MINISTRY OF NATIONAL EDUCATION

THE ANNALS OF "DUNAREA DE JOS" UNIVERSITY OF GALATI

Fascicle IX
METALLURGY AND MATERIALS SCIENCE

YEAR XXXI (XXXVI),
June 2013, no.2

ISSN 1453-083X

2013
GALATI UNIVERSITY PRESS

THE ANNALS OF "DUNAREA DE JOS" UNIVERSITY OF GALATI.
FASCICLE IX. METALLURGY AND MATERIALS SCIENCE
N^0. 2 – 2013, ISSN 1453 – 083X

Table of Content

This volume includes selected papers presented at the first edition of the *Scientific Conference of Doctoral Schools from "Dunărea de Jos" University of Galati,* CSSD-UDJG 2013, Galati, May 16-17, 2013.

***

The selected papers presented in the sections of CSSD-UDJG 2013 have been published in the following journals (Category B+), being subjected to the regular refereeing process, following the standard procedure of each journal:

1. Annals of "Dunarea de Jos" University of Galati,
Fascicle I. ECONOMICS AND APPLIED INFORMATICS, ISSN 1584-0409, Nr. 1/2013,
http://www.eia.feaa.ugal.ro/, e-mail: Economics.Annals@ yahoo.com, daniela.sarpe@ugal.ro

2. Annals of "Dunarea de Jos" University of Galati,
Fascicle II. MATHEMATICS, PHYSICS, THEORETICAL MECHANICS, ISSN 2067-2071,
Vol.V(XXXVI), Nr.1/2013**,** http://www.phys.ugal.ro/Annals_Fascicle_2, e-mail: aene@ugal.ro

3. Annals of "Dunarea de Jos" University of Galati,
Fascicle IX. METALLURGY AND MATERIALS SCIENCE, ISSN 1453-083X, Nr. 2/2013,
http://www.fimm.ugal.ro/new/index.php/annals/the-journal, e-mail: mbordei@ugal.ro

4. Annals of "Dunarea de Jos" University of Galati,
Fascicle VII. FISHERIES, AQUACULTURE&ENVIRONMENTAL SCIENCE, ISSN 2344- 3979,
Vol. 1/2013, e-mail: dgheorghe@ugal.ro

THE ANNALS OF "DUNAREA DE JOS" UNIVERSITY OF GALATI.
FASCICLE IX. METALLURGY AND MATERIALS SCIENCE
N^0. 2 – 2013, ISSN 1453 – 083X

PREPARATION AND CHARACTERISATION OF ALUMINA TEMPLATE OBTAINED BY ONE-STEP ANODIZATION METHOD

M.D. GAVRIL (DONOSE)[1], A.M. CANTARAGIU[1], C. GHEORGHIES[1], N. TIGAU[1], S. DONOSE[2]

[1]"Dunarea de Jos" Unversity of Galati, Faculty of Sciences and Environment, Chemistry, Physics and Environment Department, 800008, Galati, Romania
[2]"Sf. Grigorie Teologul" School of Galati
email: donosemihaela@yahoo.com

ABSTRACT

The goal of this study was to obtain an alumina template (AAO) by one-step anodization method and to evaluate its optical properties correlated with the annealing temperature. AAO was obtained from two different media: sulphuric acid (1.5 M H_2SO_4) and oxalic acid (0.4 M $H_2C_2O_4$) at a potential of 15 V and 40 V, respectively. AAO morphology and chemical composition had been investigated by scanning electron microscopy (SEM) and energy dispersive X-ray spectroscopy (EDX). The average pore diameters such as 20 nm for AAO obtained from H_2SO_4 and 40 nm from $H_2C_2O_4$ were measured. The crystalline structures of AAO samples annealed at three different temperatures of 150ºC, 300ºC and 350ºC were studied by X-ray diffractometry (XRD). The effect of annealing temperature on the optical properties of AAO was studied by UV-VIS spectrophotometry.

KEYWORDS: anodization, alumina template, SEM, EDX, XRD, optical properties

1. Introduction

Nowadays the porous alumina is used as the most common template material for fabricating of inorganic templates and also nanowires due to the alumina template (AAO) advantages. These are the adjustable pore diameters, uniform tubes, highly ordered porous structure [1], a reliable fabricating process with a low cost, and good thermal and chemical stability. An advantageous production method for AAO is the anodising process of aluminium from acidic electrolyte solutions with a cylindrical cell structure [2, 3] and hexagonal pattern [4]. AAO ceramic oxide has a large number of applications in high-temperature range without deformation, whereas a commercial material (Whatman Anodiscs®) cracks could appear above 700ºC due to the high mechanical tension arising from a phosphorous gradient along the pore direction [5].

Also, alumina (Al_2O_3) has lots of applications as an optical material, i.e. in thin-film devices. In this field the electronic structure and bonding presented in Al_2O_3 are intensely studied. Practically, the optical properties have a high interest calculating the optical constants of Al_2O_3 [6, 7] with high accuracy. These properties can be analysed using atomic force microscopy (AFM) [8], and reflectance spectroscopy techniques at room temperature [9] and high temperature [10].

The goal of this study was to obtain the AAO by one-step anodization method from two different media and to characterize the AAO morphology and structure by means of scanning electron microscopy (SEM) technique. Then, as-prepared AAO is crystalline to X-ray diffraction (XRD). XRD and thermal treatment techniques have been used to characterize the crystalline phase transitions of AAO prepared in oxalic acid [11] and sulphuric acid [12] at temperatures up to 150ºC, 300ºC and 350ºC respectively. For the synthesis of AAO regular pore matrix, a pre-treatment by polishing, chemical degreasing, etching and pre-texturing was required [13]. Also, the correlation between the AAO optical properties and annealing temperatures was evaluated.

2. Experimental details

High purity aluminium foil (95% Al, 50mm by 50mm and 2mm thick) was used as a substrate material for template. Aluminium with a high purity

is usually recommended to obtain self-ordered porous alumina. The quality of substrate surface has major influences on the nanostructure by self-organized anodization. Firstly, these pieces were mechanically polished with SiC paper with different granulations, and then cleaned and activated following the next steps. These procedures consist of an organic degreasing in acetone for 10 min, chemical degreasing in 1M NaOH for 5 min, etching by immersion in 5% HNO_3 for 5 min, rinsing with distilled water, and then drying in air.

Two AAO development stages are summarised into the below schematic diagram. Fig. 1a shows the aluminium surface pre-treated like substrate for the following alumina layer, before the anodization. Fig. 1b indicates the aluminium anodised with channels growing nano-sized [14].

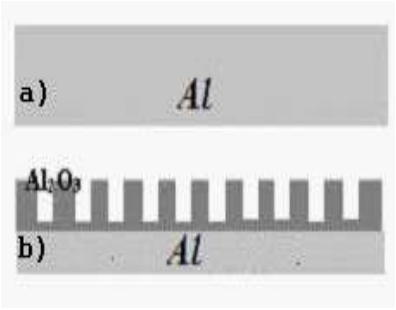

Fig. 1. *Schematic diagram of AAO development on aluminium layer a) before and b) after the anodic process*

A standard two electrod system with a cell (Fig. 2) volume of 500 mL connected at a PM 2813 programmable power supply were used to perform the anodization process. Both cathode and anode were aluminium plate electrodes. This study approached the AAO synthesis by one-step anodization method. During the anodic process both aluminium faces with a circular sector shaped are exposed to acidic solutions. Each AAO was fabricated in 0.4M oxalic acid ($H_2C_2O_4$) electrolyte and 1.5M sulphuric acid (H_2SO_4) at lower than room temperature (18°C). The alumina layer has grown by passing a direct current (DC) through solution. The anodization voltage scheme consists of 60min exposure time at 15V and 40V respectively.

The passing current through aqueous solution produces hydrogen reaction at the cathode surface and oxygen with alumina at the anode surface (1). Aluminium anodizing performed in acidic solution slowly dissolves the alumina layer obtained. The aluminium oxide dissolution process is balanced with the oxidation ratio to nanopores [15, 16].

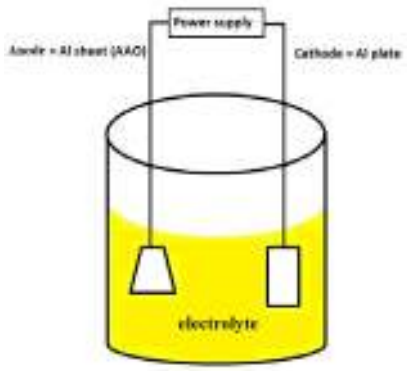

Fig. 2. *Experimental set-up of anodization cell*

$$Al(s) \rightarrow Al^{3+}(oxide) + 3e^{-}$$
$$\frac{3}{2}H_2O(l) \rightarrow 3H^{+}(aq.) + \frac{3}{2}O^{2-}(oxide) \quad (1)$$

Aluminium substrate and AAO morphological characteristics were analysed by means of SEM technique using EVO 50 EP microscope (Karl Zeiss SMT AG, Germany). The micrographs were picked-up at (2÷5) kV using the secondary electron detector. For better conductivity during SEM examination, samples were prepared by means of sputering technique with an ultra-thin platinum layer.

Three AAO samples obtained from oxalic solution were heat treated (annealed) to different temperatures (150ºC, 300ºC and 350ºC) consisting of introducting them in furnace L312 P320 Nabertherm for 3h.

The crystallographic characteristics of the annealed samples were analysed by means of XRD using DRON-3M diffractometer. XRD spectra were recorded at room temperature, and diffractometer using CoK_α radiation (λ = 1.79Å) in 2θ configuration ranged between 40º and 70º, at 40kV tension and 30mA current intensity with a scanning speed of 0.02º min^{-1} and acquisition time of 1 s/step.

Also, for all samples the reflectance measurements were recorded by means of spectroscopy method using Perkin Elmer 35UV-VIS spectrophotometer with a spectral range of (190÷1100) nm.

3. Results and discussion

SEM plan view of the aluminium foil morphology after the required pre-treatment and before the anodic process is shown in Fig. 3a. The aluminium surface is still slightly rough and for future experiments an electropolishing treatment is again required.

It is well-known that anodization of aluminium containing impurities could lead to defects.

Aluminium chemical composition of a homogeneous selected area (Fig. 3b) was determined by means of energy dispersive X-ray spectroscopy (EDX).

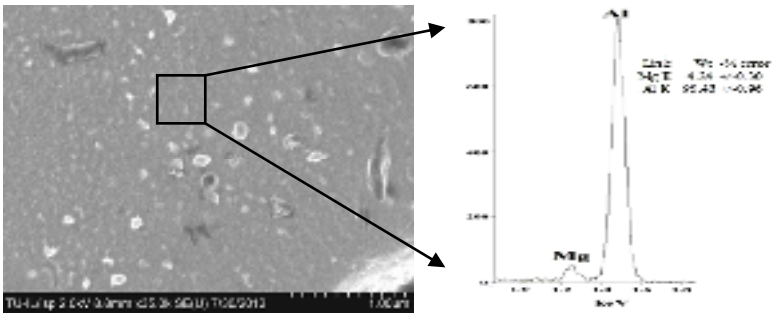

a) *b)*

Fig. 3. *Aluminium substrate: a) morphology (35.000×) and b) chemical composition*

Aluminium substrate used in these experiments contain 95 wt.% of Al and 5 wt.% of Mg.

Fig. 4 reveals a plan view of the as-prepared anodic films (before thermal treatment) obtained from sulphuric acid at 15V (Fig. 4a) and oxalic acid at 40V potential (Fig. 4b).

Their morphology showed an ordered porosity, similar to Keller's model [17].

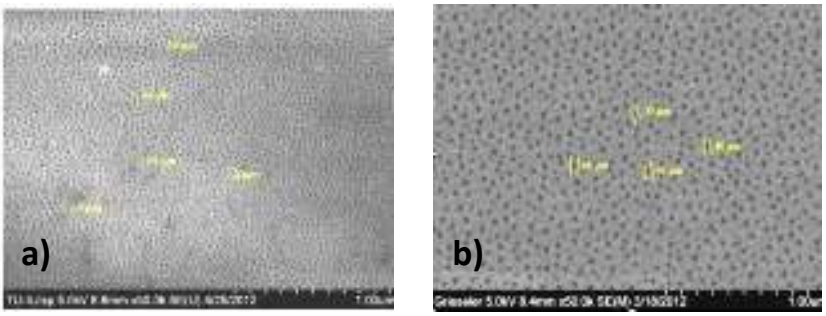

Fig. 4. *SEM images (50.000×) of porous oxidized templates produced by one-step anodization in: a) sulphuric acid and b) oxalic acid*

The average pore diameters were measured and revealed 20nm for the pores obtained from sulphuric acid and 40nm for those obtained from oxalic acid showing a hexagonal lattice.

Consequently, it was observed a change of the physical and chemical properties as well as of the anodic oxide film colour (different grey intensity). Pores diameter and interpores distance varied with anodization parameters such as type and concentration of the electrolyte, temperature, impurities and applied potential during the anodic process. The results are in concordance with the literature [18].

The internal structure of the AAO annealed samples was analyzed at room temperature by means of XRD method. A crystallization process varied with the annealing temperature showing α- and θ-(Al_2O_3) phases.

Diffraction patterns of AAO annealed at 150ºC, 300ºC and 350ºC are shown in Fig. 5.

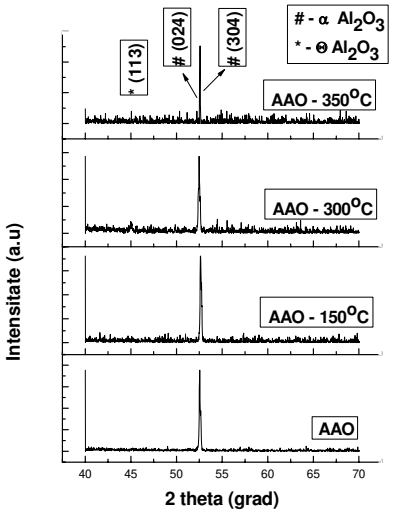

Fig. 5. *XRD patterns of AAO (obtained from $H_2C_2O_4$) annealed at 150ºC, 300ºC and 350ºC*

AAO is annealed below the melting point of aluminium, that is 680ºC, to obtain a large grain size.

XRD result of annealed AAO shows (113) plane at 2θ = 45º, (024) and (304) planes appeared at 2θ = 51.5º and 52.5º, respectively AAO structure became more crystalline with the annealing process relieving θ- and α-(Al_2O_3) phase. The annealing temperature changes the crystal structure of the alumina (θ hexagonal and α rhomboedric). The values of the diffraction peaks are in accordance with both standard JCPDS alumina card (MP 1323 and MP 1423).

Reflectance curves of annealed AAO at different temperatures are indicated in Fig. 6. Linear shape of curves is shown in the UV region where the reflectance coefficient values are constant (R~0.005%). VIS interested region presents the reflectance plots easily distinguished. AAO adsorbent and reflective features with increasing the annealing temperature are highlighted.

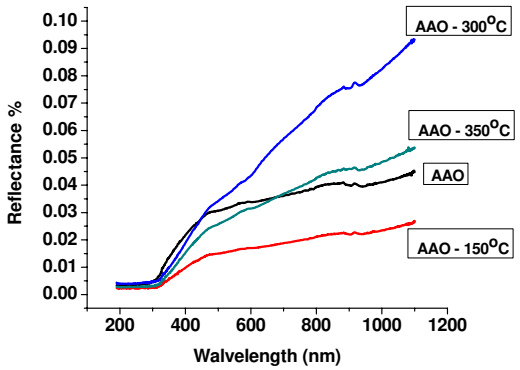

Fig. 6. *Reflectance spectra of AAO (obtained from $H_2C_2O_4$) annealed at 150ºC, 300ºC and 350ºC*

AAO annealed sample at the lowest temperature of 150°C has been oxidized having darker and more opaque visual aspect. Thereby, AAO high adsorption level was marked out because the oxide compounds forming on the template surface were compared with other two samples [19]. Increasing annealing temperature can determine pores agglomeration [20, 21].

This fact is confirmed by the pores widening and the interpores distance reducing differentially. Therefore, template surfaces became slightly rough favouring their reflexion ability. At 300°C and 350°C, respectively, the reflectance coefficient has increased and also the spectral curves show increased amplitude. Increasing wavelength the reflectance plots suddenly follow an exponential increasing as function of annealing temperature variation in IR region.

4. Conclusions

The alumina template was obtained by one-step anodization method from oxalic and sulphuric acid electrolytes at different parameters. A pre-treatment of aluminium substrate is required to assure the quality surface to obtain self-ordered porous alumina. The roughness degree of substrate was the most important factor which can influence the nanopores linearity and symmetry respectively. The template morphologies show a hexagonal lattice of nanopores with an average diameter of 40nm for them obtained from oxalic acid and 20nm from sulphuric acid. A changing of AAO physical and chemical properties as well as of the anodic oxide film colour (different grey intensity) due to the anodization parameters such as type and concentration of the electrolyte, temperature, impurities and applied potential during the anodic process was observed. The internal structure of AAO annealed samples was analyzed at room temperature by means of XRD method. The crystallization process varied with the annealing temperature showing α and θ-(Al_2O_3) phases.

The alumina reflectance as function of radiation wavelength for AAO annealed at different temperatures was observed. AAO absorbent and reflective features with increasing the annealing temperature are highlighted. The high absorbance ability is proved by AAO produced in $H_2C_2O_4$ and annealed at lowest temperature of 150°C in VIS spectrum.

Finally, this model was the basis for initial studies that aimed at better understanding of the physical and chemical properties of porous alumina and obtaining promised cobalt nanowires in self ordered alumina.

Acknowledgement

This work was financially supported by the Project SOP HRD - TOP ACADEMIC 76822. The authors gratefully acknowledge Dr. Adriana Ispas for guidance and SEM measurements. We are grateful to Andreas Bund and Udo Schmidt from Technische Universität Ilmenau, FG Elektrochemie und Galvanotechnik, Ilmenau, Germany for the efficacious discussions and advices. The authors would also thank Prof. Dr. Viorica Musat for the annealing treatment.

References

[1]. H. Masuda, K. Fukuda – *Ordered metal nanohole arrays made by a two-step replication of honeycomb structures of anodic alumina*, Science, 268 (1995), 1466.

[2]. J.P. O'Sullivan, G.C.Wood – *The morphology and mechanism of formation of porous anodic films on aluminium,* Proc. R. Soc., London, A 317 (1970), 511.

[3]. R.C. Furneaux, W.R. Rigby, A.P. Davidson – *The formation of controlledporosity templates from anodically oxidized aluminium*, Nature, 337 (1989), 147.

[4]. H. Masuda, F. Hasegawa, S. Ono – *Self-ordering of cell arrangement of anodic porous alumina formed in sulphuric acid solution*, J. Electrochem. Soc., 144 (1997), L127.

[5]. I.W.M. Brown, M.E. Bowden, T. Kemmitt, K.J.D. MacKenzie – *Structural and thermal characterisation of nanostructured alumina templates*, Curr. Appl. Phys., 6 (2006), 557.

[6]. M.E. Innocenzi, R.T. Swimm, M. Bass, R.H. French, A.B. Villaverde, M. R. Kokta – *Room-Temperature Optical Absorption in Undoped α-Al_2O_3*, J. Appl. Phys., 67 (1990), 7542–7546.

[7]. M.E. Thomas, W.J. Tropf, S.L. Gilbert – *Vacuum-Ultraviolet Characterization of Sapphire, AlON, and Spinel Near the Band Gap*, Opt. Eng., 32 (1993), 1340–1343.

[8]. C. Argento and R. H. French – *Parametric Tip Model and Force–Distance Relation for Hamaker Constant Determination from AFM*, J. Appl. Phys., 80 (1996), 6081–6090.

[9]. R. H. French – *Electronic Structure of a-Al_2O_3, with Comparison to AlON and AlN*, J. Am. Ceram. Soc., 73 (1990), 477–489.

[10]. M.L. Bortz, R.H. French, D.J. Jones, R.V. Kasowski, F.S. Ohuchi – *Temperature Dependence of the Electronic Structure of Al_2O_3, $MgAl_2O_4$, and MgO*, Phys. Scr., 41 (1990), 537–541.

[11]. P.P. Mardilovich, A.N. Govyadinov, N.I. Mukhurov, A.M. Rzhevskii, R. Paterson – *New and modified anodic alumina templates. Part I. Thermotreatment of anodic alumina templates*, J. Membr. Sci., 98 (1995), 131.

[12]. R. Ozao, M. Ochiai, H. Yoshida, Y. Ichimura, T. Inada – *Preparation of γ-alumina templates from sulphuric electrolyte anodic alumina and its transition to α-alumina*, J. Thermal Anal. Calorim., 64 (2001), 923.

[13]. H. Asoh, K. Nishio, M. Nakao, T. Tamamura, H. Masuda – *Conditions for fabrication of ideally ordered anodic porous alumina using pretextured Al*, J. Electrochem. Soc., 148 (2001), B152.

[14]. Cynthia G. Zoski – *Handbook of Electrochemistry*, Elsevier, 2007.

[15]. Robert S. Alwitt – *Anodizing*, www.electrochem.cwru.edu/encycl.

[16]. www.shodor.org.

[17]. F. Keller, M.S. Hunter, D.L. Robinson – *Structural Features of Oxide Coatings on Aluminum*, J. Electrochem. Soc., 100 (1953), 9, 411-419.

[18]. P. Bocchetta, C. Sunseri, A. Bottino, G. Capannelli, G. Chiavarotti, S. Piazza, F. Di Quarto – *Asymmetric alumina membranes electrochemically formed in oxalic acid solution* Journal of Applied Electrochemistry 32: 977–985, 2002.

[19]. C. Gheorghies, L. Gheorghies, S. Ciortan, V. Paunoiu, A.M. Cantaragiu, C.C. Lalau, D.E. Rusu – *Structural Analysis of Alumina Thin Layer Prepared by Controlled Oxidation Process,* The Annals of "Dunărea de Jos" University of Galaţi, Fascicle V, Technologies in Machine Building (2009), 319-322.

[20]. L. Gheorghies, A. Sion - *Obţinerea şi analiza acoperirilor metalice de protecţie*, Ed. CERMI, Iaşi, 2012

[21]. L. Gheorghies - *Nanomecanica suprafetei*, Ed. Ars Docendi, Bucuresti, 2004

THE ANNALS OF "DUNAREA DE JOS" UNIVERSITY OF GALATI.
FASCICLE IX. METALLURGY AND MATERIALS SCIENCE
N^0. 2 – 2013, ISSN 1453 – 083X

INFLUENCE OF THERMAL TREATMENT ON ZIRCONIA POWDER

Livia GHEORGHIES
"Dunărea de Jos" University of Galati, Faculty of Materials Engineering and Environment,
111, Domnească Street, RO-800201, Galati, Romania
email: cgheorg@ugal.ro

ABSTRACT

Zirconia powder in amorphous state was prepared by electrolytic deposition method (ELD) and then it was subjected to a thermal treatment according to a typical diagram. The structural changes in zirconia powder induced by thermal treatment have been pointed out by X-Ray diffraction (XRD), thermogravimetric analysis (TGA) and differential thermoanalysis (DTA) techniques. During thermal treatment, XRD patterns and DTA curves showed the presence of a mixture of two crystalline phases well-formed at approximately 400^{o}C and a transformation of the type tetragonal-monoclinic ($t \rightarrow m$) at approximately 600^{o}C. In situ XRD study allowed establishing the growth kinetics of crystalline phases. Using experimental maximum intensities, $H_{(hkl)}$ and integral intensities, $I_{(hkl)}$, of XRD peaks, the volume fractions, V_m, and V_t, of m and t phases, respectively, present in a polymorphic mixture were calculated.

KEYWORDS: zirconia, powder, temperature, structure

1. Introduction

Zirconia is an oxide ceramic with chemical formula ZrO_2 that has attracted the interest of researchers mainly due to useful properties in practical applications such as thermal stability, thermal shock resistance and corrosion resistance. This oxide ceramic is used in catalysis technique and electronics as dielectric and piezoelectric material. Ceramic materials based on zirconia have many applications due to their many qualities such as heat resistance, high strength and hardness, low thermal conductivity, and ionic conductivity at high temperatures [1-2]. These materials fabricated by different techniques are used as tribological protections, thermal barriers for engine, and bioinert coatings in the medical field [3-5]. Often the ways of obtaining and processing powder influence the properties of ceramics.

ELD is among the many techniques used to obtain powder materials. Using aqueous or organic solutions, this method is often preferred for the preparation of powders due to primarily relatively simple technique which takes place at normal temperature and pressure, possibility of application to industrial scale and automation. The electrolytically obtained powders have a high purity and their microstructure can be controlled and managed by monitoring operating parameters such as electrolyte type, its concentration and pH, and other process variables, i.e. voltage, electric current, temperature, speed of reaction.

Under normal conditions, zirconia exists in three polymorphic forms in equilibrium state for different temperature, T, according to the Joint Committee on Powder Diffraction Standards (JCPDS) [6]: monoclinic (*m*) T < 1205^{o}C (JCPDS: 37 – 1484), tetragonal (*t*) 1075 ^{o}C < T < 2377 ^{o}C (JCPDS : 50 – 1089) and cubic (*c*) 2377^{o}C < T < 2680^{o}C (melting point) (JCPDS : 51 – 1149). Zirconia forms of higher symmetry have properties very often preferable to the ones of monoclinic form so they are stabilized in various ways. The temperature at which the tetragonal to cubic transformation occurs can be lowered, by the addition of some solutes such as MgO, CaO, Y_2O_3. The presence of tetragonal zirconia as dispersed phase determines the increasing of the fracture strength, toughness and hardness of oxides as well as nonoxides ceramics [7].

Due to its high melting point, zirconia is an attractive refractory material. However, $t \rightarrow m$ transformation is accompanied by an increase in volume that causes disintegration of powder during cooling process [8]. The knowledge of the $t \leftrightarrow m$ transformation mechanism determined by the influence of thermal processes is very important in

the industrial applications. In some circumstances, the tetragonal phase is present in addition to the monoclinic phase at room temperature (RT). This is the subject of research of many scientific papers.

According to them, the reason for the formation of this high temperature phase at RT can be: presence of anionic impurities or other defects in the lattice as adsorbed oxygen [9]; residual stresses [10]; minimum surface energy [11]; lattice defects as oxygen vacancies or water vapours [12].

The m→t phase transformation can be controlled by nucleation mechanism that is almost nonexistent at RT but can be activated mechanically or thermally [13].

The purpose of this paper is to study of effects the thermal treatment on the phase transformations undergone by amorphous zirconia obtained by ELD from an aqueous electrolyte.

A qualitative and quantitative analysis on identification for the crystalline phase of zirconia was conducted using XRD, TGA, and DTA methods.

2. Experimental procedure

Amorphous zirconia powder was prepared by ELD from an aqueous solution of $ZrO(NO_3)_2$ (Merck, p.a. grade) on a graphite cathode with spectral purity [14]. The resulting powder was heat treated at different temperatures from RT to 800^{o}C.

Structural investigation was made by a DRON 3 X-ray diffraction instrument equipped with a high temperature oven-chamber using CuKα X-ray with the wavelength λ=1,5417 Å, at a voltage of 36 kV and a current of 20 mA.

During the experiments, temperature was controlled with a Pt-Pt-Rh (10%) electronic thermocouple having an accuracy of ±1^{o}C. The sample was prepared by pressing the starting compound into a tantalum grid. The scanning angle, 2θ, was varied from 26^o to 34^o with a detection step of 0.02^o while the temperature was increased. In order to eliminate any effects of texture during the XRD analysis, the sample was rotated in a plane parallel to the axis of the goniometer. The international diffraction data base of JCPDS has been used to identify the crystalline phases.

In order to elucidate the changes in physical properties of zirconia powder as function of temperature, simultaneous measurement of TGA and DTA were performed by a derivatograph of the system F.Paulik, J.Paulik, L. Erdey (MOM, Budapest, Hungary).

The experiments were carried out in open crucible, with a heating rate of 20^{o}C/minute and using alumina calcined at 1400^{o}C as standard material.

3. Results and discussions

The crystal structure and phase composition of the resulting zirconia powder were investigated by XRD. Figure 1 shows the XRD patterns of the powder electrodeposited on the graphite electrode indicating the existence only of the typical graphite peak and none of the distinctive peaks of zirconia because this is amorphous. In order to characterize and identify the phase transformations caused by thermal treatment, the amorphous powder was removed from the graphite electrode and pressed into a sample tantalum holder which was put in the high temperature oven-chamber.

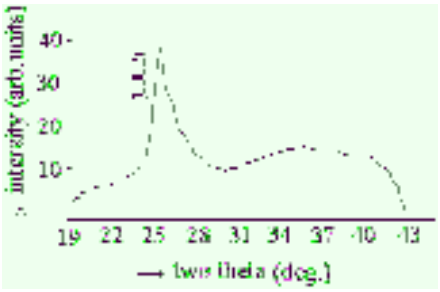

***Fig. 1**. XRD pattern of amorphous zirconia electrodeposited on graphite electrode*

The heat treatment was performed at the different temperature in air or in argon atmosphere with the maintaining time of one hour and cooling together furnace. The evolution of the XRD patterns for different temperatures is shown in Figure 2. The appearance and development of (hkl) zirconia characteristic peaks with increasing temperature are pointed out.

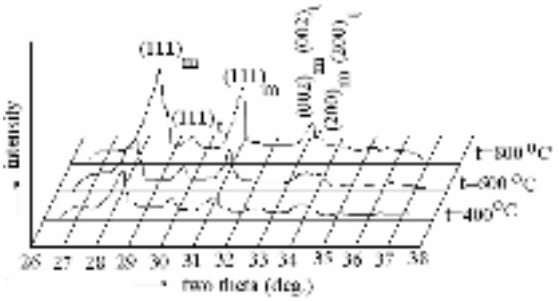

***Fig. 2**. XRD patterns of thermally treated zirconia powder*

Only around 600^{o}C, *m* and *t* phases are well formed and their $(200)_m$, $(200)_t$, $(002)_m$, $(002)_t$ peaks are clearly distinct. Consequently to calculate the volume fractions of the two phases, the $(111)_t$, $(111)_m$ and $(\bar{1}11)_m$ well-formed peaks were chosen.

Using experimental maximum intensities, $H_{(hkl)}$ and integral intensities, $I_{(hkl)}$, of these peaks, the volume fraction, V_m, of monoclinic phase present in a polymorphic mixture was calculated [15]:

$$V_m = \frac{P \cdot X_m}{1+(P-1)X_m} \quad (1)$$

where

$$P = \frac{H_{(111)_t}}{H_{(\bar{1}11)_m} + H_{(111)_m}} \quad (2)$$

and

$$X_m = \frac{I_{(\bar{1}11)_m} + I_{(111)_m}}{I_{(\bar{1}11)_m} + I_{(111)_m} + I_{(111)_t}} \quad (3)$$

The data presented in the table 1 show that the volume fractions of the two phases, V_m and V_t, respectively, increase with temperature, but the former exceeds the latter.

Table 1. *Volumetric fractions of zirconia phases*

Sample	T	Atmosphere	V_m	V_t
	[^{o}C]		[%]	
1	400	air	85	15
2	600	air	92	8
3	800	air	97	3
4	800	argon	97	3

In situ crystallization study requires fast collection of data at high temperatures. Such measurements were performed during both the heating and the cooling processes.

The heating was fast up to 400^{o}C and slowly continued with a speed of 20^{o}C/min up to 804^{o}C. During heating, the X-ray detector scans were fast with a speed of 8^{o}C/min and the direction of rotation of the goniometer was changed manually. One change requested 12 seconds and during which time the temperature rose by 4^{o}C.

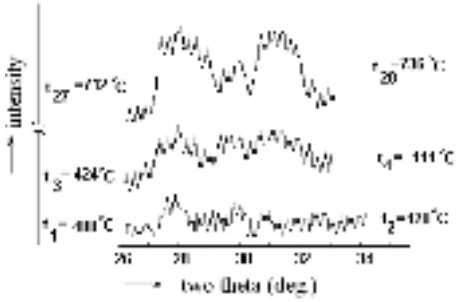

Fig. 3*. In situ XRD patterns for different temperature ranges*

The entire temperature range was covered in 1224 seconds when 17 scans were performed, seven of them in counter-clockwise and the rest in reverse. Some of the obtained diffraction patterns are shown in Figure 3. Left and right values represent the starting and ending temperatures of the sample during scanning process.

The analysis of XRD patterns allowed establishing the growth kinetics of crystalline phases, i.e. development of mosaic blocks. The aspect of two experimental curves allows having an overview of the growth kinetics of the crystalline phases from amorphous powder as presented in Figure 4. The figure shows the existence of the two crystalline phases and their stabilization tendency after the temperature reached 804^{o}C, during the heating process, the goniometer being fixed in specific angular positions to receive *t* and *m* phase peaks respectively.

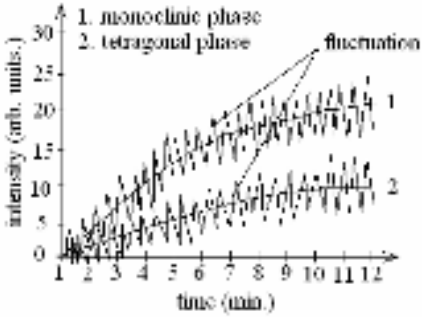

Fig. 4*. Kinetics curves of crystalline phases*

The cooling with a speed of 20^{o}C/min from 804^{o}C to RT was also conducted. Some XRD patterns presented in Figure 5 reveal that the tetragonal phase is stable to near about 400^{o}C and then it was converted in the monoclinic form. Left and right values represent the starting and ending temperatures of the sample during the scanning process. Compared to the heating stage, kinetics is altered so that transformations occurred faster and at lower temperatures.

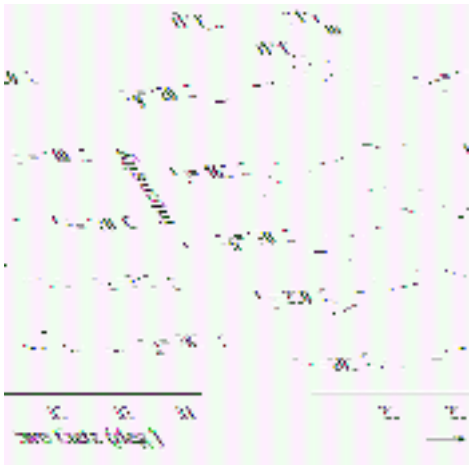

Fig. 5*. XRD patterns of powder zirconia obtained at quickly scanning*

The TGA and DTA data on zirconia powder are presented in Figure 6. A significant mass loss appeared at 150^{o}C can be attributed to removal of water. It is accompanied at DTA curve by a low endothermic peak determined probably by the release of the volatile compounds. At approximately 400^{o}C the well-formed exothermic peak corresponds to the crystallization of amorphous zirconia and the next lower peak appeared at approximately 600^{o}C is determined by the $t \rightarrow m$ phase transition process confirmed also by XRD [16].

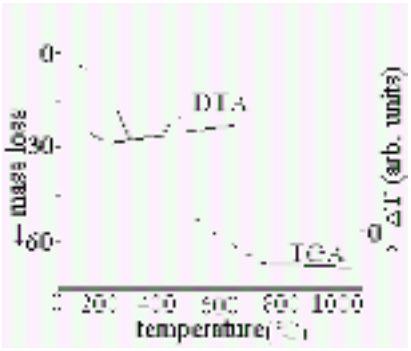

***Fig. 6**. TGA and DTA curves*

4. Conclusions

Zirconia obtained by ELD is amorphous at RT and crystallizes after heating at about 400^{o}C and the $t \rightarrow m$ allotropic transformation occurs at about 600^{o}C. During the heating process of the electrodeposited zirconia powder, the volume fraction of the *m* phase exceeds the *t* one. Crystallization kinetics of zirconia powder can be determined by in situ XRD studies over time following the changes of maximum or integral intensity of the diffraction peaks.

Modern XRD instruments equipped with suitable software permit the improving of the pattern quality and reduction of the data acquisition time, making this a more powerful technique.

References

[1]. A.K. Bandyopadhyay - Nano Materials, New Age International, New Delhi, (2008)
[2]. K.C. Patil, M.S. Hedge, T. Rattan and S.T. Aruna - World Scientific, New Jersey, (2008)
[3]. J.-P. Maria, D. Wicaksana, A. I. Kingon, B. Busch, H. Schulte, E. Garfunkel, and T. Gustafsson - J. Appl. Phys. **90**, 3476 (2001)
[4]. G. D. Wilk, R. M. Wallace, and J. M. Anthony - J. Appl. Phys. **87**,484 (2000)
[5]. C. J. Först, C. R. Ashman, K. Schwarz, and P. E. Blöchl - Nature London **427**,53 (2003)
[6]. JCPDS Database, International Center for Diffraction Data (2003)
[7]. S. Shukla, S. Seal, R. Vij and S. Bandyopadhyay - J. Nanopart. Res. 4, 553-559 (2002)
[8] J. Tang et.al - Adv. Funct. Mater. 15, 1595-1602 (2005)
[9]. M. Bhagwat, V. Ramaswamy, Materials Research Bulletin 39 1627–1640 (2004)
[10]. J. Chevalier, L. Gremillard, A. V. Virkar and D. R. Clarke - J. Am. Ceram. Soc.,92 [9] 1901–1920 (2009)
[11]. F. Zhang et.al. - Analyses Chem. Mater., 19, 3118-3126 (2007)
[12]. J. R. Kelly and I. Denry - Dental Materials 24 289–298 (2008)
[13]. R. H.J. Hannink, P. M. Kelly and B. C. Muddle - J. Am. Ceram.Soc. 83[3] 461-487 (2000)
[14]. *C.* Gheorghies, *L.* Gheorghies - Sept. 18-21, Leganes, Madrid, Spain, p.455-459 (2001)
[15]. H. Toraya, M. Yoshimura, and S. Somiya - J. Am. Ceram. Soc., 67 [6] C119–21 (1984)
[16]. V. Santos, M. Zeni, C.P. Bergmann and J.M. Hohemberger - Rev.Adv.Mater.Sci. 17, 62-70 (2008)

THE ANNALS OF "DUNAREA DE JOS" UNIVERSITY OF GALATI.
FASCICLE IX. METALLURGY AND MATERIALS SCIENCE
N^0. 2 – 2013, ISSN 1453 – 083X

CELLULAR AUTOMATA METHOD IN STUDYING RECRYSTALLIZATION PROCESS

Vasile ANĂSTĂSOAEI, Constantin GHEORGHIES
"Dunărea de Jos" University of Galati, Faculty of Science and Environment,
111, Domnească Street, RO-800201, Galati, Romania
emails: Vasile.Anastasoaei@ugal.com, Constantin.Gheorghies@ugal.ro

ABSTRACT

A cellular automaton is a decentralized computing model providing a platform for performing complex computation with the help of only local information. The cellular automata method describes the evolution of a discrete system of variables by applying a set of deterministic (or probabilistic) rules that depend on the values of the variables as well as those in the nearby cells of a regular lattice. In this paper we present some types of cellular automata used for modelling and simulating recrystallization process.

KEYWORDS: cellular automata, modelling, recrystallization process

1. Introduction

A cellular automaton is a discrete dynamical system that consists of a regular network of finite state automata, named cells, which change their states depending on the states of their neighbors, according to a local update rule. All cells change their state simultaneously, using the same update rule. The process is repeated at discrete time steps. Cellular automata are discrete in both space and time, homogeneous in space and time, and local in their interactions. Cellular automata can have arbitrary dimensions. Space is defined on a regular array of cells that can be regarded as the nodes of a finite difference field. The state of each cell is characterized in terms of a set of generalized state variables. The actual values of these state variables are defined at each of the individual cell. The opening state of the automaton is defined by mapping the initial distribution of the values of the chosen state variables onto the cells in the network. The dynamic evolution of the automaton takes place through the application of deterministic (or probabilistic) transformation rules that act on the state of each cell. These rules determine the state of a cell as a function of its previous state and the state of the neighbours of the cell. Cellular automata work in discrete time steps. After each time interval, the values of the state variables are updated for all cells simultaneously, mapping the new values assigned to them through the transformation rule. Cellular automata were introduced by von Neumann and Ulam for the simulation of self-reproducing Turing automata and population evolution. In the last years, cellular automata have been used to simulate the microstructure evolution in materials science. In this domain a number of different aspects were addressed, namely, primary static recrystallization (Hesselbarth and Gobel, [2]; Pezzee and Dunand [3]; Marx and Raabe [4]). Although cellular automaton simulations are typically carried out at an elementary level (atoms, clusters of atoms, dislocation segments, subgrains), it should be emphasized that particularly those variants that discretize and map in a continuum space are not intrinsically calibrated by a characteristic physical length or time scale. This means that a cellular automaton simulation of continuum systems requires the definition of elementary units and transformation rules that adequately reflect the system behaviour at the level addressed.

2. Basic definitions and notations

Let d be a positive integer. We consider Z^d a d-dimensional cellular space, whose elements are called cells. Let S be a finite set of elements, called states. A *configuration* is a function $c: Z^d \rightarrow S$ that assigns a state to each cell. A d-dimensional *neighbourhood vector*, of size m, is a t-uple $N= (z_1,z_2,...,z_m)$, where each $z_i \in Z^d$, and $z_i \neq z_j$ for all $i \neq j$. The elements z_i specify the relative locations of the neighbours of each cell. A *rule* (local rule) is a function $f: S^m \rightarrow S$, that specifies the new state of each cell based on the old states of its neighbours. If the neighbours of a cell

have states $s_1,s_2,\ldots,s_m$, then the new state of the cell is $f(s_1,s_2,\ldots,s_m)$. In cellular automata all cells use the same rule, and the rule is applied at all cells simultaneously.

To specify a cellular automaton one needs to specify the following items:

- the dimension *d,*
- the finite state set S,
- the neighbourhood vector $N= (z_1, z_2 \ldots , z_m)$, and
- the local rule $f:S^m \rightarrow S$.

Formally, we define the corresponding *cellular automaton* to be the 4-uple $A=(d,S,N,f)$.

Let $N= (z_1, z_2 \ldots, z_m)$ be a d-dimensional neighbourhood vector. For any cell $z \in Z^d$, we denote $N(z) = (z + z_1, z + z_2, \ldots, z + z_m)$, and for any $K \in Z^d$, we denote $N(K) = \{z + z_i | z \in K, i = 1,2,\ldots,m\}$, that is N(z) is the ordered sequence of the neighbours of cell z, while N(K) is the unordered set of neighbours of cells in K. In the two-dimensional space, the *von Neumann-* and the *Moore-* neighbourhoods are often used. In the von Neumann configuration, $N=(z_1,z_2,z_3,z_4)$, $z_1=(-1,0)$, $z_2=(0,-1)$, $z_3=(0,1)$, $z_4=(1,0)$, while in the Moore configuration, $N=(z_1,z_2,z_3,z_4, z_5,z_6,z_7,z_8)$, $z_1=(-1,-1)$, $z_2=(-1,0)$, $z_3=(-1,1)$, $z_4=(0,-1)$, $z_5=(0,1)$, $z_6=(1,-1)$, $z_7=(1,0)$, $z_8=(1,1)$ (Fig. 1).

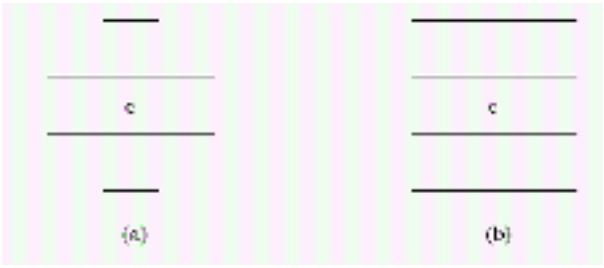

***Fig. 1**. The (a) von Neumann and (b) Moore neighbors of the c cell*

The local interaction of neighbouring sites in a cellular automaton is specified through a set of deterministic or stochastic transformation rules. The value of an arbitrary state variable s assigned to a particular site at a time t ($t=t_0+\Delta t$) is determined by its present state (t_0) or its last few states (t_0, $t_0-\Delta t$, etc.) and the state of its neighbors. For example, in a one-dimensional cellular automaton case, considering the last two time steps for the evolution of the cellular automaton, we can write formally

$$s_j^{t_0+\Delta t} = f(s_{j-1}^{t_0-\Delta t}, s_j^{t_0-\Delta t}, s_{j+1}^{t_0-\Delta t}, s_{j-1}^{t_0}, s_j^{t_0}, s_{j+1}^{t_0})$$

where $s_j^{t_0}$ indicates the value of the variable at a time t_0 at the node j.

The positions $j+1$ and $j-1$ indicate the nodes in the immediate neighborhood of position j.

The function f specifies the set of transformation rules, such as provided by standard finite difference algorithms. Due to the discretization of space, the type of neighboring affects the local transformation rates. In the case of a higher-dimensional cellular automaton simulation, with independent variables described by rectangular coordinates, the predictions become dependent on the shape of cells. In the two-dimensional case, with von Neuman configuration, we have $x(i,j)=f(x(i-1,j),x(i,j-1),x(i,j+1),x(i+1,j))$, while with the Moore configuration, we have $x(i,j)=f(x(i-1,j-1),x(i-1,j),x(i-1,j+1), x(i,j-1),x(i,j+1)\ \ x(i+1,j-1),,x(i+1,j), x(i+1,j+1))$.

Transforming these somewhat abstract rules and properties associated with general automata into a materials-related simulation concept consists in mapping the values of relevant state variables onto the cells of a cellular automaton grid which reflects the independent spatial coordinates, and using the approximate local finite difference solutions of the underlying partial differential equations of the model addressed as local transformation rules.

For the Moore configuration, which allows one to introduce a certain medium-range interaction among the sites, the equation of the state can be writen as:

$$s_j^{t_0+\Delta t} = f(s_{j-2}^{t_0-\Delta t}, s_{j-1}^{t_0-\Delta t}, s_j^{t_0-\Delta t}, s_{j+1}^{t_0-\Delta t}, s_{j+2}^{t_0-\Delta t}, s_{j-2}^{t_0}, s_{j-1}^{t_0}, s_j^{t_0}, s_{j+1}^{t_0}, s_{j+2}^{t_0})$$

The state of a cellular automaton is completely specified by the transformation rules and by the values of the state variables at each site. Even for very simple automata there exists an enormous variety of possible transformation rules. For a one-dimensional binary cellular automaton with von Neumann neighboring, each node must assume one of two possible states, $s_j=0$ or $s_j=1$. From the state equation

$$s_j^{t_0+\Delta t} = f(s_{j-1}^{t_0}, s_j^{t_0}, s_{j+1}^{t_0})$$

we can define 2^8 possible deterministic or probabilistic transformation rules f.

One of them is

if $\left(s_{j-1}^{t_0} = 0, s_j^{t_0} = 0, s_{j+1}^{t_0} = 0\right)$

then $s_j^{t_0+\Delta t} = 0$ $\quad (0,0,0) \rightarrow 0$

if $\left(s_{j-1}^{t_0} = 0, s_j^{t_0} = 0, s_{j+1}^{t_0} = 1\right)$

then $s_j^{t_0+\Delta t} = 1$ $\quad (0,0,1) \rightarrow 1$

if $\left(s_{j-1}^{t_0} = 0, s_j^{t_0} = 1, s_{j+1}^{t_0} = 0\right)$

then $s_j^{t_0+\Delta t} = 0$ $\quad (0,1,0) \rightarrow 0$

if $\left(s_{j-1}^{t_0} = 0, s_j^{t_0} = 1, s_{j+1}^{t_0} = 1\right)$

then $s_j^{t_0+\Delta t}=1 \qquad (0,1,1)\rightarrow 1$

if $\left(s_{j-1}^{t_0}=1, s_j^{t_0}=0, s_{j+1}^{t_0}=0\right)$

then $s_j^{t_0+\Delta t}=1 \qquad (1,0,0)\rightarrow 1$

if $\left(s_{j-1}^{t_0}=1, s_j^{t_0}=0, s_{j+1}^{t_0}=1\right)$

then $s_j^{t_0+\Delta t}=0 \qquad (1,0,1)\rightarrow 0$

if $\left(s_{j-1}^{t_0}=1, s_j^{t_0}=1, s_{j+1}^{t_0}=0\right)$

then $s_j^{t_0+\Delta t}=0 \qquad (1,1,0)\rightarrow 1$

if $\left(s_{j-1}^{t_0}=1, s_j^{t_0}=1, s_{j+1}^{t_0}=1\right)$

then $s_j^{t_0+\Delta t}=1 \qquad (1,1,1)\rightarrow 1$

In general, the number of rules can be calculated by $|S|^m$.

The general algorithm of a cellular automaton has the form:

Input data:

iT – number of iteration allowed to perform when computing the solution

C – number of initial configurations used for rule evaluation

Initialization:

a) For each cell *i* {

1. initialize rule table of cell *i;*
2. $s_i=0;$}

b) count=0; initial configuration counter

Iteration:

while not done do:

c) generate a random initial configuration

d) run the algorithm on initial configuration for *iT* iteration;

e) for each cell *i*

1. *if* cell *i* is in the final state then $s_i=s_i+1$

f) c=c+1

g) if c (mod C)=0 then

for each cell *i*

1. compute $ns_i(c)$ (number of neighbors)
2. if $ns_i(c)=0$ then don't change the rule of cell *i*
3. *else if* $ns_i(c)=1$ then replace the rule of cell *i* with the corresponding neighboring rule.
4. *else if* $ns_i(c)=2$ then replace the rule of cell *i* with the crossover of the two corresponding neighboring rules.
5. *else if* $ns_i(c)>2$ then replace the rule of the cell *i* with the crossover of the two randomly chosen neighboring rules.
6. $s_i=0$.

3. Cellular automata in recrystallization process

Transforming the abstract rules of a cellular automaton into a materials-related concept consists of mapping the values of relevant state variables onto the points of the cellular automaton and using the local finite difference formulations of the partial differential equations of the underlying model as local transformation rule. The particular versatility of the cellular automatom approach for the simulation of recrystallization process is due to its flexibility in considering a large variety of state variables and transformation laws. Cellular automaton simulations are carried out at an elementary level using atoms, cluster of atoms, small crystalline elements as underlying units. To model the recrystallization process, the most used was the two-dimensional cellular automata. As neighbors model (related as local environment), was used the von Neuman environment and the Moore environment (Fig. 1).

In [2] it is presented a straightforward application of cellular automata to recrystalization. It is focused on capturing three phenomena:

h) nucleation of grains

i) growth of grains

j) the slowing of growth owing to the impingement of grains.

The model used contains:

1. the geometry of the cells: a two-dimensional square network of cells,
2. the number and the kind of states a cell can possess: two states per site, recrystallized or not recrystallized,
3. the definition of the neighborhood of a cell: von Neuman and Moore (Figure 1.),
4. the rules that determine the state of each cell in the next time step: rules for nucleation of new grains, growth of grains, and the impingement of grains.

The initial configuration is with all sites set to zero (all cells correspond to no recrystallized state), and a number N_i of „embryos" were placed in system by assigning non-zero values to randomly selected nodes on the network. The strategy is to assign to each embryo a label to identify the grain that arose from that embryo. The rule to describe growth: if A≥1 at time step *t,* then the central site would be considered recrystallized at time step *t+1* and take on the identity of the grain that extends into its neighborhood. Here, A is defined as the sum of recristallized neghbors of the central node, based on the selected neighborhood. At each time step, the creation of another set of N_i embryos is attempted.

The N_d cells are chosen at random and if a cell was not recrystallized, an is created an embryo, with a sequential number. Thus all growing grains have their own unique identification number.

4. Conclusions

We have presented a general model for cellular automata, and a general automaton algorithm. The implementation of this algorithm depends on the dimension of the network of cells, the model of neighbourhood, and the number of initial configurations. The presented model and algorithm are prepared in order to be applied in the modelling of recrystalization process, and it is important to define these rules, corresponding to the considered phenomena.

References

[1]. Chopard B., Droz M. - *Cellular automata modelling of Physical Systems,* Cambridge University Press, (1998)
[2]. Hesselbarth H. W., Göbel I. R. - *Simulation of recrystallization by cellular automata,* Acta Metallurgica et Materialia, 39, (1991), 2135-2143
[3]. Pezee C. E., Dunand D. C. - *The impingement effect of an inert, immobile second phase on the recrystallization of a matrix* , Acta Metall. 42 (1994)
[4]. Marx V., Raabe D., Gottstein G. - *Simulation of the influence of recovery on the texture development in cold rolled BCC-alloys during annealing.* Proceedings 16th RISØ Int. Sympos. on Mat. Science: Materials: Microstructural and Crystallographic Aspects of Recrystallization, RISO Nat. Lab, Roskilde, Denmark eds. N Hansen, D Juul Jensen, YL Liu, B Ralph, (1995) 461-466.
[5]. Dierk Raabe - *Cellular automata in Materials Science with particular reference to recrystallization simulation,* Annual Review of Materials Research, 32, 2002, 53-76
[6]. Wolfram S. (ed.) - *Theory and applications of cellular automata,* Singapore: World Scientific, (1986).

THE ANNALS OF "DUNAREA DE JOS" UNIVERSITY OF GALATI.
FASCICLE IX. METALLURGY AND MATERIALS SCIENCE
N^0. 2 – 2013, ISSN 1453 – 083X

EFFECT OF SINGLE-WALL CARBON NANOTUBES ON THERMAL PROPERTIES OF POLYESTER COMPOSITES

Luminita CIUPAGEA, Virgil ILIUTA, Gabriel ANDREI
"Dunarea de Jos" University of Galati, Romania
email: luminitacotet@yahoo.com

ABSTRACT

This paper presents the effect of different contents of single-wall carbon nanotubes (SWCNT) on the specific heat and coefficient of thermal expansion of polyester composites. By adding small content of SWCNT in the matrix of the polyester, the specific heat increase compared to pure polyester. For a content higher than 0.15 wt% SWCNT, the coefficient of thermal expansion increases compared with pure polyester on cooling curve.

KEYWORDS*:* polyester, nanocomposites, SWCNT, thermal properties

1. Introduction

Unsaturated polyester is a polymer used in industrial applications as matrix for different type of composites. In recent years, nanomaterials have become the subject of intensive research. As for nanomaterials manifold, carbon nanotubes (CNT) attracted the attention of researchers because of their properties such as: low density, good stiffness, uncommon strength, exceptive electrical properties, excellent optical and thermal properties. By adding CNT into polymer matrix, a composite with better mechanical, thermal and electrical properties may be obtained.

In their study, Kucukyildirim et al added 1% wt multi-wall carbon nanotube (MWCNT) into polyester/glass fiber composite and they reported better mechanical properties such as tensile strength and toughness [1].

Other researchers used carbon nanofibers (CNF) into polyester matrix. Even small content of CNF, between 0.1 and 0.3 % wt, may increase the strength at flexural tests [2]. As regards thermal approach, a content between 1 and 3%wt MWCNT into polyester matrix improves thermal conductivity of the composite [3]. The biggest challenge regarding carbon nanotubes or nanofibers is the manufacture of an homogeneous composite by getting a good dispersion of the nanomaterial into polymer matrix. Mechanical stirring or ultrasonic methods are the most used techniques in order to obtain an homogeneous mixture. As for mechanical mixing, the more energy is higher, the dispersion is better. [4].

Scientific literature reveals other techniques which provide a suitable dispersion of CNT into polymer, such as: *in situ* polymerization or chemical functionalization [5].

2. Experimental results

2.1. Materials

The composites samples were prepared with commercial orthophtalic unsaturated polyester resin with 40% styrene (Norsodyne H 13271 TA). The main features of the resin are: density at 20^{o}C is 1.1g/cm^3, viscosity at 23^{o}C is 4.5 dPas, solid ranges between 56 – 60%, the working temperature was 23^{o}C and gel time was 12 min.

The methyl ethyl ketone peroxide was used as catalyst in order to initiate the polymerization reaction.

Single-wall carbon nanotubes, purchased from the company Cheap Tubes Inc., have a purity of over 90%, external diameter between 1 and 2 nm, internal diameter between 0.8 and 1.6nm, length between 5 and 30μm, specific surface 407m^2/g and density 2.1g/cm^3.

2.2. Preparation of the composites materials

Preparation of the composites materials was made using mechanical stirring technique. A short description of the procedure is related in this paragraph.

After weighting, the resin and single-walled nanotubes were placed into mortar for homogenization. Dispersion was performed by progressive addition of the polyester over SWCNT. After adding the entire amount of polymer, the

mixture was stirred by a magnetic stirrer for 1 hour, at 600rpm. Next step was degassing the mixture to remove bubbles air using a vacuum pump for 1 minute. The catalyst was introduced for starting the polymerization process. Homogenization of the catalyst inside the mixture mass was done using the stirring solution for 5 minute at 600 rpm, followed by a second degassing. Molding was performed using a vacuum pump to avoid the formation of the voids into composite. Finally, the polymerization was completed by placing the materials into oven for 8 hours, at 70^{o}C.

The following samples were prepared:

- polyester composite with 0.10% wt SWCNT;
- polyester composite with 0.15% wt SWCNT;
- polyester composite with 0.20% wt SWCNT.

These composites and pure polyester were tested for determination of specific heat and coefficient of thermal expansion.

2.3. Method for determining the specific heat

The **specific heat** of the materials was determined based on differential scanning calorimetry data recorded with a (DSC) instrument, type DSC1 Star System Mettler Toledo.

The testing method for all the samples consisted of following steps:

1. Keeping the sample at 30^{o}C for 5 minutes;
2. Heating the sample from 30^{o}C to 130^{o}C with a rate of 10^{o}C/min.
3. Keeping the sample at 130^{o}C for 5 minutes;
4. Cooling the sample from 130^{o}C to 30^{o}C with a rate of 10^{o}C/min.

The specific heat value was calculated by the relation:

$$c = \frac{Q}{m \cdot (T_2 - T_1)}$$

where c is the specific heat (J xg^{-1}×^{o}C^{-1}), Q is the heat flow (J), m is specimen mass, (g), T_1, T_2 are heating temperatures from start and end points (^{o}C).

The specific heat values for all tested materials was calculated in the range of 70 - 110^{o}C for both heating and cooling curves. In this range, the material behaviour can be considerated rather liniar, as shown figure 1.

The determination of the **thermal expansion coefficient** was done using a thermo mechanical analyzer (TMA) type TMA – SDTA 840, Mettler Toledo.

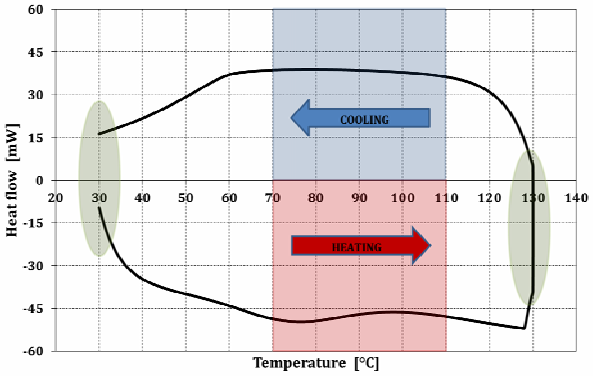

***Fig. 1.** Graph of the heat flow depending on the temperature for tested materials*

Testing method consist of following steps:

1. Keeping at 30^{o}C for 5 minute;
2. Heating from 30^{o}C to 130^{o}C with a thermal rate of 10^{o}C/min under a 0.02N loading;
3. Keeping at 130^{o}C for 5 minute;
4. Cooling from 130^{o}C to 30^{o}C with a thermal rate of 10^{o}C/min under a 0.02N loading.

Linear thermal expansion coefficient was calculated using the formula:

$$\alpha = \frac{L}{\Delta L \times \Delta T}$$

where α thermal expansion coefficient, (10^{-6}/^{o}C), L is initial length of the sample (mm), ΔL is the difference between final and initial length of the sample (mm); ΔT is the difference between final and initial temperature of the sample (^{o}C).

The values of the coefficient of thermal expansion were calculated into the interval 70 – 110^{o}C.

3. Results and discussion

3.1. Specific heat

The experimental results for specific heat of the polyester nanocomposite and pure polyester, on the heating curve, are shown in the Figure 2. From the graph it can be seen that the polyester nanocomposites with SWCNT have greater values for specific heat. This means that small amounts of well dispersed SWCNTs could improve the specific heat of the composite. From the graphs presented in the Figures 2 and 3 it can be seen that all the nanocomposites shown better values for specific heat as compared to pure polyester. The value of specific heat increases with 63%, in case of 0.10% wt SWCNT, with 69% for 0.20% wt SWCNT and with 76% for 0.15% wt SWCNT, all values compared with the specific heat of polyester.

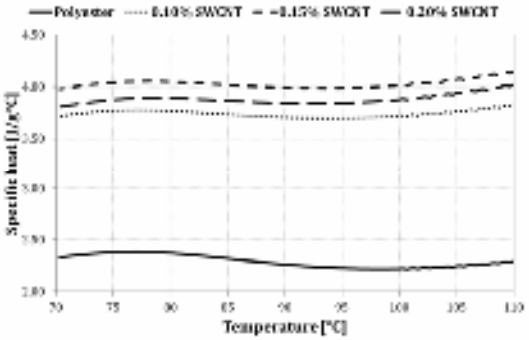

Fig. 2. *Variation of the specific heat for polyester and polyester nanocomposite with different content of SWCNT on heating curve*

The figures 4 and 5 show the specific heat values on cooling curve. All values for nanocomposites are bigger compared with specific heat of pure polyester.

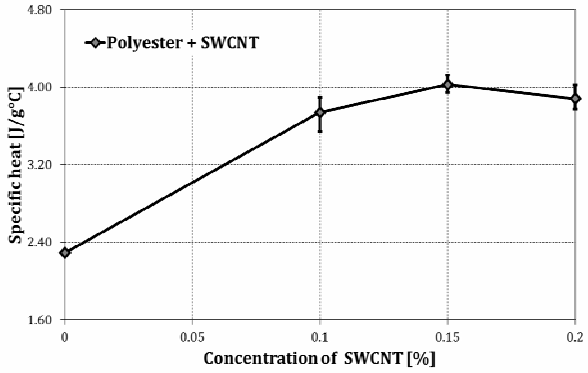

Fig. 3. *Variation of the specific heat depending on the content of SWCNT added into polyester, on heating curves*

On cooling curve, the polyester nanocomposite with 0.15% wt SWCNT has the higer value from all tested materials as is shown in figure 4.

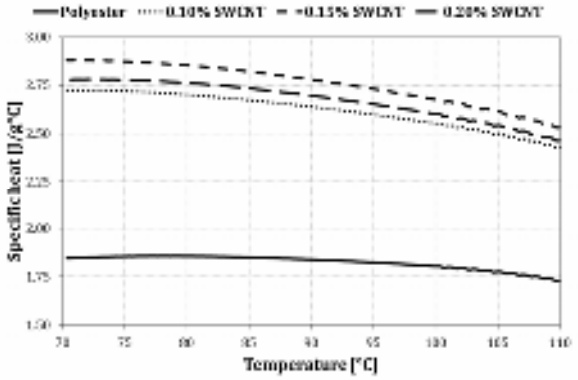

Fig. 4. *Variation of the specific heat for polyester and polyester nanocomposite with different contents of SWCNT on cooling curve*

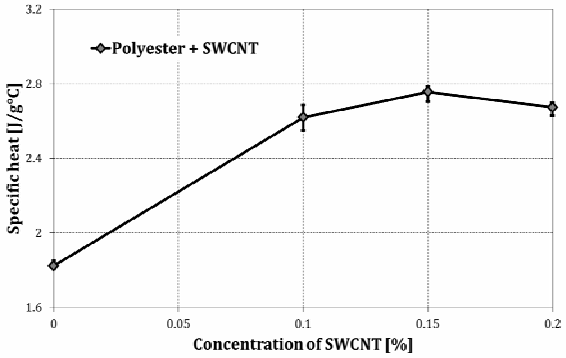

Fig. 5. *Variation of the specific heat depending on content of SWCNT added into polyester, on cooling curves*

As for nanocomposite with 0.10% wt SWCNT, specific heat increase with 44%, for 0.15% wt SWCNT, with 51% and for 0.20% increase with 47%, all values were compared with specific heat of polyester.

3.2. Coefficient of thermal expansion

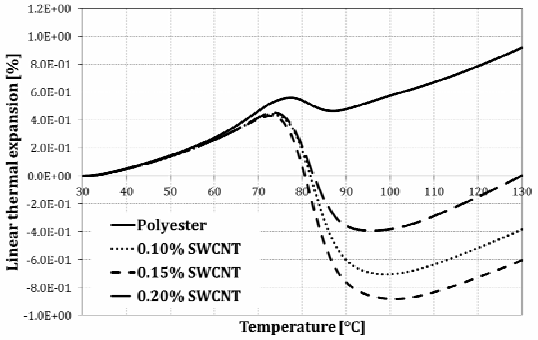

Fig. 6. *Evolution of linear thermal expansion with temperature for polyester and SWCNT composites on heating curve*

Regarding the linear thermal expansion on heating and cooling curves, the experimental results reveled different situation as shown in Figures 6 and 7.

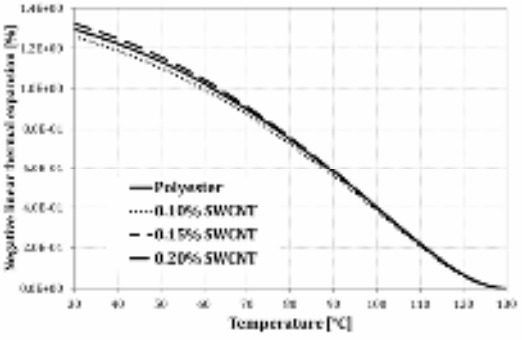

Fig. 7. *Evolution of linear thermal expansion with temperature for polyester and SWCNT composites on cooling curve*

On heating curves (Figure 6) all of nanocomposites have an increasing trend for linear expansion until the glass transition temperature (Tg) value is achieved. After this point, practically between 70 and 100^{o}C, the curve has a descending trend, reaching negative values for thermal expansion. The neat polyester has a small decrease after Tg, in the interval 75-90^{o}C, over this range, thermal linear expansion increase. It can be concluded that in case of nanocomposite beyond Tg there is a rearrangement of molecules within material.

On cooling curves, negative linear thermal expansion, for all of tested materials, has a almost similar evolution, with small differences, as is shown in Figure 7.

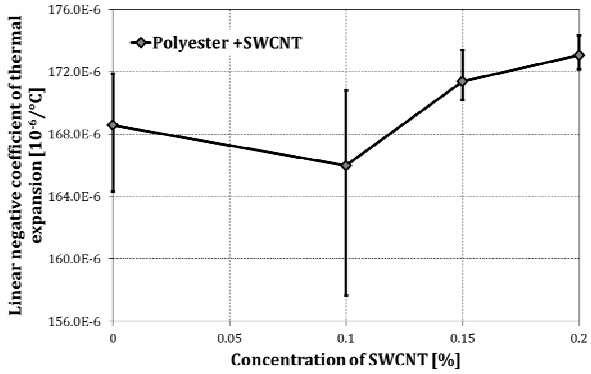

Fig. 8. *Variation of linear negative coefficient of thermal expansion depending on the content of SWCNT added into polyester, on cooling curves*

Figure 8, shows that, except polyester composite with 0.10% wt, all of nanocomposites have increasing values for linear negative coefficient of thermal expansion, compared with neat polyester. The biggest value was obtained for polyester nanocomposite with 0.2%wt SWCNT.

4. Conclusion

The aim of this work was to determine the important thermal properties of polyester and polyester composites with small contents of SWCNT.

The experimental results shown that the specific heat of nanocomposite increase for both heating and cooling curves. The biggest value for specific heat was obtained for nanocomposite with 0.15 wt % SWCNT on heating curves, the increasing was 76% compared with polyester value.

Concerning the coefficient on thermal expansion calculated on cooling curves, the polyester nanocomposites with 0.15 wt % and 0.20 wt % shown increased values compared with polyester value.

Acknowledgement

This work was carried out with the support of the Project POSDRU - 76822 TOP ACADEMIC.

References

[1]. Kucukyildirim, B.O. et al - Mechanical Behavior of Industial Grade MWCNT and Glass Fiber Reinforced Polyester Hybrid Nanocomposites, *International Journal of Arts and Sciences* 3 (9), (2010), pp.252-257.

[2]. Hossain, M.K. et al. - Flexural and Compression Response of Woven E-glass/Polyester-CNF Nanophased Composites, *Composites: Part A42*, (2011), pp. 1774-1782.

[3]. Wang, S. et al. - Enhancing Thermal Conductivity of Glass Fiber/Polymer Composites Through Nanotubes Incorporation; *Composites Part B: Engineering, Vol. 41, Issue 7*, (2010), pp. 533-536.

[4]. Agullo, J-Vera et al. - Comparative Study of the Dispersion and Functional Properties of Multiwall Carbon Nanotubes and Helical – Ribbon Carbon Nanofibers in Polyester Nanocomposites, *Composites Science and Technology 69*, (2009), pp. 1521 – 1532.

[5]. Xie, X-L et al. - Dispersion and Alignment of Carbon Nanotubes in Polymer Matrix: A Review, *Materials Science and Engineering* R 49, (2005), pp 89-112.

[6]. Alsina, O. L.S. et al, 2005, Thermal properties of hybrid lignocellulosic fabric-reinforced polyester matrix composites, *Polymer Testing* 24, Issue, pp.81-85.

[7]. Ashby, M. - *Materials Selection in Mechanical Design*, Second Edition, Ed. Elsevier Butterworth – Heinemann, pp. 22 -28.

[8]. Crawford, R. J., 1998, *Plastics Engineering*, Third Edition, Ed. Elsevier Butterworth – Heinemann, (1999), p.7.

[9]. Morgan, P.- *Carbon Fibers and Their Composites*, Ed Taylor and Francis Group, (2005), p 537.

[10]. Moreira, D.C. - Experimental investigation of heat conduction in polyester – Al2O3 and polyester – CuO nanocomposites; *Experimental Thermal and Fluid Science*, Vol.35, Issue 7, (2011), pp. 1458-1462.

[11]. Ruban, Y. J. V. et al. - Mechanical and Thermal Studies of Unsaturated Polyester – Toughened Epoxy Composites Filled with Amine-Functionalized Nanosilica; Appl. Nanosci, (2011).

THE ANNALS OF "DUNAREA DE JOS" UNIVERSITY OF GALATI.
FASCICLE IX. METALLURGY AND MATERIALS SCIENCE
N^0. 2 – 2013, ISSN 1453 – 083X

PREPARATION AND CHARACTERIZATION OF Tin OXIDE THIN FILMS

***N. TIGAU[1], D. C. VLADU RADU[1], G. PRODAN[2], C. GHEORGHIES[1], S. CONDURACHE-BOTA[1]**

[1]Faculty of Sciences and Environment, Chemistry, Physics and Environment Department, „Dunarea de Jos" University of Galati, Romania
[2]Ovidius University of Constanta, 124, Mamaia Street, 900527, Constanta, Romania
*Corresponding author
email: ntigau@ugal.ro

ABSTRACT

Tin oxide (SnO) thin films were prepared onto glass substrates by thermal evaporation under vacuum. The substrate temperature was kept constant at 300 K during the film growth. The structural studies using transmission electron microscopy (TEM) analysis showed that the SnO thin films have a polycrystalline and tetragonal crystal structure with preferential orientation of (110) planes parallel to the substrate. Optical transmission and reflection spectra, at normal incidence, in the spectral range 300-1100 nm, are investigated. The optical properties of SnO thin films were determined. The optical energy band gap, E_g, has been estimated from the absorption coefficient values using Tauc's procedure. It is found that the SnO thin films exhibit direct band gap.

KEYWORDS: thermal evaporation, tin oxide, TEM, optical properties

1. Introduction

In recent years, transparent conducting oxide films have attracted the researchers due to their potential use in a variety of applications including optoelectronic devices, such as solar cells, flat panel displays, light emitting devices and gas sensors [1-5]. Among the transparent conducting oxide films, tin oxide exhibitts interesting physical properties suitable for these applications.

There are different methods of depositing tin oxide thin films, in particular spray pyrolysis [6,7], magnetron sputtering [8], pulsed laser ablation [9], chemical routs by using sol-gel [10] and thermal evaporation technique [11]. In the present work, the ojective was to prepare SnO thin films by vacuum thermal evaporation technique and to study the structural and optical properties of these films.

2. Experimental research

SnO thin films were deposited on highly clean glass substrates by thermal evaporation under vacuum ($p=10^{-5}$ torr) of SnO_2 powder (Sigma Aldrich, purity 99.99%). The glass substrate was kept at a temperature of 300K during deposition of thin films and the thickness of SnO thin films was measured by interferometric method [12] using a Linnik microscope.

The thickness of investigated samples was d=0.10 μm. The microstructural characteristics of the SnO thin film such as morphology, particle size and crystal structure were analyzed by transmission electron microscopy (TEM). The TEM investigation was performed on a Philips CM-120 electronic microscope with an accelerating voltage of 120kV.

Optical transmission and reflection spectra were recorded in the wavelength range of 300-1100nm using Perkin Elmer Lambda 35 UV-Vis Spectrometer and UV Win Lab software.

3. Results and discussion

The investigated SnO thin films were adherent, uniform and covered well over the substrate. The electron diffraction was used for determining the structural phases of SnO thin films. Selected area electron diffraction (SAED) patterns were taken from

selected areas in the SnO thin films. Figure 1 shows the SAED patterns of the SnO thin film deposited at substrate temperature of 373K. Six intense diffraction rings shown are corresponding to diffraction from (101), (200), (220), (211), (321) and (312) planes. The SnO thin film deposited at 300K exhibits the polycrystalline structure and corresponds to a tetragonal rutile structure. The crystallites are preferentially oriented with the (101) planes parallel to the substrate surface. Lattice spacing, d_{hkl}, was calculated using Bragg's equation together with the Miller indices and the calculated values of d_{hkl} are inserted in SAED pattern.

The lattice parameters, a and c, of SnO polycrystalline thin films, with a tetragonal structure, were calculated using the relation [11, 12]:

$$d_{hk\ell} = \frac{1}{\sqrt{\frac{h^2+k^2}{a^2}+\frac{\ell^2}{c^2}}} \quad (1)$$

where h, k and ℓ are Miller`s indices corresponding to ($hk\ell$) lattice plane. The values of lattice parameters were found to be a=4.75Å and c=3.08Å, respectively. These values are in good agreement with those reported recently in Ref. [6,11,14,15] for SnO thin film.

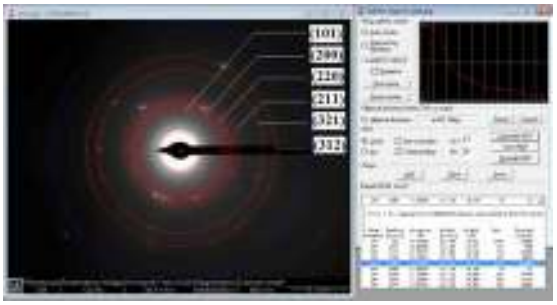

***Fig. 1**. SAED pattern of SnO thin film*

Figure 2(a) shows bright-field transmission electron microscopy (BF-TEM) images recorded from plan view specimens, showing that SnO thin films exhibit a grainy structure which consists of many small grains of relatively uniform size forming morphologically homogeneous films. The size distributions of the crystallites, obtained from measurements on around 400 grains, are plotted in Fig. 2(b).

The distributions of grain sizes, as measured from BF-TEM images, were fitted to the lognormal curves [16,17]. The mean grain size, x_c, was found to be around 12.26nm (Fig. 2b).

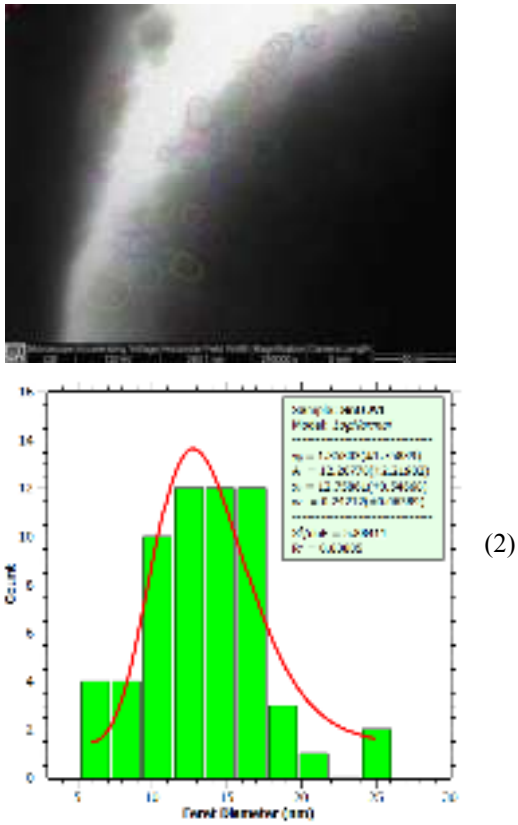

(2)

***Fig. 2**. (a) BF-TEM images of SnO thin films, (b) Grain size distribution of the SnO thin film*

Figure 3 shows the optical transmittance (T%) and reflectance (R%) spectra of SnO thin films deposited at the investigated substrate temperature. The thin films exhibit more than 75% of transmittance in the visible and near-infrared wavelength regions with some interference fringes and sharp ultraviolet absorption edges. Also, in Fig. 3 it can be seen that all samples show reflectance more than 25% the for whole investigated wavelength range.

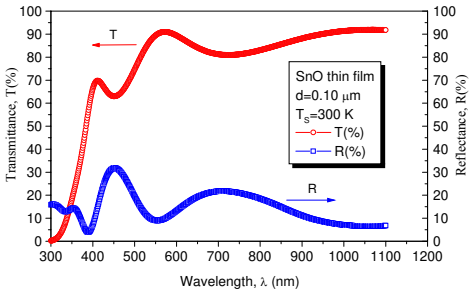

***Fig. 3.** Transmission and reflection spectra of SnO thin film*

The absorption coefficient, α, was calculated by relation [18-20]:

$$\alpha = \frac{1}{d}\ln\frac{(1-R^2)}{T} \quad (2)$$

where d=0.10 μm is the film thickness, T the transmittance and R reflectance of the SnO thin film. The variation of absorption coefficient with wavelength is shown in Fig. 4.

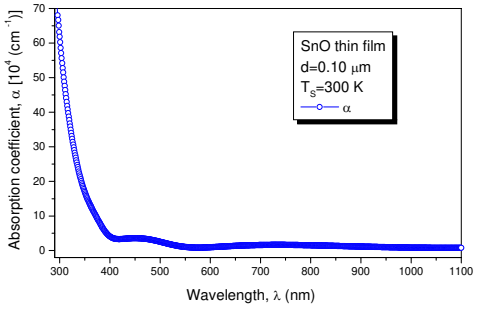

***Fig. 4**. Variation of absorption coefficient of SnO thin film*

The optical band gap energy, E_g, can be estimated from the fundamental absorption edge of SnO thin films. Assuming the allowed direct transition between valence and conduction band, the values of optical band gap of SnO thin films were determined from the dependence of absorption coefficient, α, on the photon energy, hν, using Tauc`s relation [20-22]:

$$\alpha h\nu = A(h\nu - E_g)^{1/2} \quad (3)$$

where A is a parameter that depends on the transition probability. Figure 5 exhibits the plots of $(\alpha h\nu)^2$ versus photon energy, hν. The E_g values are determined by extrapolating the linear portion of the curves to the hν axis. The obtained value of optical band gap energy was found to be 3.78eV; which is in good agreement with those found in literature for this kind of thin films [8,10,23-28].

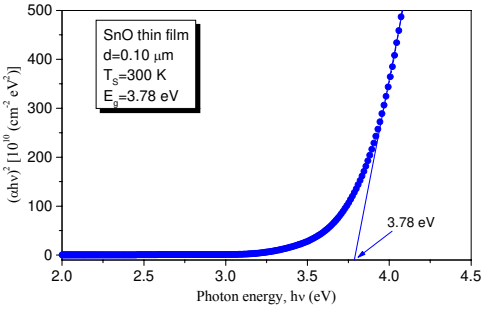

***Fig. 5.** The $(\alpha h\nu)^2$ versus $(h\nu)$ plot for investigated SnO thin film*

4. Conclusions

SnO thin films were deposited at substrate temperature of 300 K using the thermal evaporation technique. The TEM patterns showed that the films is polycrystalline with tetragonal rutile structure. The obtained values of lattice parameters were: a=4.75Å and c=3.08Å, respectively. The mean grain size was found to be around 12.26nm. Transmission and reflection spectra in the wavelength range 300-1100 nm were used to calculate the absorption coefficient and optical band gap energy. The value of optical band gap energy evaluated from absorption spectra was found to be 3.78 eV which is in good agreement with literature.

References

[1]. A.L. Dawar, J.C. Joshi - *J. Mat. Sci.* 19, 1, (1984).
[2]. B. Russo, G.Z. Cao - *Appl. Phys. A.* 90, 311, (2008).
[3]. P.S. Patil, S.B. Sadale, S.H. Mujawar, P.S. Shinde, P.S. Chigare - *Appl. Surf. Sci.* 253, 8560, (2007).
[4]. C.M. Lampert - *Solid Energy Mater.* 6, 1, (1981).
[5]. D.S. Lee, Y.T. Kim, J.S. Huh, D.D. Lee - *Thin Solid Films* 416, 271, (2002).
[6]. P.S. Shewale, S.I. Patil, M.D. Uplane - *Semicond. Sci. Technol.* 25, 115008, (2010).
[7]. E. Elangovan, S.A. Shivashankar, K. Ramamurthi - *J. Cryst. Growth* 276, 215, (2005).
[8]. D. Beena, K.J. Lethy, R. Vinodkumar, V.P. Mahadevan - *Sol. Energ. Mat. C.* 91, 1438, (2007).
[9]. J. Montero, J. Herrero, C. Guillen - *Sol. Energ. Mat. C.* 94, 612, (2010).
[10]. B. Benrabah, A. Bouaza, S. Hamzaoni, A. Dehbi - *Eur. Phys. J. Appl. Phys.* 48, 30301, (2009).
[11]. A. Sharma, D. Prakah, K.D. Verma - *Optoelecton. Adv. Mat.* 1(12), 683, (2007).
[12]. C. Gheorghies, L. Gheorghies, R. Chirila - *Roentgenocristalografie,* Ed. Tehnica, Bucuresti, (1994).
[13]. K. L. Chopra - *Thin Film Phenomena*, McGraw-Hill, New York Book Co. 101, (1969).
[14]. S. Sambhaji, S. Bhande, Gauri A. Taur, Arif V. Shaikh, Oh-Shim Joo, Myung-Mo Sung, Rajaram S. Mane, Anil V. Ghule, Sung-Hwan Han - *Mater. Lett.* 79,29, (2012).
[15]. Y. Liu, Y. Dong, G. Wang - *Appl. Phys. Lett.* 82(2), 260, (2003).
[16]. N. Tigau, V. Ciupina, G. Prodan, G.I. Rusu, E. Vasile - J. *Cryst. Growth* 269, 392, (2004).
[17]. M. Huang, Y. Wang, Y. Austin Chang, *Thin Solid Films* 449, 113, (2004.
[18]. F. Aousgi, M. Kanzari - *Energy Procedia* 10, 313, (2011).
[19]. G.I. Rusu, M.E. Popa, G.G. Rusu, Iulia N. Salahoru - *Appl. Surf. Sci.* 218, 213, (2003).
[20]. T. S. Moss, M. Balkanski, (eds) - *Handbook on Semiconductors, Optical Properties of Semiconductors,* North-Holland, Elsevier, Amsterdam, (1994).
[21]. N.F. Mott, E.A. Davis - *Electronic Processes in Non-Crystalline Materials,* Clarendon Press, Oxford, (1971.
[22]. N. Tigau, V. Ciupina, G. Prodan - *J. Cryst. Growth* 277, 529, (2005).
[23]. S. Condurache-Bota, N. Tigau, A.P. Rambu, G.G. Rusu, G.I. Rusu - *Appl. Surf. Sci.* 257, 10545, (2011).

[24]. H. R. Fallah, M. Ghasemi, A. Hassanzadeh, H. Steki - *Physica B* 373, 274, (2006).
[25]. S. S. Lekshmy, L.V. Maneeshya, P.V. Thomas, K. Joy - *Indian J. Phys.* 87, 33, (2013).
[26]. N. F. Habubi, K.A. Mishjil, S.S. Chiad - *Indian J. Phys.* 87(3), 235, (2013).
[27]. C.Gheorghies, L. Gheorghies - *Nanomateriale si Nanotehnologii,* Ed. CERMI, Iasi, (2008)
[28]. L. Gheorghies, A. Sion - *Obţinerea şi analiza acoperirilor metalice de protecţie,* Ed. CERMI, Iaşi, (2012).

THE ANNALS OF "DUNAREA DE JOS" UNIVERSITY OF GALATI.
FASCICLE IX. METALLURGY AND MATERIALS SCIENCE
N^0. 2 – 2013, ISSN 1453 – 083X

CHARACTERIZATION OF THE DENTAL METALS AND ALLOYS

***Elisabeta VASILESCU[1], Vlad-Gabriel VASILESCU[2]**
Alexandru Mircea NICOLAU[2]
[1]"Dunărea de Jos" University of Galati, Faculty of Materials and Environment Engineering,
47, Domnească Street, RO-800008, Galati, Romania
[2]"Carol Davila" University of Bucuresti, Faculty of Dentistry Medicine,
Dionisie Lupu Street, 37, Bucuresti, Romania
*Corresponding author
email: elisabeta.vasilescu@ugal.ro

ABSTRACT

Metals and alloys in dentistry have seen remarkable progress due to their biocompatibility and deepen research on the application of advanced technologies to improve surface properties by controlling interactions material - environment in the mouth. Biocompatibility of metals is a consequence of the presence of surface oxide layer. Chemical properties and therefore chemical processes determine precisely this interface oxide layer and not the metal itself. Biocompatibility would be perfect without any biomaterial - tissue interactions and could be assured by a completely inert biomaterial, which does not exist at this time. Titanium and its alloys provide strength, rigidity, and ductility similar to those of other dental alloys. Whereas, pure titanium castings have mechanical properties similar to Type III and Type IV gold alloys, some titanium alloy castings, such as Ti-6Al-4V and Ti-15V, have properties closer to Ni-Cr and Co-Cr castings with the exception of lower modulus. Co-Cr alloys are alloys nenobile group, developed as an alternative to noble alloys, which have become very expensive, inaccessible and limited resources. Modern alloys based on Co-Cr, due to its superior mechanical and cost-effective price noble alloys have replaced the classic class IV in technology (metal-polymer) and modern (metal and metal-ceramic composite). Co-Cr alloys have advantages related to high modulus (250GPa) than type IV gold alloys (70-100GPa) but they maintain their rigidity, which means that all items may have minimum thickness metal frame.

This article presents a few considerations and results of studies regarding the biological behavior and corrosion resistance of the commercially pure titanium (CP Ti), titanium alloys (e.g. Ti6Al4V), in comparison with other alloys (stainless steel, Co-Cr alloys) used in prosthetic or orthodontic implant technology.

KEYWORDS: biocompatible metallic material, corrosion resistance, biological behavior, titanium and titanium alloys, stainless steel, cobalt- chromium alloys

1. Introduction

Metallic biomaterials represent an important class of materials for dentistry due mainly to their mechanical properties and an acceptable biocompatibility. The biocompatibility of dental materials depends on their composition and on the location and interaction of the oral cavity.

Material response to changes in pH, the application of force or the degradative effects of fluids may affect bio-compatibility. The main issues to be considered when using metallic materials as biomaterials in dentistry (dentures, implants) include: the corrosion, release of toxic metal ions, attrition and lack of elasticity. Toxicity of metal ions as particles resulting from wear are the main disadvantages of using metallic materials as biomaterials, as they can induce multiple tissue reactions, including osteolysis, degradation of the normal bone structure, severe reaction of macrophages, granulomas, fibrous capsule, inflammatory and immune reactions. All this can lead to destabilization and weakening of

prostheses and implants. In general, corrosive metals determine an acute toxic reaction.

2. Comparative study of the corrosion resistance and biocompatibility of dental metals and alloys (titanium, titanium alloy, stainless steel, cobalt-based alloys)

A study on the resistance to corrosion of biomaterials for implants [10], expressed by the rate of corrosion and the rate of formation of corrosion products in Hank's solution resulted in the following data (table 1) [10, p.67]. Among metals for medical applications, the best biocompatible titanium has the highest potential scale ABE-Anodic Back Electromotive Force determined in blood serum at 37^{0}C [8] and is well tolerated by living cells without place changes in their functions. Titanium implant is preferred because it has low density (4.5g/cm^3) compared to stainless steel (7.9g/cm^3 for 316) and 8.3g/cm^3 and 9.2g/cm^3 for cast CoCrMo or CoNiCrMo forged), good mechanical and chemical properties. According to some authors, titanium alloys are better tolerated than pure titanium, since the oxide layer formed has a larger thickness (10-20μm) which is regenerated every nanosecond. Stainless steel is categorized as widely used in the past because they were cheap, durable, easily obtained and processed. Decrease in carbon content and addition of moliben (316L grade steel) had the effect of increasing the corrosion resistance. Another large group of alloys used to make implants and prostheses are Co-Cr alloys (or stellites). Chromium is the main alloying element that increases corrosion resistance and oxidation by the formation of oxide film (Cr_2O_3) on the surface. Co-Cr alloys exhibit characteristics similar to the stainless steels and have the advantage of practically zero toxicity.

We studied the corrosion behavior of the alloy Co-Cr (the metal material used in biomedical applications, fig.1) in aqueous solution with different pH, because it is known that all vital processes in the body is carried out in the exact values of pH. Were selected three types of media, so-called artificial saliva with different pH values: Hank (pH 7.4), artificial saliva Saliva Fusayama Meyer (pH 5.0) and Ringer's saliva (pH 6.6). The electrochemical cell used during the experiment is made up of the working electrode (WE) - Co-Cr alloy, reference electrode Ag / AgCl (saturated KCl solution, E = 200mV/NHE) (RE), the auxiliary electrode (EC)- Pt-Rh grid. After corrosion tests carried out in the four solutions / artificial saliva, the samples were subjected to microscopic analysis. Areas with aspects of localized pitting corrosion phenomenon highlighted the qualitative analysis by electron microscopy (SEM - Scanning Electron Microscope, fig.) were further investigated specific techniques EDS equipment - Energy-dispersive X-ray spectroscopy quantitative analysis (Fig.2, Fig.3). The fields that indicate susceptibility of alloy studied was revealed: the chemical composition of the alloy examined, variation of concentration of an element in a particular area of interest (pitting)- three dimensional version of the distribution of chemical elements over an area that includes the points of corrosion.

Table 1. *Chemical composition and mechanical properties of Co-Cr alloy [10, p.67]*

Chemical composition, %									
Specification	EN 10204 -3.1B	Co	Cr	Mo	Mn	C	Fe	Si	Sonstige
	max. [%]	63	29.4	5.95	0.6	0.29	0.05	0.7	0.1

Properties		
Density [g/cm^3]	**Hardness**, HV10	**Modulus of elasticity, E** [MPa]
8,3	420	230,000

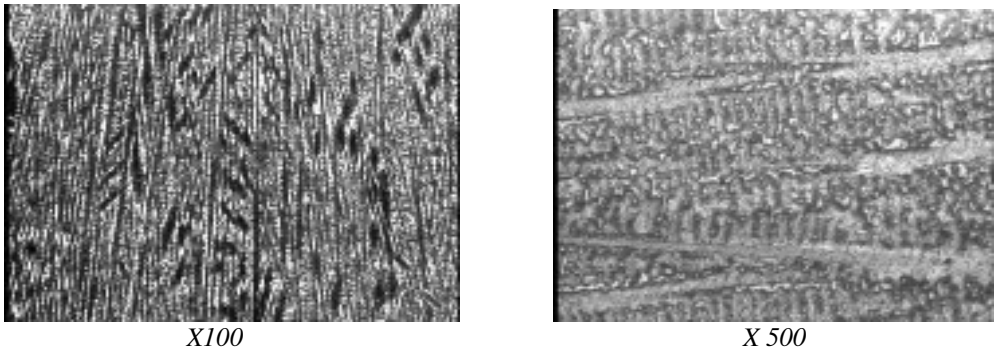

X100 *X 500*

Fig. 1. *Microstructural aspects of CoCr dental alloy samples (optical microscopy) [10, p.68]*

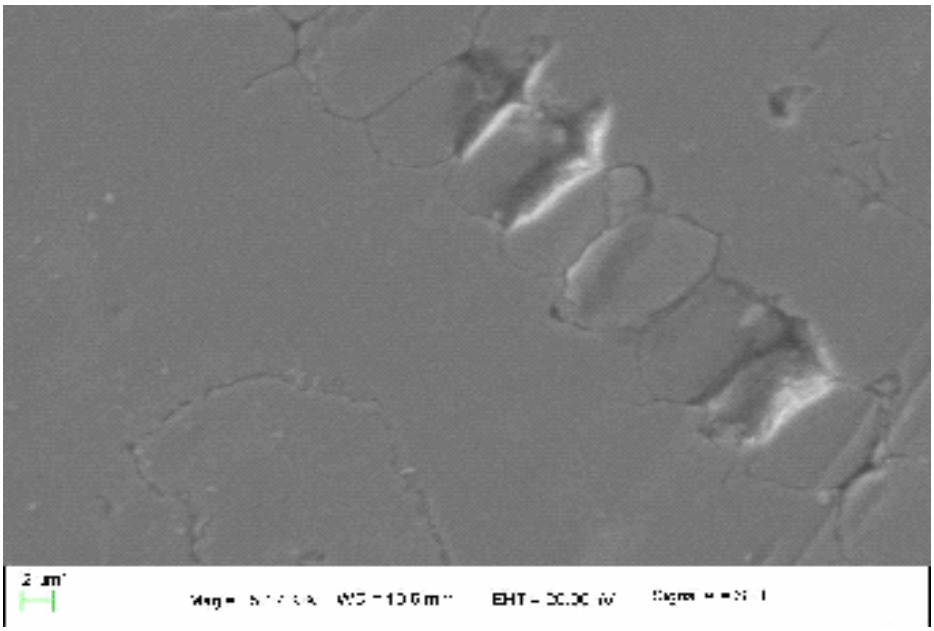

Fig. 2. *CoCr dental alloy /Micrographic issues - details of areas affected by corrosion (pitting) (Magnification: 5000 X, using detectors BSE - Back-Scattered Electron Detector and SE- Secondary Electron Detector) [10, p.80]*

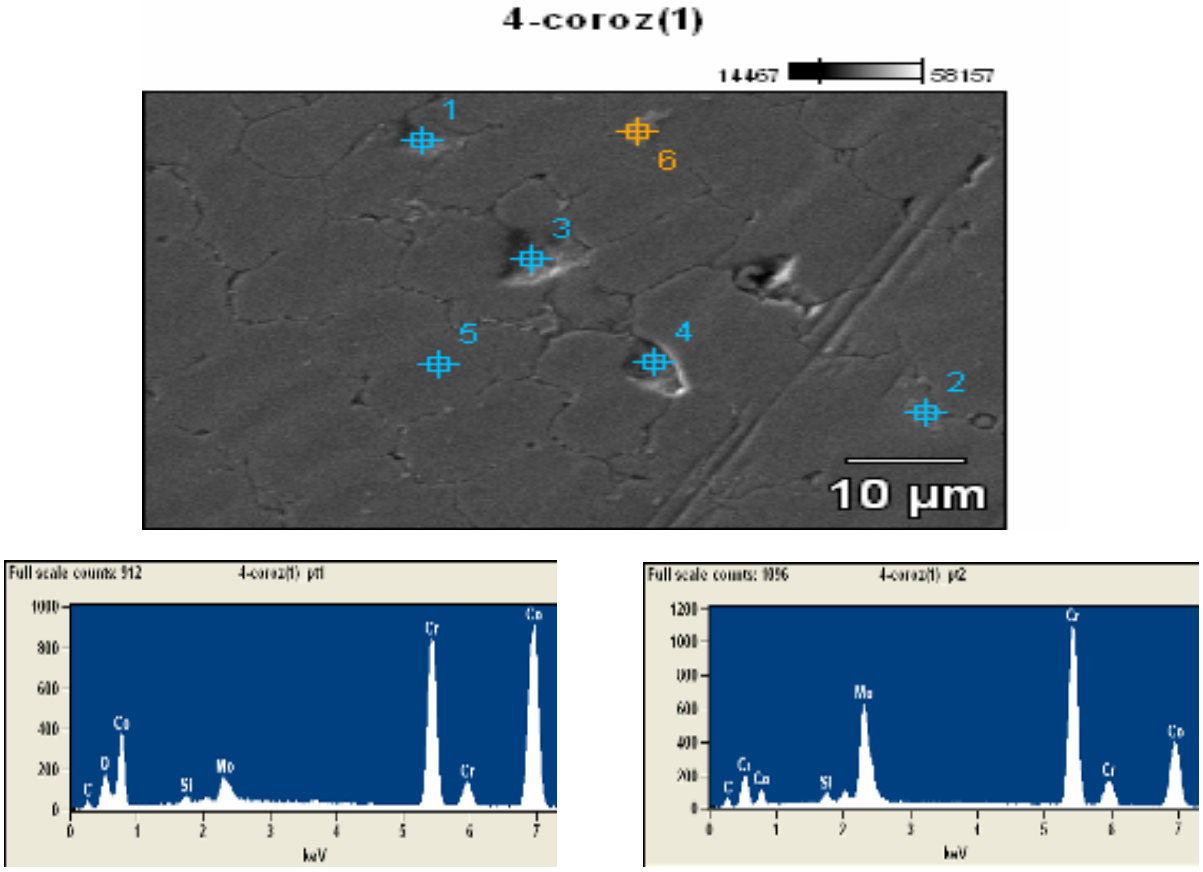

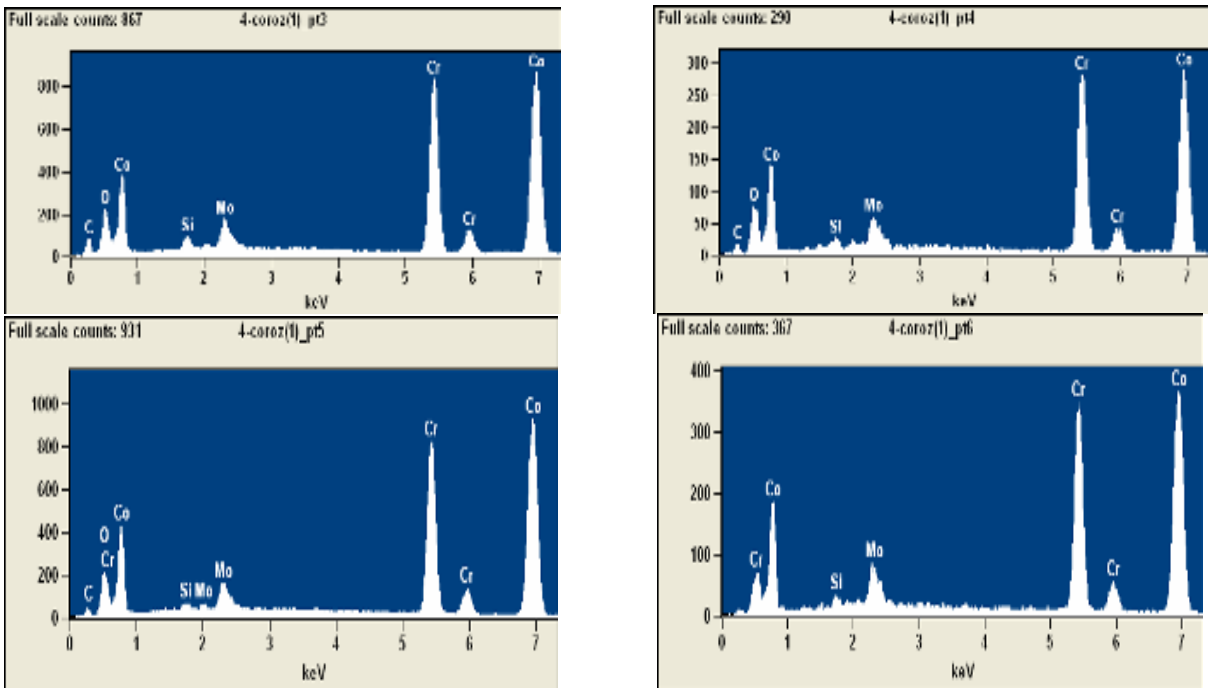

Fig. 3. *CoCr dental alloy (sample 4)/*
The pitting areas revealed by the quantitative analysis with SEM

Table 2. *Corrosion rates of biomaterials in Hank's solution [8]*

Alloy	**Metal transformed into compounds** [ng/m²h]	**Metal found in tissue** [ng/m²h]
Stainless steel - polished mechanically	7.8	0.274
(AISI 316L) - chemically polished	230	-
Vitalium - mechanical polishing	150	0.249
alloy (Co-Cr-W-Ni), the chemical polishing	20	-
Ti - mechanical polishing	4.1	0.430
- chemical polishing	3.5	-
Ti-16Mo	1.5	-
Ti-5Ta	0.26	-

Table 3. *Potential drops in Hank's solution and time repassivation of metallic biomaterials in 0.9%NaCl [8]*

Metallic biomaterials	**Potential drops**	**Repassivation time**			
		t^c		$t^{0,05}$	
	[V]	[s]			
AISI 316	+0.2-0.3	>72000	35	>>7200	6000
CoCr	**+0.42**	**44,4**	**46**	**>>6000**	**6000**
CoCrNi	+0.42	35.5	41	>6000	5300
TiAl6V4	**+2.0**	**37**	**41**	**43.3**	**45.8**
Ti	**+2.4**	**43**	**44.4**	**47.4**	**49**
Ta	+2.25	-	-	-	-
Nb	-	47.6	43.1	47	85

3. Comparative study of biological properties of some metals and alloys used in dentistry

Biomaterial surface reactivity and living tissue response are measured by the degree of biocompatibility. From this point of view, biomaterials can be: biotolerante (e.g. bone implant is separated by a layer of soft tissue) bioinerte (they do not cause migrations of ions in living environment they do not influence biochemical living cells do not lead to rejection phenomena), bioactive (connection between implant and tissue is made without the use of binders).

From the literature we can draw some general questions relating to metallic biomaterials toxicity, as follows:

Aluminum negative influence on bone metabolism in that it inhibited the phosphorylation and ATP synthesis, thereby reducing cellular energy reserves. Regarding alumina (Al_2O_3), the main compound of aluminum, we can say that it has no toxic effect due to its low solubility, even promoting cell proliferation. Cobalt is considered an essential element of life. After nickel and cobalt chrome stands between allergenic metals.

Chromium and it also belongs to the group of elements essential to life. Toxicity depends on the oxidation state in which it is located. Hexavalent chromium is more toxic than trivalent chromium and is considered a potent mutagen and carcinogen. Trivalent compounds do not penetrate through the skin or cell membrane and bind to the stable protein complex. In contrast, hexavalent compounds have a greater power of oxidation of organic molecules, passing easily through cell membranes and are reduced to the more stable trivalent form, which penetrates the nucleus and induce mutations in DNA interactions.

Nickel is one of the most studied factors related to effects on the human body. He ubiquitous in our environment and is absorbed inland digestive, respiratory, skin or metal implants, inhalation, implantation, ingestion, intraperitoneal injection, intramuscular or intravenous. The amount of nickel in blood and urine is an accurate indicator of intoxication with this metal. Nickel has high affinity for microsomal and mitochondrial proteins of pneumocytes, which are mainly based on energy storage cell reserve and location of complex enzyme systems. Nickel compounds such as Hydrocarbonate, sulfides or oxides of nickel activate interleukin production and lipid peroxidation, thus generating free radicals, which are potentially highly carcinogenic. Nickel is considered as the most sensitizing metal soft tissue. It leads to allergic contact dermatitis, allergic reactions producing more alergies than all other metals combined. Vanadium lowers concentrations of coenzyme A and Q by disinhibition oxidative phosphorylation, interferes with many enzyme systems and can induce irreversible disruption. High solubility contributes to the toxic effects that are estimated to be 10 times larger than the Ni-Co-Cu complex. Aluminum and vanadium elements are released into tissues. Metal ions released from corrosion and wear can induce hearing loss after a long period of implantation, especially because of the potential adverse effects of vanadium. Release of vanadium ions in the body can produce serious organ damage and, also, can produce platelets systems. For this reason it is preferable alloy Ti-Al-Nb-Ti alloy instead of Al-V. In vitro studies showed that the cells behave differently in the presence of debriurilor generated by the wear of the two alloys. So there is an increased release of prostaglandin E2 in response to contact to Ti-6Al-4V particles, and an increase in the release of other inflammatory cytokines compared with Ti-Al-Nb particles. These data suggest that Ti-6Al-4V stimulates phagocytic cells more than the Ti-Al-Nb and Ti easily. Exposure of bone marrow cells from Ti-6Al-4V particles induce a significant increase in the release of proinflammatory and osteolytic mediators that are responsible for the lost prostheses.

4. Conclusions

Research conducted and thorough documentary study allow drawing general conclusions regarding biocompatibility but also the limits of metals and alloys used in dentistry:

- Metallic biomaterials are the most popular class of materials for implants, prostheses and medical instruments, due to their very good mechanical properties and acceptable biocompatibility.
- The main aspects that must be considered when using metallic materials in dentistry applications include corrosion, release of heavy metal ions, attrition and lack of elasticity. From this point of view we can speak clearly about the proven tissue toxicity of stainless steel in contact with human tissue. The problems raised by these steels in use as biocompatible materials are associated with the release of nickel ions, in particular as a result of the corrosion of corrosion products release causes inflammatory reactions, which prevents the endosseous implants osseointegration and favors the formation of fibrous capsule.
- Modern Co-Cr alloys due to superior mechanical properties and cost price advantages have replaced the noble class IV alloys in conventional technology (metal-polymer) and modern (metal and metal-ceramic composite) alloy cobalt - chromium -

molybdenum were used as subperiosteal implants, plates and implants endosseous transosseous, the advantage of mechanical biocompatibility better than stainless steel (316L), biocompatibility comparable to their chemical and, particularly, the lack of toxicity.

- Some common applications for metals, titanium has the best biocompatibility, surface explained by the formation of a stable oxide thin film, which confers passivity, it is preferred that the implant material due of density low mechanical properties and very good chemical;
- Titanium alloys are better tolerated than pure titanium because the oxide layer that forms is much larger (10-20μm) has been shown as corrosion resistance, biological compatibility, features and price resistance, the most used in medicine are alloys "conversion" on the basis of titanium. Their corrosion resistance can be increased by alloying with molybdenum, zirconium, rhenium, niobium, chromium, manganese, titanium alloy Ti-6Al-4V commonly used in implants shows a combination of the most favorable characteristics, but the problem of metal ion release.

Aluminum and vanadium are released into the tissue elements, metal ions released from corrosion and wear can induce hearing loss after a long period of implantation, especially due to the adverse effects of vanadium.

References

[1]. Anderson JM, et al. - *Host reactions to biomaterials and their evaluation*, Ratner BD, et al., eds. Biomaterials Science: An Introduction to Materials in Medicine. London: Elsevier, 2004

[2]. ASM Handbook Committee - *Metals Handbook-Corrosion of Metallic Implants and Prosthetic Devices*, vol. 13, ninth ed., American Society for Metals, Metals Park, 1987

[3]. Christoph Leyens, Manfred Peters - *Titanium and Titanium Alloys-Fundamentals and Applications,* Ed. WILEY-VCH, pg. 4-16, 2004

[4]. Gotman I. - *Characteristics of metals used in implants*, J Endourol (1997), 11(6):383-9

[5]. Claudia Fleck - Dietmar Eifler - *Corrosion, fatigue and corrosion fatigue behaviour of metal implant materials, especially titanium alloys,* International Journal of Fatigue 32 (2010) 929–935

[6]. M. Karthega, V. Raman, N. Rajendran - *Influence of potential on the electrochemical behaviour of b titanium alloys in Hank's solution*, Acta Biomaterialia 3 (2007) Elsevier, p. 1019–1023

[7]. H.J. Rack, J.I. Qazi - *Titanium alloys for biomedical applications*, Materials Science and Engineering C 26 (2006) Elsevier, p. 1269 – 1277

[8] Ghiban, B. - *Metallic Biomaterials* - Ed. Printech Bucuresti (1999)

[9].*** - Orthodontic Mini implants, Leone Clinical procedure for positioning.

THE ANNALS OF "DUNAREA DE JOS" UNIVERSITY OF GALATI.
FASCICLE IX. METALLURGY AND MATERIALS SCIENCE
N^0. 2 – 2013, ISSN 1453 – 083X

PROFILOMETRIC ANALYSIS OF WORN SURFACE OF BRONZE, IRON AND IRON COMPOSITE SAMPLES, BY PIN-ON-DISK METHOD

Virgil ILIUŢĂ, Luminiţa CIUPAGEA (COTEŢ), Gabriel ANDREI, Minodora RÎPĂ
"Dunărea de Jos" University of Galaţi, Department of Machine Elements & Graphics
email: virgil.iliuta@ugal.ro

ABSTRACT

In this study are presented the results of profilometric analysis for the wear of bronze materials, cast iron and composite materials. These materials were tested under dry wear conditions, using "pin-on-disk" method on a UMT-2 tribotester at a room temperature and relative humidity of 30-45%. The tests were carried out with load of 30, 40 and 60N at a linear speed of 0.815 m/s. The resulted traces of wear were examined with a Surtonic 3 + profilometer that has Talyprof software installed on, trademarks of TAYLOR HOBSON (United Kingdom) company. The obtained results allowed for a tribological analysis of the materials and their classification from the tribological point of view.

KEYWORDS: roughness parameters, bronze, gray cast iron, composite material for iron

1. Introduction

Polymer composites are more and more often used because of remarkable mechanical properties such as stiffness, low density, mechanical strength and good resistance to wear, excellent chemical properties and good wettability. Adding filling materials to the composite ones improves other characteristics such as electricity, etc. Due to their highly performant properties regarding quality, safety and ease of use, composite materials are also used in maintenance and repair sectors of the automotive, automobile, shipbuilding, steel industry, etc. [1, 2, 3, 9].

For these reasons, their use is required in aviation or automotive industry, as alternatives to conventional materials metal alloy composites. The possibility of designing the properties of composite materials is an advantage over traditional materials.

The addition of metal reinforcers in polymer composites led to the improvement of resistance and friction mechanical properties.

There are numerous applications where friction phenomenon is very important.

2. Experimental procedure

2.1. Materials and characterization

The material samples were subjected to tribological investigations are metals (bronze CuAl19Fe3T STAS 198/2-1992 brand and gray cast iron with nodular graphite EN-GJS- 450-10 SR EN 1563:1999 brand) and a composite meant for cast iron applications. This composite [10] is produced by "Diamond Metallplastic GmbH" company in München, Germany and is marketed under the name of Multimetall Eisen. In this paper it will be marked SCC code.

Table 1. *Mechanical characteristics of metallic materials*

Material quality/Prescripions	Sample code	Rm [N/mm^2]	$R_{p0,2}$ [N/mm^2]	A_5 [%]	Hardness HB
Bronze with Al, CuAl9Fe3T brand	SA	506	-	12.0	134
Gray cast iron with graphite, EN-GJS-450-10 brand	SC	506	433	11.6	173
Steel C45	SS	687	405	22	250

The materials listed above formed the tribological couple with pin which is made from C45 SR EN 10083-2:2007 steel.

The experimenatally obtained mechanical characteristics of the mechanical materials are listed in Tab. 1.

Composite material for iron (sample code: SCC) has the following characteristics [10]: elasticity modulus 6,000N/mm^2; traction resistance 77N/mm^2, crushing strength 5.0N/mm$^{2;}$ shear strength 22.5N/mm^2, bending strength 89N/mm^2 compressive strength 160N/mm^2;

Diffractometric analysis revealed the presence of the following phases in the composite material for iron's structure: α quartz SiO_2 particles of Al and Fe_5Si_3.

Test samples are: φ6.25x25 mm steel pin C45 and φ96x6 mm bronze disc iron cast and composite material for iron. Roughness of the samples was R_a0.8.

2.2. Experimental setup and procedures

Dry testing for sliding friction using "pin on disk" method was performed on UMT-2 tribotester (CETR®, USA) at room temperature and humidity between 30-45%.

Before testing, the samples were degreased with an organic solvent and dried with hot air at the temperature of 50°C.

The actual wear tests were preceded by a 10 minute dry at the speed of 0.815m/s. Wear tests were performed on the same wear track that resulted from the grind. The testing lasted for 50minutes, at a sliding speed of 0.815m/s, on a friction distance L_f = 2445 m and load forces of: 30, 40 and 60N.

The data regarding the digital profiles was acquired with the digital Surtronic3+ Profileograph, widely used in surface geometry tribological study and they were processed in Talyprof (Taylor Hobson® equipment and software). For the present study some of the program's expert functions were used.

The wear trace profilometric analysis is often used for setting the intensity and type of the wear process [4, 5, 6, 7, 8].

Wear evaluation through profiling methods was performed by using three characteristic parameters provided by the Talyprof software: maximum depth of track profile, the area of wear track between the highest peaks that limit the track result, on the left and the right side, and the profile's bottom (area of the hole) and the average depth of the track's profile (mean depth).

Based on digital roughness profile, a complex analysis of the worn surfaces' microgeometry was carried out, especially for wear tracks:

a) the comparative study of profile charts, following the variation of quantitative parameters, that characterize the wear track: the maximum profile dept, area, average profile;

b) using bar type diagrams for the variation of the three characteristic parameters;

Talyprof program uses the transformed profile by determining the average line of the profile (STAS 5730/1-85) and therefore digital profiles of wear tracks are distorted to the real profile. Determination of the average line of the profile involves minimizing the sum of squares of profile deviations. To the wear track, due to the rectangular geometry of the track, which is generated by sliding friction contact between the pin and disc, the calculation algorithm produces "compensation" of the side edges (limits) of the track area all with a sum of many small positive areas of the profile's surface roughness, from the left and the right side of the track. Therefore the profile is strongly "lifted" up at all corners.

In order to achieve the digital profiles for the wear traces, for each of the last three parts of the disc, were performed at least three profilograms.

These profilograms have been achieved by taking into consideration the radial direction (vertical on the circular trace) at angles of 120˚C.

Since the maximum width of the wear trace is connected to the diameter of the pin, 6mm, all the profiles have been carried out on an inspection length of the probe of 8mm.

3. Results and discussion

In Fig. 1÷9 are presented the results obtained for some of the studied materials: bronze, cast iron and composite material for iron, all of these materials making tribological joints with C45 steel pin.

In the case of bronze material (Fig. 1÷3), on the 8mm inspection length, the profilograms showed the deepest wear traces in case of a force F_2 = 40N (Fig. 2). The corresponding profilograms for F_3=60N force showed wear traces with smaller depths in comparison with F_2 force. From the profiles' combined analysis of and photos taken with a microscopic of these wear traces, associated with the comments concerning pin wear surfaces, the cause of these little deep traces could be established: at the normal loading force F_3, adhesion wear was very strong, unlike the case of wear tests for F_1 and F_2, where predominant was the abrasive wear.

The detachments from the bronze particles were a phenomenon of low intensity.

Basically, on one hand, the disk material, adhered to the pin (visible phenomenon due to the material's yellow color on pin surface), and on the other hand it has been redistributed on the wear surface of the disk.

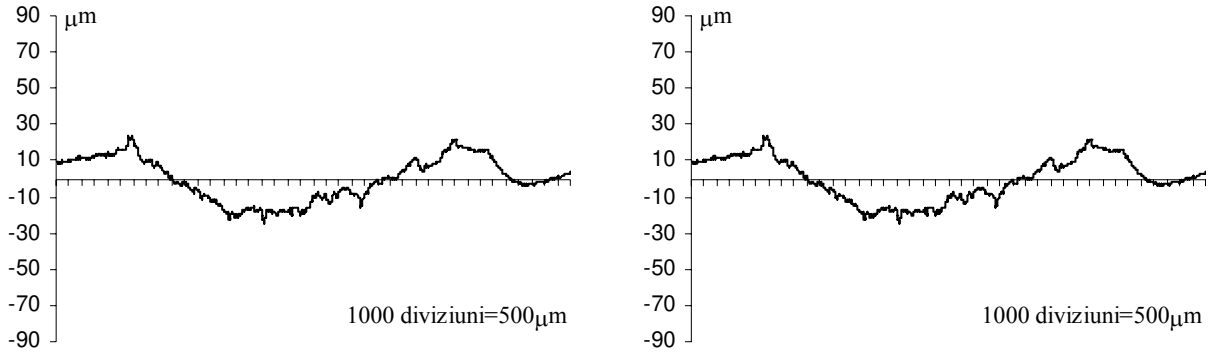

Fig. 1. *Bronze disk and steel pin, F_1=30N;*
a) wear trace profilogram conducted on a length of 8mm;
b) extracted from the wear trace's profilogram

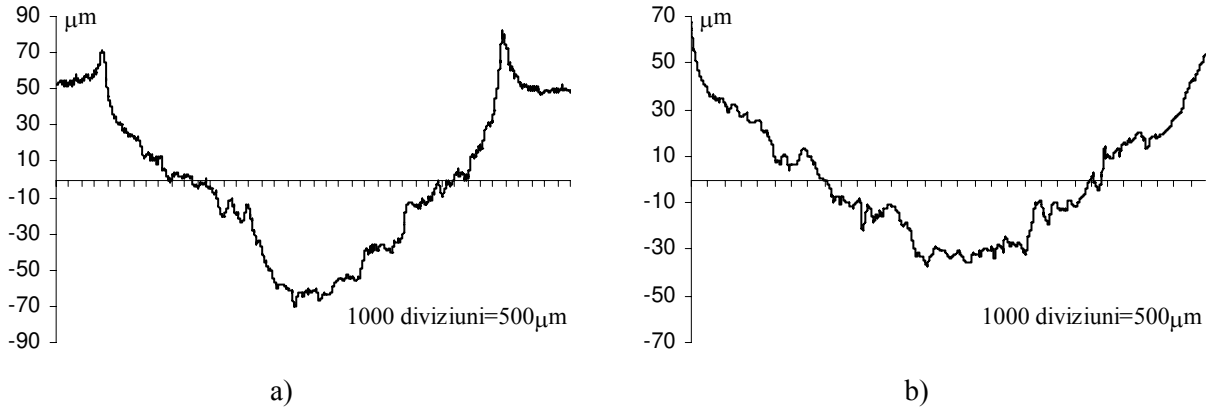

Fig. 2. *Bronze disk and steel pin, F_2=40N;*
a) wear trace profilogram conducted on a length of 8mm;
b) extracted from the wear trace's profilogram

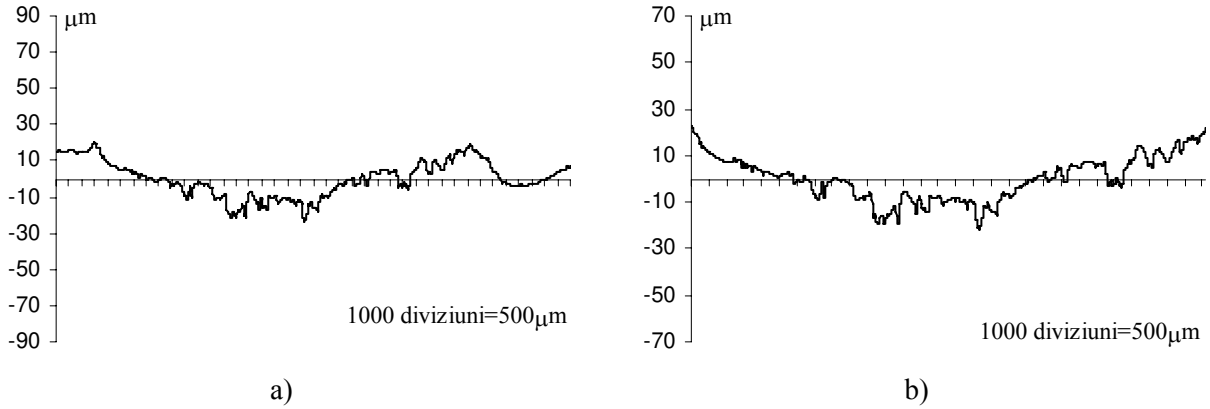

Fig. 3. *Bronze disk and steel pin, F_3=60N;*
a) wear trace profilogram conducted on a length of 8mm;
b) extracted from the wear trace's profilogram

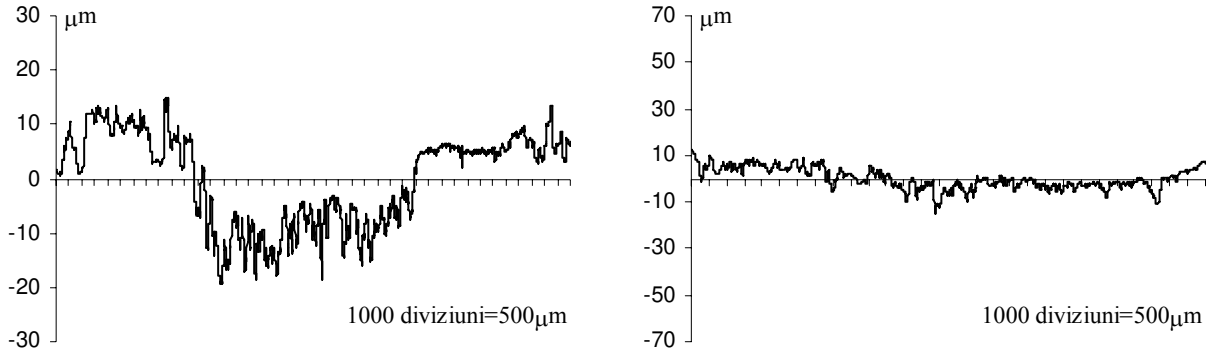

a) b)

Fig. 4. *Cast iron disk and steel pin, F_1=30N;*
a) wear trace profilogram conducted on a length of 8mm;
b) extracted from the wear trace's profilogram

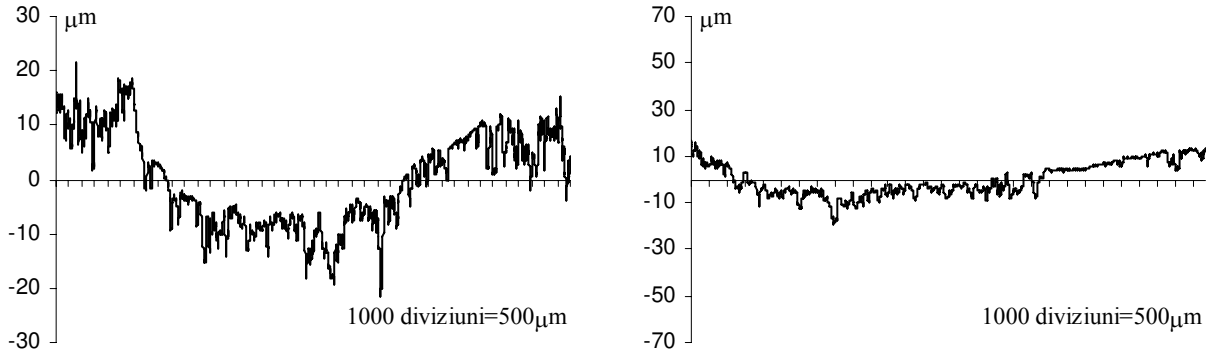

a) b)

Fig. 5. *Cast iron disk and steel pin, F_2=40N;*
a) wear trace profilogram conducted on a length of 8mm;
b) extracted from the wear trace's profilogram

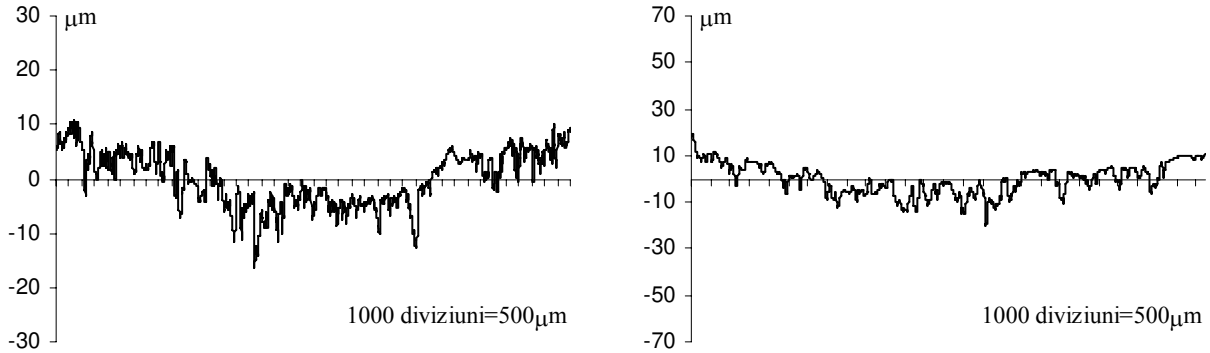

a) b)

Fig. 6. *Cast iron disk and steel pin, F_3=60N;*
a) wear trace profilogram conducted on a length of 8mm;
b) extracted from the wear trace's profilogram

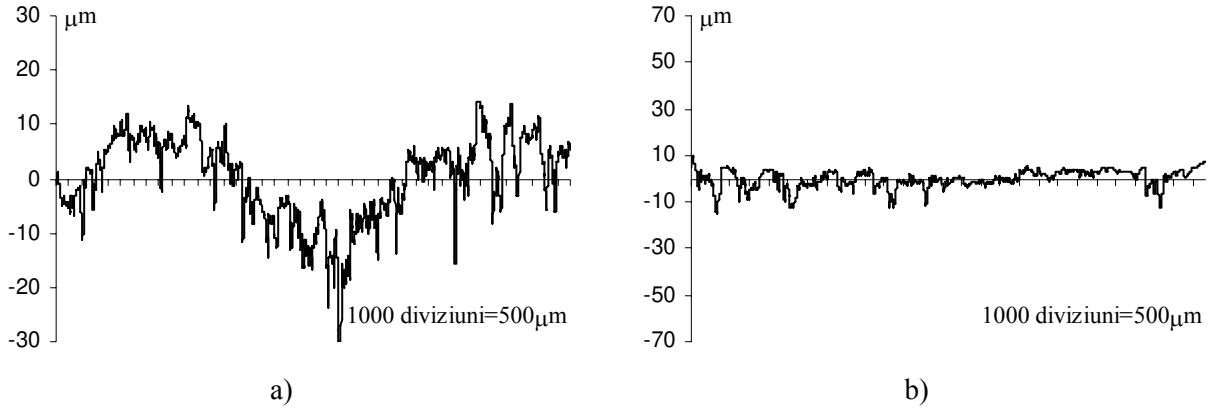

a) b)

Fig. 7. *Composite material for iron disk and steel pin, F_1=30N;*
a) wear trace profilogram conducted on a length of 8mm;
b) extracted from the wear trace's profilogram

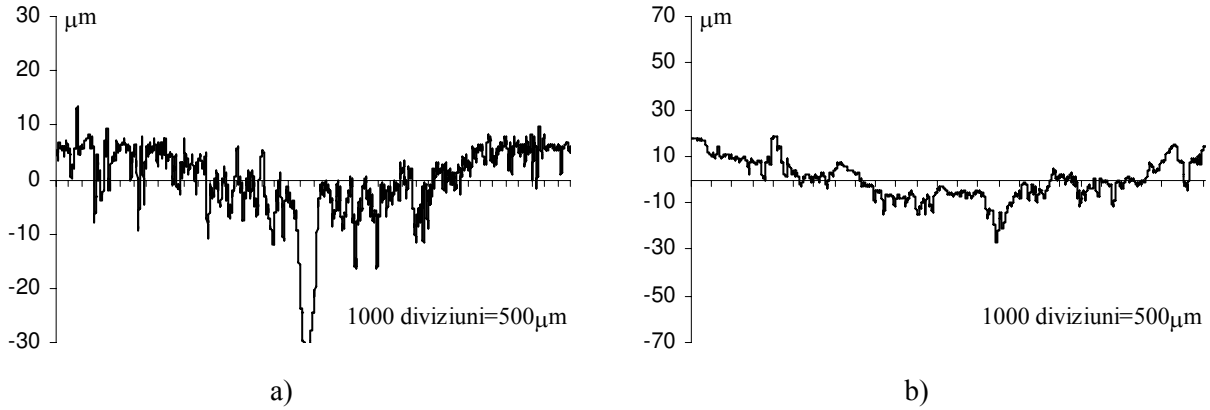

a) b)

Fig. 8. *Composite material for iron disk and steel pin, F_2=40N;*
a) wear trace profilogram conducted on a length of 8mm;
b) extracted from the wear trace's profilogram

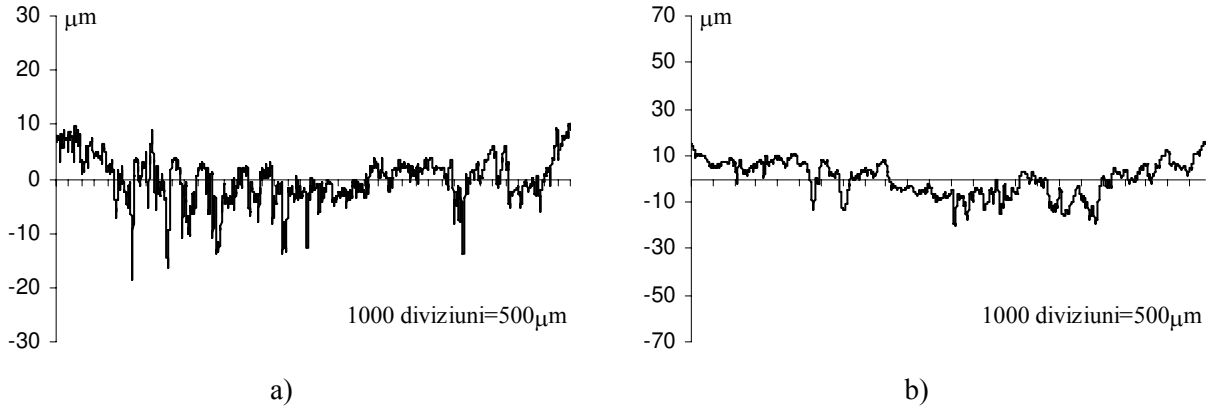

a) b)

Fig. 9. *Composite material for iron disk and steel pin, F_3=60N;*
a) wear trace profilogram conducted on a length of 8mm;
b) extracted from the wear trace's profilogram

In case of worn disk surfaces made of the cast iron (Figure 4÷5) and, respectively, from iron composite (Figure 7÷9), wear adhesion was less pronounced than in the case of bronze disk, idea sustained by the profilograme appearance with many more peaks and dips, quite high, namely deep (from 4-5μm to 10-15μm).

For F_3 = 60N test for iron (Figure 6), we can observe a few high peaks and very deep goals, on the worn surface which means strong smoothing of the profile's projections roughness profile of wear. Predictably, wear depth and width increase along with force. Composite material for iron behaves better at wear than iron, fact proven by the width and depth of wear, both smaller for composite F_0, comparing to cast iron. For tests with F_1 = 30N and F_2 = 40N, the less smoother appearance of the wear trace's profile is explained by a greater predominance of abrasive wear comparing to adhesive wear. Considering force F_3 = 60N, profiles are smoother which means an increase in the prevalence of adhesion wear. With the aid of the column diagrams (fig. 10÷11) the three parameters belonging to the wear profile were compared, and they were generated by Talyprof software: the maximum depth of the trace profile; the area of the wear trace, between the highest peaks that limit the trace, on the left and right side, and the bottom of the profile and the mean for the trace's profile.

The three parameters were analyzed for each material depending on the normal load force and for each loading force depending on the material.

By looking at the diagrams in Fig. 10÷12 one can confirm the predominance of adhesion wear for bronze material, as well as the greater percentage of adhesive wear to abrasive wear in case of the composite material for cast iron.

Studying Figure 10 it is revealed that, in the case of composite material for cast iron, the wasted volume is lower than the one for cast iron, but the probability that the percentage of adhesion wear would grow at bigger forces, is higher.

Comparing the behavior of materials at the same loading force (fig. 11), the following conclusion can be drawn: for all the three loading forces the lowest ear trace areas were obtained for composite material for cast iron. Of the three parameters used for the study, the one that offers the most obvious results is the wear trace area.

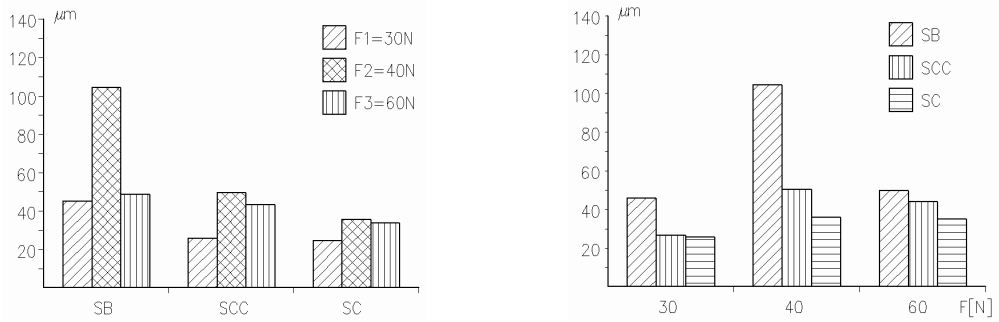

Fig. 10. *Maximum depth variation of the wear trace*

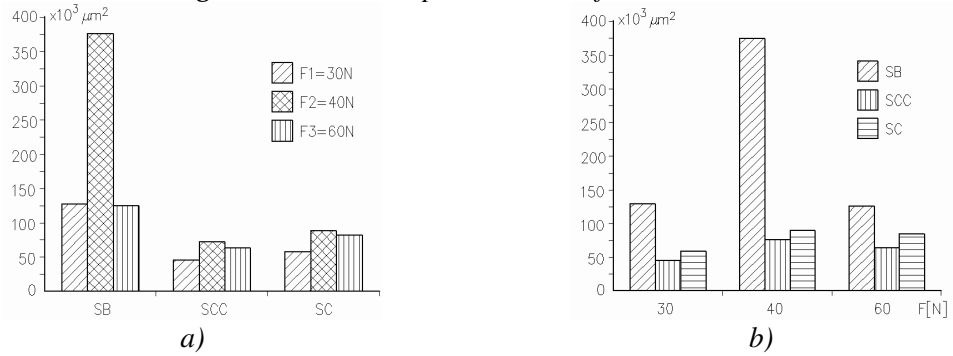

Fig. 11. *Area variation of the wear trace*

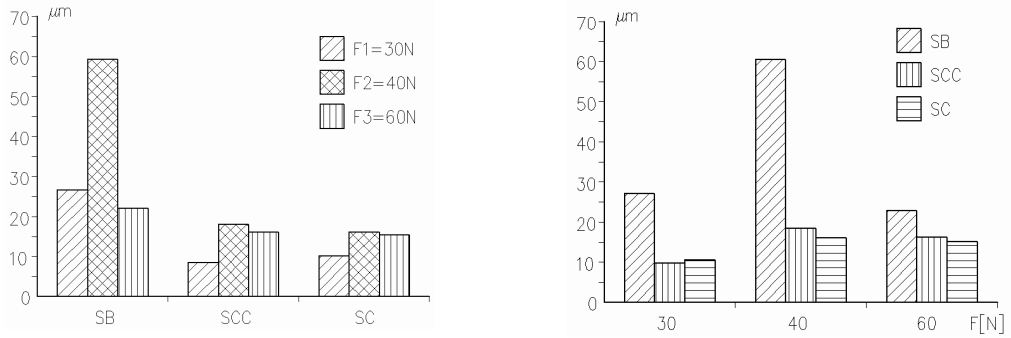

a) *b)*

Fig. 12. *Mean depth variation of the wear trace*

4. Conclusions

From the experimental results presented in the previous chapter, the following conclusions can be drawn:

For F_3=60N force, were obtained profilograms with smoother protuberances, which proves a predominance of adhesion wear

For all materials, the greatest trace wear appears at a F_2=40N force.

The area belonging to the smallest wear trace appears in the composite material for cast.

The composite material for cast iron, code F_o, presents the best profilometric characteristics of the wear trace after applying pin-on-disk method.

References

[1]. Brydson J.A., (ed.) - *Plastics Materials,* [book] Edition, Butterworth-Heinemann, ISBN 0-7506-4132-0, (1999)

[2]. Crawford R.J. - *Plastics engineering,* [book] 3rd ed. Stoneham, MA: Butterworth Heinemann; (1998)

[3]. Friedrich K. (ed.) - *Advances in Composites Tribology* [book], Elsevier Scientific Publishers, Amsterdam, (1993)

[4]. Kasem, H. et al. - *Characterization of surface grooves and scratches induced by friction of C/C composites at low and high temperatures,* Tribology International 43 (2010) pp.1951–1959

[5]. Lee J.H. et. al. - *Experimental and numerical analysis of friction and wear behavior of polycarbonate,* Wear 251 (2001) pp.1541–1556

[6]. Lee J.H. et. al. - *Modify the friction between steel ball and PDMS disk under water lubrication by surface texturing,* Meccanica (2011) 46: pp.499–507

[7]. Sedlacek M. et. al. - *Correlation between standard roughness parameters skewness and kurtosis and tribological behaviour of contact surfaces*, Tribology International 48 (2012) pp.102–112

[8]. Yousif B.F., El-Tayeb N.S.M. - *Wear and friction characteristics of CGRP composite under wet contact condition using two different test techniques*, Wear 265 (2008) pp.856–864

[9]. *** - 2002. CHM-17 (former Military Handbook–MIL-HDBK-17-3F)–Composite Materials Handbook, Volume 3 – Polymer Matrix Composites Materials Usage, Design, and Analysis, published by U. S. Department of Defense, ISBN: 978-1-59124-508-7

[10]. *** - Prospect firma „Diamant Metallplastic GmbH"

THE ANNALS OF "DUNAREA DE JOS" UNIVERSITY OF GALATI.
FASCICLE IX. METALLURGY AND MATERIALS SCIENCE
N^0. 2 – 2013, ISSN 1453 – 083X

EFFECTS OF THERMOPHYSICAL AND MECHANICAL PROPERTIES OF THE SUBSTRATE ON THE NORMAL ADHESION OF Ni-Cr-Fe COATINGS DEPOSITED BY THERMAL SPRAY

Daniel CALINICA
"Dunarea de Jos" University of Galati, Romania
email: daniel.calinica@yahoo.com

ABSTRACT

Thermal spray process is used to obtain high quality coatings that improve corrosion resistance, mechanical and tribological properties, in various technical applications: auto parts, turbine elements, in the naval industry. It aims at the increase service life of components, greater reliability and a higher degree of safety. A major contribution to achieving these goals is due to the good adhesion of the coating to the substrate. Generally, spray distance, design speed powders, powders nature, source temperature (flame, arc, plasma) are the most analyzed parameters in the thermal spray process. But, substrate roughness can strongly influence the performance of the coatings. The aim of this paper is to present the effect of substrate roughnes on the normal component of the adhesion of Ni-Cr-Fe coatings.

KEYWORDS: thermal spray, roughness, adhesion

1. Introduction

American Society for Testing and Materials (ASTM) defines adhesion as "the state in which two surfaces hold together because connection interfacial forces which may be of Van der Waals, interlocking forces, or a combination of these (ASTM D907-70)" [1].

Coating adherence to the substrate is considered as the most important property monitored in thermal spray deposition process.

A low level of adherence leads in time to delamination and corrosion at the interface coating/substrate, undesirable phenomena will progress continuously [2].

Literature states that the factors influencing adhesion layers deposited by thermal spray process are highly correlated with:

-the nature of the materials used for spraying, grain size, preparation method;

-spraying process mainly (oxy-fuel spraying, plasma spraying, arc spraying), and parameters (the distance the spray deposition temperature, the design speed of the particulates);

-thermophysical properties of the substrate (conductivity and thermal diffusivity) and the appearance of the surface (roughness and method used for cleaning and surface profiling) [3].

In Figure 1 is shown schematically how to achieve deposition using thermal spray process [4].

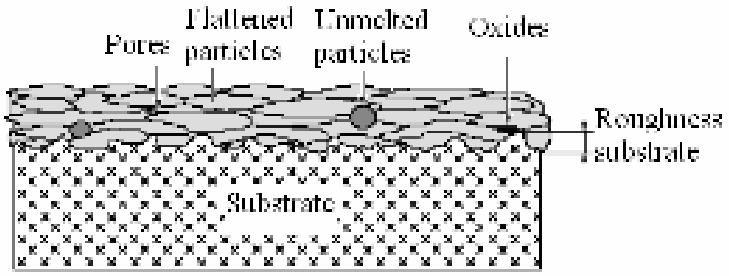

Fig. 1. *Principle of coating formation during thermal spraying*

Layer deposited on a rough substrate comprises the largest proportion of flattened particles and pores, but can include unmelted particles and oxides. The appearance of oxides and unmelted particles is due to the variation of the spraying parameters such as the melting temperature of the powder, the design speed or the spray distance.

Adhesion of the coating to the substrate is achieved through several mechanisms, but the mechanical interlock due to the rough surface of the substrate support is most important. A too high content of oxide inclusions and / or unmelted particles leads to decreasing the level of deposit adhesion to the substrate, in the literature stating that just melted and unoxidized particles can adhere to the rough surface of the substrate.

This paper aims at presenting the effect of substrate roughness on the normal adhesion strength of Ni-Cr-Fe coatings deposited by thermal spray.

2. Materials and experimental procedures

For testing tensile adhesion there is a wide variety of standardized methods: ASTM D 4541, ASTM C633, EN 582, ISO 14916 [5]. In this paper we used the non-standard method shown schematically in Figure 2a [6]. Samples of steel S355JR were made according to the dimensions shown in Figure 2b.

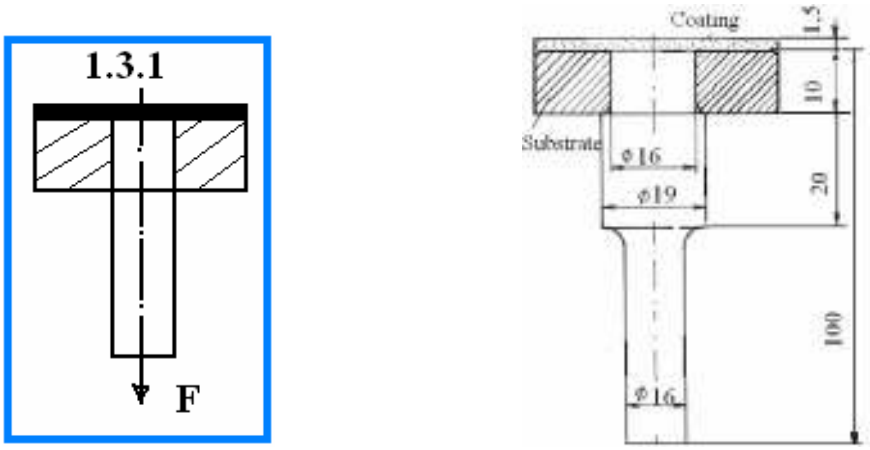

***Fig. 2. a-** Testing method**; b-** Sample dimensions*

The surfaces of the samples (Figure 3) were processed in order to make deposits as follows:

-Sample 1 was processed by turning coarse followed by sandblasting; surface roughness 12.5µm;

-Sample 2 was processed by turning normal followed by sandblasting; surface roughness 6.3µm;

-Sample 3 was processed by turning fine followed by sandblasting; surface roughness 3.2µm;

-Sample 4 was processed by polishing with diamond disc; surface roughness 1.6µm;

-Sample 5 was processed by grinding; surface roughness 0.8µm.

***Fig. 3.** Test samples with different roughness*

The coatings were deposited by employing an oxy-acetylene thermal spray system type Castodyn DS 8000 onto S355JR steel substrate samples. The spraying operation is carried out in two stages: first, a bond coat, followed by the anti-wear coating (figure 3a). The selected powders used in our research are the comercial powders

Ultrabond 51000 as bond layer and LubroTec 19985, a Ni-Cr-Fe alloy producing anti-wear deposits (figure 3b). The use of Ultrabond 51000 powder as a bond layer brings about an exothermic reaction so that a solid state metallurgical bonding is obtained, thus making it possible to deposit bonding layers on ferrous metals, coppers and on aluminium alloys.

a ***b***

Fig. 4. a *- Anti-wear coatings;* ***b*** *- The selected powders*

It also has good mechanical characteristics and very good resistance to elevated temperatures.

This first deposit should be approximately 0.1mm thick, obtained in a single pass. Next, the Ni-Cr-Fe alloy is deposited, by spraying a layer of LubroTec 19985 onto this bonding layer until it reaches the final dimension required (1.5mm - in our case).

During the coating, the temperature of the part does not exceed 200°C. The powders used had a particle size between ~38 and 150μm, according to the manufacturer's information.

3. Effect of thermophysical and mechanical properties of the substrate on the normal adhesion strength of Ni-Cr-Fe coatings deposited by thermal spray

To highlight the influence of substrate roughness on the normal component of adherence of coatings, we proceeded to spray tests using the five test samples with different roughness. To deposit layers, samples were successively mounted on a lathe. Spray parameters were adjusted in accordance with Table 1.

Table 1. *Spray parameters*

Parameter	Bond coat	anti-wear coating
Powder	51000	19985
Standard Spray Module	SSM 10	SSM 10
Setting of container mounting	3	4
Flame setting	Neutral	Neutral
Air without extension neck (bar)	0-1	0-1
Spraying distance (mm)	150	160
Pressure: Ox = 4 bar; Ac = 0.7 bar; Air = 2 bar Oxygen flow rate: ~2000 NL/h (flame) Acetylene flow rate: ~1800 NL/h Flame power: ~28 kW		

***Fig. 4**. Normal adhesion strength testing*

Testing normal component of adherence for the samples was done on a press Nilles model (Figure 4).

To calculate the normal adhesion strength of coatings of Ni-Cr-Fe deposited by thermal spray we used the following formula [7]:

$$A^{\perp} = (F^{\perp})/A \qquad (1)$$

where:

-$F^{\perp}$ is the maximum force applied perpendicular to the surface coating in order to coating detachment from the substrate,

-A is the surface of interface coating/substrate.

Test results of five samples are presented in Table 2.

***Table 2.** Normal adhesion strength of Ni-Cr-Fe coatings*

Test sample	Roughness	Normal adhesion strength
	[μm]	[Mpa]
1	12.5	10.5
2	6.4	12.2
3	3.2	9.1
4	1.6	7.3
5	0.8	4

Variation of normal adhesion strength depending on substrate roughness was approximated by a 2nd order polynomial expressions using Excel software [8]:

$$A^{\perp} = -0{,}6071x^2 + 5{,}6329x - 1{,}22 \qquad (2)$$

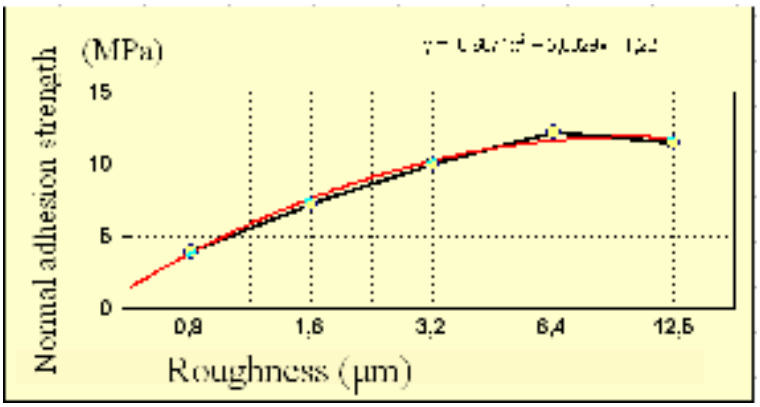

***Fig. 5.** Influencet of substrate roughness on the normal adhesion strength of Ni-Cr-Fe coatings*

To highlight the importance of thermophysical properties of the substrate was achieved a deposit on a sample prepared similarly to sample 5 but in the process of achieving thermal spray deposit has omitted the deposition of bond coat Ultrabond 51000. The result of failing to submit the bonding layer (which should be improved conductivity and thermal diffusivity of the substrate) consisted of almost

instantly deposited layer delamination. The traces of low thermal diffusivity can be easily observed in Figure 6 (right), showing clearly the existence of the temperature gradient. For comparison was achieved the detachment of coating deposited on sample 5 (Figure 6 left), in order to highlight the lack of distinct thermal zones, which leads to the conclusion that improving conductivity and thermal diffusivity of the substrate by applying bonding layers with excellent thermophysical properties is compulsory.

Fig. 6. *Coatings detached;* ***left*** *- with bonding layer deposition;* ***right*** *- without bonding layer deposition*

4. Conclusion

The results show that normal adhesion strength of Ni-Cr-Fe coatings strongly decreases if the substrate roughness decreases under 3.2μm, while increasing substrate less roughness reduces the coating adhesion. The maximum adherence value was recorded for substrate roughness of 6.3μm. This is probably due to increased exposed surface of the substrate.

Adhesion of coatings is strongly influenced by the thermophysical properties of the substrate and substrate processing quality. Application bonding layer Ultrabond 51000 has improved conductivity and thermal diffusivity of the substrate, and thus has increased adhesion of the coating deposited on the substrate. Good roughness coupled with the absence of oxides and other impurities is a compulsory condition for achieving adhesion.

Detachment of coatings from the substrate after tensile test was achieved uniformly, without damaging the coating or the substrate at the interface coating / substrate.

References

[1]. *** - *ASTM Standard D907-12a - Standard Terminology of Adhesives,* ASTM International, West Conshohocken, PA, (1998), www.astm.org

[2]. **McPherson, R**. - *The relationship Between the Mechanism of Formation, Microstructure and Properties of Plasma Sprayed Coatings,* Thin Solid Films, Vol. 83, (1981)

[3]. Shi, D. - *Biomaterials and Tissue Engineering*, (2004), pag. 49

[4]. Marot, G. - *Modellisation de l'essai d'indentation interfaciale et confrontation aux essais normalises pour la determination de l'adherence de revetements obtenus par projection thermique,* Universite des Sciences et Technologies de Lille, Lille, (2007), pag. 16

[5]. Era, H., Otsubo, F., Uchida, T., Fukuda, S., Kishitache, K. - *A Modified Shear Test for Adhesion Evaluation of Thermal Sprayed Coating,* Material Science and Engineering, (1998)

[6]. Kharlamov, Y.A. - *Methods of Measurement of the Adhesion Strength of Coatings",*Industrial Laboratory, (1987)

[7]. Mittal, KL. - *Adhesion Measurement of Films and Coatings,* Utrecht, (1995)

[8]. www.mrexcel.com.

THE ANNALS OF "DUNAREA DE JOS" UNIVERSITY OF GALATI.
FASCICLE IX. METALLURGY AND MATERIALS SCIENCE
N^0. 2 – 2013, ISSN 1453 – 083X

EFFECT OF ZrO_2 NANOPARTICLES ON THE MECHANICAL AND ANTICORROSION PROPERTIES OF EPOXY COATING

***Viorel PANAITE[1,2], Viorica MUSAT[1], Simona BOICIUC[1], Gina Genoveva ISTRATE[1] and Tamara RADU[1]**

[1]Centre of Nanostructures and Functional Materials, Faculty of Materials and Environment Engineering, "Dunărea de Jos" University of Galati, 47, Domneasca Street, RO-800008, Galati, Romania,
[2]Bureau Veritas Romania Controle International 165b, Galati, Brailei Street, RO-800310, Galati, Romania
[*]Corresponding author
email: panaite_viorel@yahoo.com

ABSTRACT

Homogeneous epoxy coatings containing ZrO_2 nanoparticles were applied on Grade A naval steel substrates. The morphology of the coating was characterized by optical microscopy and scanning electron microscopy. The effect of nanoparticles on the corrosion resistance of the hybrid coating was investigated by potentiodynamic polarization method. ZrO_2 (1wt. %) doping increased the microhardness of coating up to 15%, from 12.5 (kgf/mm^2) to 14.4 (kgf/mm^2). The coated steel samples were electrochemically monitorized over the 30 days of immersion in 5 wt. % NaCl solution. As shown by the polarization resistance and corrosion rate, the nanoparticles have a beneficial role, significantly improving the corrosion resistance.

KEYWORDS: nanoparticle, epoxy coating, Tafel curves, corrosion parameters

1. Introduction

Epoxy coatings have been widely used as a material to protect the metallic structures [1-3] and represent one of the most used coating systems in naval field. The protective coatings for marine steel structures work in very demanding conditions. Epoxy coating is suitable for these multiple requirements, because of its excellent chemical resistance, good electrical insulating properties and strong adhesion to steel substrates, but often is susceptible to damage by surface abrasion and wear [4, 5] and also is poorly resistant to the propagation of cracks [6].

Usually, epoxy coatings reduce the corrosion of a metallic substrate subject to an electrolyte. It is acting as a physical barrier layer against the ingress of a deleterious species and represent a reservoir for corrosion inhibitors. The barrier features of epoxy coatings can be enhanced by the incorporation of nanosized inorganic filler particles dispersed within the epoxy matrix, to form an epoxy nanocomposite.

Thereby, the following benefits can be obtained:

- Improving the integrity and durability of coatings by dispersion of fine particles in the cavities of epoxy matrix [7-9] which cause crack bridging [10];
- Preventing epoxy disaggregation during curing, resulting in a more homogeneous coating, due to tendency of nanoparticles to occupy small hole defects formed from local shrinkage during curing of the epoxy resin and act as a bridge, interconnecting more molecules;
- Offering significant barrier properties for corrosion protection, by reducing the total free volume and increasing cross-linking density [11, 12].

In this work it is discussed the influence of ZrO_2 nanoparticles on the surface morphology, microhardness and anticorrosion parameters of epoxy coatings. A better understanding of the mechanisms through which nanoparticles interact with epoxy matrix is very important to offer subsequent guidelines in design of epoxy coatings with high performances in corrosion protection of steel.

2. Experimental details

2.1. Materials

The epoxy resin, the hardener and the solvent used for coating deposition, commercially known as DER 353, I 3100 and D 309 respectively, were obtained from S.C. "Policolor" S.A. (Bucharest).

ZrO_2 nanoparticles with diameter below 100nm, were purchased from Sigma Aldrich (Steinheim, Germany). Sodium chloride (NaCl) used for corrosion test was purchased from S.C. Silal Trading S.R.L. (Bucharest). As substrate it was used rectangle steel samples (50x20mm) of grade S235JR+AR according to EN 10025-2004; the steel substrates have the following chemical composition: 0.12% C, 0.48% Mn, 0.015% Si, 0.013% P, 0.006% S, 0.039% Al, 0.016% Cu, 0.029% Cr, 0.024% Ni, 0.001% V, 0.003% Mo, 0.001% Ti, 0.001% Nb, Fe in rest. The composition and mechanical properties are similar to those of naval steel grade A.

2.2. Deposition of coatings

Steel substrates were initially cleaned with acetone, sand-blasted to the grade "Sa 2½" and cleaned by immersion in acetone. To remove the microparticles remained on the surface after sand-blasted, the substrates were sonicated for 10min. in acetone. Two types of coatings were prepared: epoxy and epoxy modified with ZrO_2 nanoparticles. The weight ratio of the epoxy resin to the hardener was 2:1. Before mixing, both resin and its hardener were diluted by solvent with a 1:1 weight ratio [13]. After that, the two solutions were stirred (1400rpm) using a Heidolph MR Hei-Tech magnetic stirrer, mixed and sonicated 10min. using a bath. For nanocomposite coating, at this resulted solution were added ZrO_2 nanoparticles, (1%) of the total weight of resin and hardener. The steel substrates were dipped into the obtained mixture, using a home-made dip-coater, at different withdrawn speed of 2.5, 5 and 10cm/min, respectively. After each layer deposited, the samples were kept at room temperature for 30min. and placed in an oven (Model FN 055 Nüve) at 90ºC for 30min. Finally, the samples were kept at room temperature for 30min.

The following groups of samples were obtained: epoxy coating (six layers) and ZrO_2 modified epoxy coatings (two layers noted with I and six layers noted with II) (Table 1). All the coated samples were kept at room temperatures for 14 days, to allow full curing for the subsequent mechanical and anticorrosion tests.

2.3. Characterization of coatings

The Thickness of the Dried Film (DFT) was measured by a nondestructive echo-sound test, using a 345 type Elcometer. The DFT values are presented in Table 1. The surface morphology and the cross-section for the nanocomposite sample covered by six layers at withdrawn speed of 10 cm/min, were analyzed by Scanning Electron Microscopy (SEM) (model Zeiss EVO MA 15). *Microhardness* measurements were realized for the samples covered by six layers, using a specific system (model PMT–3), according to EN ISO 6507/1 – 2002 [14] and equation (1),

$$HVF=1.8544*F/d^2\ [kgf/mm^2] \quad (1)$$

where F is strength test and d is diagonal of square trace remained after test.

The anticorrosive performance of nanocomposite coatings was investigated by potentiodynamic weak polarization method. The samples were kept immersed in corrosive solution (5wt.% aqueous NaCl solution) over the 30 days and the measurements of corrosion parameters were carried out periodically using Voltalab PGP 201 Radiometer Analytical equipment, with three electrodes: the epoxy coated steel sample served as the working electrode, while the counter electrode and the reference electrode used were a platinum grid and a saturated calomel - Ag/AgCl (Sat. KCl), respectively. A special cell ensures the reproducibility of the experimental parameters, especially the distances between electrodes and the free sample surface ($0.5024cm^2$) in contact with the corrosive solution. The steel was polarized around its corrosion potential, in general in the potential range of -1000mV÷ +200mV by a direct current (DC) signal, at a scan rate of 0.2mV/s. The results were processed with the application VoltaMaster software, version 4, using the following experimental parameters: diameter of the free surface of the sample (8mm); solution expose surface aria ($50.24mm^2$); steel sample density ($7.8kg/dm^3$) and iron valence (2).

3. Results and discussion

3.1. Effect of nanoparticles on the morphology of epoxy coating

Optical top-view images of the investigated samples are shown in Figure 1, which indicates that cured epoxy coatings have a relatively homogeneous morphology, the ZrO_2 modified epoxy coatings are denser and apparently showed no sign of nanoparticles agglomeration. The average thickness of the epoxy coatings for the sample studied, estimated from its cross-sectional view (as shown in Fig. 2a) is in accordance with the thickness of the coating measured by nondestructive echo-sound test. Six layers epoxy coating has the same range DFT with two layers ZrO_2 modified epoxy coatings (I). These coatings are much thinner than the six layers ZrO_2 modified epoxy coatings (II) (Table 1), which are very homogeneous in value. As it can be seen in Figure 2a, the surface of coating has small roughness, the coating shows a good compliance and adherence to the substrate, is very compact, without boundaries between the deposited layers.

The sample studied has some agglomeration of zirconia nanoparticles, revealed by cross section view

(see zone A of 24.38µm^2) (Fig. 2a) and chemical analysis (Fig. 2b).

3.2. Effect of nanoparticles on the mechanical properties – microhardness

As the indentation depth in microhardness measurements done on PMT–3 system is around 3µm and the coating thickness is above 25µm, the contribution of steel substrate to the final results of microhardness is negligible. In this work we presume that all the coatings have identical mechanical properties over the entire thickness and the results of microhardness so measured are the representative value of the whole coatings.

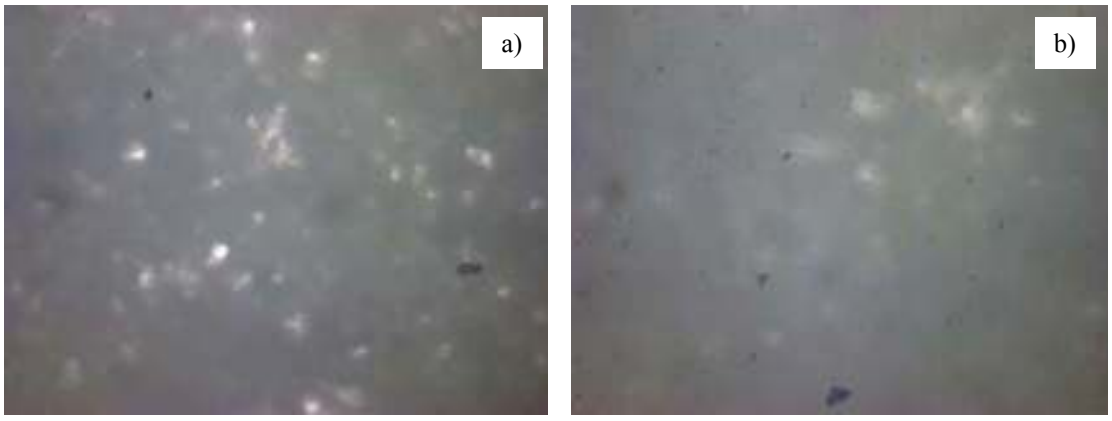

Fig. 1. *Optical micrographs of epoxy coatings obtained by six layers, at withdrawn speed of 10cm/min: a) plain epoxy; b) nanocomposite coatings*

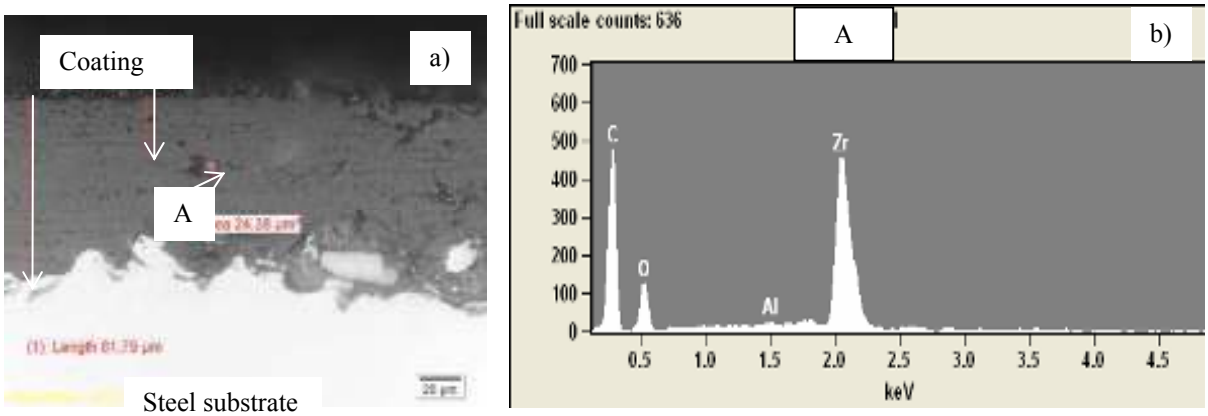

Fig. 2. *SEM images of nanocomposite coatings obtained by six layers, at withdrawn speed of 10cm/min: a) cross sectional view, indicating a thickness of 82µm; b) chemical analysis specific for region A*

Table 1. *DFT of the samples at different withdrawn speed*

Type of coating	**No. of layers**	**Withdrawn speed** (cm/min)	**DFT** (µm)
Epoxy	6	2.5	32±10
		5	50±10
		10	70±15
ZrO_2-Epoxy nanocomposite (type I)	2	2.5	35±5
		5	45±5
		10	50±8
ZrO_2-Epoxy nanocomposite (type II)	6	2.5	80±12
		5	95±10
		10	112±18

Figure 3 shows the values of microhardness calculated considering the average thickness of film coatings, for the samples covered by six layers, measured in two different stages: as prepared (a) and after salt spray test chamber (480 hours) (b). The incorporation into epoxy of small amount of ZrO_2 nanoparticles (1wt.%) have a beneficial role, improving the microhardness of coating, up to 15% for the homologous samples obtained for the withdrawn speed of 2.5cm/min and maintains the values of microhardness upper or sensitive to values equal in rest.

This beneficial role is particularly relevant in time, when the coating has worked in demanding conditions (after salt spray test chamber).

3.3. Effect of nanoparticles on the corrosion resistance of the coated steel

The corrosion potential, corrosion current, polarization resistance and instantaneous rate were estimated from the measured potentiodynamic polarization curves of epoxy-coated steel.

Fig. 4 shows the temporal evolution of instantaneous corrosion rate and polarization resistance (Rp) of steel samples coated at withdrawn speed of 2.5 cm/min, during the 30-day immersion in 5wt.% NaCl solution. To conclude on the beneficial role of introducing nanoparticles into epoxy matrix, it is better to compare the temporal evolution of the corrosion parameters for plain epoxy with nanocomposite type I, the two coatings having DFT closer as values.

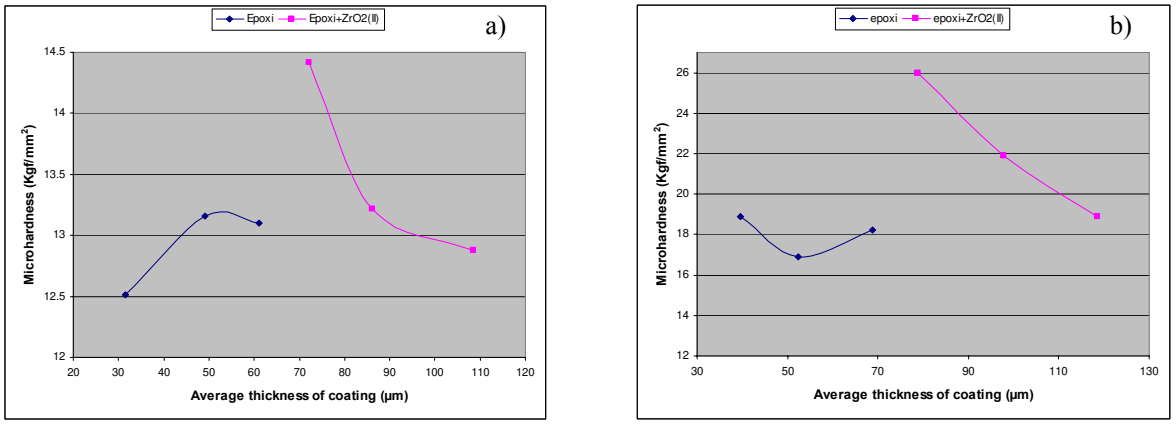

Fig. 3. *Microhardness values calculated considering the average thickness film, for plain epoxy and the ZrO_2 modified epoxy coating (II) (six layers): a) as prepared; b) after salt spray corrosion test*

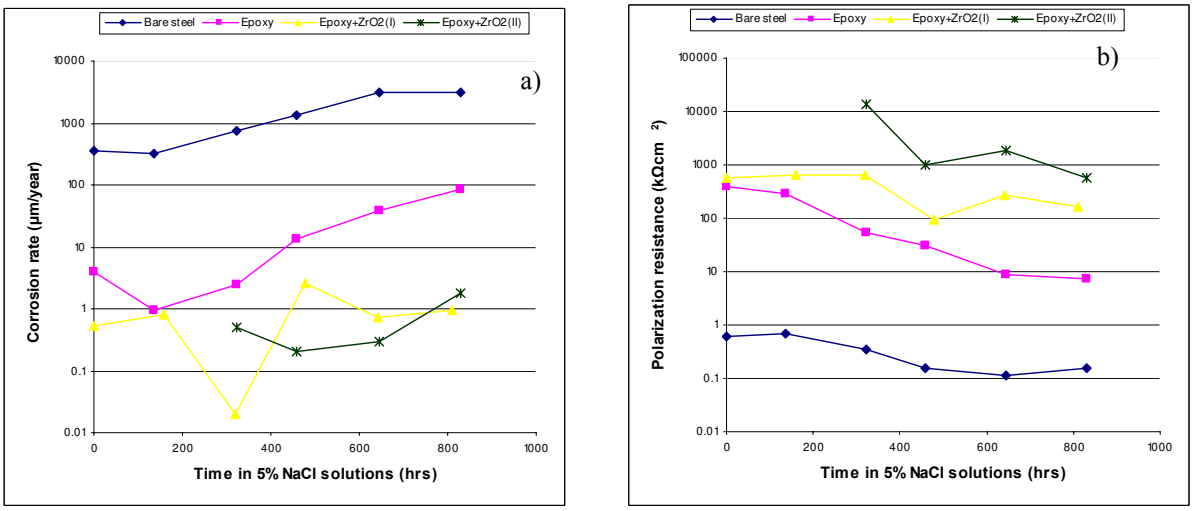

Fig. 4. *Temporal evolution of: corrosion rate - a); polarization resistance - b), for samples coated at withdrawn speed of 2.5cm/min, measured in 5wt% aqueous NaCl solution, at different times of immersion*

In case of nanocomposite type II, the beneficial role could be the result both of the presence of ZrO_2 nanoparticles and the thickness obtained after six layers deposited. So, the incorporation into epoxy coating of small amount of ZrO_2 nanoparticles (1wt.%) significantly reduced the corrosion rate of the epoxy-coated steel over the 30-day immersion in 5wt.% NaCl solution, up to 80 times after 800 hours (Fig. 4a), and consequently leads to the adequate improving corrosion resistance of the epoxy-coated, up to 20 times (Fig. 4b). It can be noted that Rp for nanocomposite type II in comparison with similar value for nanocomposite type I, is maintained higher by 3-27 times, while the corrosion rate at some moments of tests are better for nanocomposite type I. It is assumed that in the type I nanocomposite coatings, the nanoparticles were better dispersed, the two layers were thinner opposite to nanocomposite II,

in which some nanoparticles agglomeration were highlighted. For samples covered with six layers, each layer deposited leads to increasing the internal stress, the source for micro-cracks and pinholes [11, 12], decreasing mechanical strength and corrosion resistance.

Conclusions

ZrO_2 nanoparticles were successfully dispersed in epoxy based coatings at a concentration of 1%.

The electrochemical monitoring of coated steel over the 30 days of immersion in 5wt.% NaCl solution suggested the beneficial role of nanoparticles in significantly improving the corrosion resistance of the coated steel. The epoxy coating modified with ZrO_2 nanoparticles showed an important enhanced microhardness value.

The hardness remains at good values for samples subjected to corrosion test for long time.

For future research, it would be important to investigate ways to improve dispersion of the nanoparticles in the coating matrix, further effect of increasing ZrO_2 nanoparticles content on the anticorrosive performance for epoxy coating; the potential application of the nanoparticles as reservoirs of corrosion inhibitors, for the storage and for releasing them in some conditions will be investigated.

References

[1]. F. Galliano, D. Landolt - Prog. Org. Coat. 44 (2002) 217.
[2]. A. Talo, O. Forsen, S. Ylasaari - Syn. Met. 102 (1999) 1394.
[3]. V.B. Miskovic-Stankovic, M.R. Stanic, D.M. Drazic - Prog. Org. Coat. 36 (1999) 53.
[4]. B. Wetzel, F. Haupert, M.Q. Zhang - Compo.Sci. Technol. 63 (2003) 2055.
[5]. M.Q. Zhang, M.Z. Rong, S.L. Yu, B. Wetzel, K. Friedrich - Macromol. Mater. Eng. 287 (2002) 111.
[6]. S. Yamini, R.J. Young - Polymer 18 (1977) 1075.
[7]. K. Lam, K.T. Lau - Compo. Struc. 75 (2006) 553.
[8]. G. Shi, M.Q. Zhang, M.Z. Rong, B. Wetzel, K. Friedrich - Wear 254 (2003) 784.
[9]. Hartwig, M. Sebald, D. Putz, L. Aberle - Macromol. Symp. 221 (2005) 127.
[10]. F. Dietsche, Y. Thomann, R. Mulhaupt - J. Appl. Polym. Sci. 75 (2000) 396.
[11]. N. Huong - *Improvement of bearing strength of laminated composites by nanoclay and Z-pin reinforcement*, PhD. Dissertation, University of New South Wales, Australia (2006).
[12]. O. Becker, R. Varley, G. Simon - Polymer 43 (16) (2002) 4365.
[13]. Xianming Shi, Tuan Anh Nguyen, Zhiyong Suo, Yajun Liu - *Effect of nanoparticles on the anticorrosion and mechanical properties of epoxy coatings*, Recep Avci, acc. 30 jun. 2009.
[14]. *** - EN ISO 6507/1 – 2002

THE ANNALS OF "DUNAREA DE JOS" UNIVERSITY OF GALATI.
FASCICLE IX. METALLURGY AND MATERIALS SCIENCE
N^0. 2 – 2013, ISSN 1453 – 083X

PROPERTIES AND APPLICATIONS OF NANOCELLULOSE POLYMER COMPOSITES. A SHORT REVIEW

Magdalena Silvia RODEANU, Marian BASTIUREA, Gabriel ANDREI, Dumitru DIMA
"Dunărea de Jos" University of Galati, 47, Domneasca Street, RO-800008, Galati, Romania
email: magda.bastiurea@ugal.ro

ABSTRACT

This paper covers some aspects related to the structure of natural cellulose fibers as well the sources, obtaining methods, properties and their applications. In contrast with aramide and other materials resulted from fossil fuels, nanocellulose is completely renewable. The tensile strength of crystalline cellulose is similar to aluminum's. Its stiffness has been shown to be in the order of magnitude which is similar to aramide and better than glass fibers. Nananocellulose may be prepared as films which are expected to show high strength, high stiffness and high strain. Its strength/weight ratio is 8 times greater than that of stainless steel.

KEYWORDS: nanocellulose, polymer, nanocomposites

1. Introduction

Cellulose is the most widespread biopolymer on earth, having an annual production that is estimated to be over 7.5×10^{10} tons [3, 17]. Cellulose is the major component of most plant fibers, about 40% to 50% of the plant [19]. Nature creates amazing materials under modest conditions, i.e., neutral pH and ambient temperature and pressure [13]. In biosynthesis, approximately 36 individual cellulose molecule chains connect with each other through hydrogen bonding to form larger units known as elementary fibrils, which are packed into larger microfibrils with 5-50 nm in diameter and several micrometers in length [8], which in turn aggregate to form cellulose fibers. By applying effective methods these fibers can be disintegrated into cellulose substructures with micro- or nano-size dimensions [3]. Generally, cellulose is a linear natural macromolecular substance of carbohydrates class, consisting of D-anhydroglucose repeating units joined by β-1,4-glycosidic linkages (Figure 1), with molecular formula of $(C_6H_{10}O_5)_n$, where 'n' is the degree of polymerization ranging from 10,000 to 15,000) [3, 8, 9, 13], fiber with high strength, height stiffness, and low density, insoluble in water, forming the plant cells walls and giving the plant strength and elasticity. Cellulose fibers can be classified according to their origin and grouped as cellulose fibers extracted from wood fiber (hardwood, softwood); and from non-wood lignocellulosic fibre: leaves (abaca, cantala, curaua, palm, henequen, pineapple, sisal, banana), from seeds: cotton; from bast (flax, hemp, jute, ramie); from fruit (coir, kapok, oil palm); from grass: alpha, bagasse, bamboo; from stalk/straw (cereal: corn, wheat, rice), from tunicate and bacteria [7, 8, 11].

Plant fibers are constituted of cellulose fibers, consisting of helically wound cellulose microfibrils, bound together by an amorphous lignin/ hemicellulose matrix. Lignin keeps the water in fibers, acts as a protection against biological attack and as a stiffener to give stem its resistance against gravity forces and wind [7]. Hemicelluloses are believed by many researchers to act as interfacial coupling agents between the polar surface of cellulose and the relatively nonpolar lignin matrix. In principle, the plant cell wall composite is designed much like a synthetic fiber-reinforced polymer composite [11, 13].

The plant cell wall fiber is a heterogeneous membrane [1]. It is built up of two sections: the primary cell wall and the secondary cell wall, which is further divided into three layers (S1, S2 and S3) like in Figure 2 [7, 11, 13].

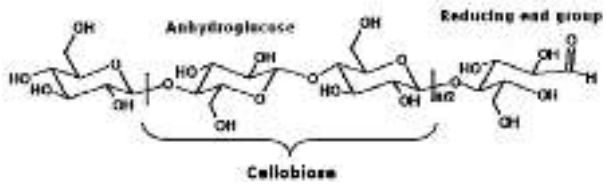

Fig. 1. *Chemical structure of cellulose [3]*

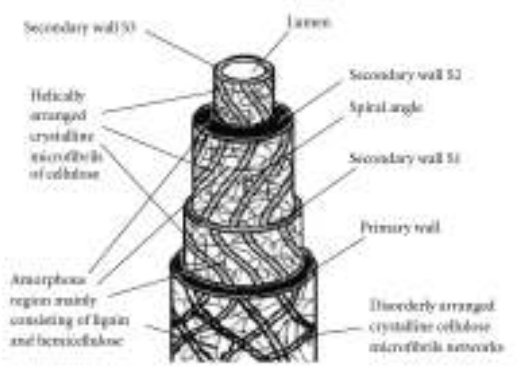

Fig. 2. *Structural constitution of a natural vegetable fiber cell, in which the secondary wall S2 makes up ~80% of the total thickness and thus acts as the main load bearing component [7, 11, 12]*

2. Synthesis of cellulose nanofibers

Cellulose nanofiber are not yet commercially available, instead micro-crystalline cellulose (MCC), a closely related item, is available, material widely used as a rheology control agent and as a binder in the pharmaceutical industry [9]. MCC is formed by particles of hydrolysed cellulose consisting of a very large amount of cellulose microcrystals together with amorphous areas.

MCC is prepared by removing part of the amorphous regions by acid degradation leaving the less accessible crystalline regions as fine crystals of typically 200–400nm in length and an aspect ratio of about 10. Degree of polymerization (DP) is about 140–400, depending on the cellulose source and treatment procedure [14].

There are several methods for cellulose nano-fibers isolation that have been reported till now. Cellulose nano-fibers have been synthesized from acetobacter xyllinium by enzymatic hydrolysis, from potato tuber cells through alkali hydrolysis and from sugar beets. Cellulose nano-fibers were prepared from MCC by application of a high pressure homogenizer (20,000 psi) and treatment consisting of different passes (0, 1, 2, 5, 10, 15 and 20).

Cellulose nanofibers have been extracted from the agricultural residues, wheat straw and soy hulls by chemomechanich technique.

The size of the obtained cellulose nano-fibers depends on several factors, a particular importance having the source of cellulose and the applied treatment [3, 7].

Each microfibril from the cellulose fiber is formed by aggregation of elementary fibrils, which are made up of crystalline and amorphous parts.

The crystalline parts, which can be isolated by several treatments, are the whiskers, also known as nanowhiskers, nanocrystals, cellulose nanocrystals, nanocrystaline cellulose (NCC), nanofibrils, cellulose crystallites, nanorods, rodlike cellulose microcrystals or microcrystals (in spite of their nanoscale dimension), with lengths ranging from 500nm up to 1–2μm, and about 8–20nm or less in diameter (Azizi Samir et al., 2004; Lima & Borsali, 2004), resulting in high aspect ratios. Each microfibril can be considered a string of whiskers, linked along it by amorphous domains (which act as structural defects) [1 - 18].

2.1. Mechanical methods

Mechanical methods such as high pressure homogenization, milling/ refining, cryocrushing, microfluidization were used to extract nanocellulose of wood fibers and plant fibers that have eliminated already hemicellulose and lignin matrix by pretreatment, from microcrystalline cellulose, invertebrate marine animals tunicates, algae and bacteria [5].

2.1.1. Crushing

This method has some drawbacks on the water retention capacity, which tends to increase during the process of refining and high energy requirement needed in the refining cellulosic materials and decreased cellulosic material crystallinity, and also to increase the solubility of the polymer [3].

2.1.2. Cryocrushing

A subclass of the previous method is the "cryocrushing", which involves water-swollen cellulosic material immersed in liquid nitrogen, followed by crushing the material with a mortar and pestle. This method has already been successfully used for craft fibers after refining.

Homogenization method has been applied by many researchers and involves cellulosic material passing through a small nozzle at very high pressure (20,000 psi). When frozen fibers are subjected to high impact forces, ice crystals exert pressure on the cell walls, breaking them and releasing the microfibrils [3].

2.2. Physical methods

2.2.1. Ultrasonication

Through this environmental friendly method, ultrasonication alone or combined with other methods eg. the acid hydrolysis, have been obtained nano-fibers only in laboratory tests.

Thus Filson and Daeson-Andoh obtained by ultrasonication and acid hydrolysis nano-fibers with an average diameter between 9- 23nm [18], see TEM image in Figure 3.

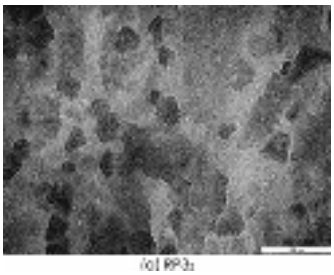

***Fig. 3**. TEM image of cellulose nanocrystals produced from ultrasonication of recycled pulp for 10 min and in water [18]*

2.2.2. Microwave

The main disadvantage of this method is that the material obtained is extremely deteriorated and the strength characteristics of the nano-fibers are small.

2.2.3. Gamma rays irradiation

Using the method there is a separation of a gas due to dehydrogenation, depolymeri-zation and destruction effects of the chains glucosides, affecting not only the molecular structure but also the secondary and supramolecular structure [3].

2.3. Chemical methods

2.3.1. Acid hydrolysis

Stable aqueous suspensions of cellulose nano fibers can be prepared by acid hydrolysis. This is main method used to obtain cellulose whiskers, using mineral acids like H_2SO_4, HCl and H_3PO_4, consisting basically in removing the amorphous regions present in the fibrils, leaving the crystalline regions that have a higher resistance to acid attack intact with a high degree of crystallinity [3, 14, 17].

2.3.2. Alkaline hydrolysis

Alkaline hydrolysis determines the partial separation of the cellulose fibers from the cell wall [3, 7] and an improvement of the physical and chemical characteristics of cellulose, particularly its reactivity to other chemical agents. These treatments are usually made using diluted solutions of NaOH (1-10%) at low or high temperatures and concentrated NaOH solutions over 10% only at low temperatures.

2.3.3. Organic solvent treatments

Aqueous and non-aqueous solvents are used for pulp. Usually, all these solvents suffer from either high environmental toxicity or poor solvating power [3, 6]. Another important aspect of this technology is the easy recovery of organic solvents by distillation and the absence of residues from these treatments [3].

2.3.4. Ionic liquid treatments

Dissolving of cellulose with ionic liquids allows for the full use of cellulose by combining two major principles of green chemistry: use of preferred solvent environment and bio-renewable feed-stocks [3, 5, 6].

2.3.5. Biological treatments

Under the enzymes action cellulosic material undergoes a degradation process. Destruction is influenced by the chemical characteristics of the cellulose wich has a high stability due to its high crystallinity. Degradation of the cellulose substrate occurs in the presence of microorganisms (fungi, bacteria) or directly with cellulose enzyme preparations. Enzymatic treatment removes non-cellulose components of the cellulosic fibers may increase the crystallinity, thermal stability and the amount of hydroxil groups of fibers treated [3].

3. Structural analysis

Once isolated, crystals are often suspended in a solution. Evaporating the solution on a substrate will produce a film of nanocrystals that can be imaged and characterized using a number of techniques: 1) Optical Microscopy (OM) which is limited to imaging objects greater than about half of the wavelength of visible light (> 250nm) and therefore can only image large crystal aggregates; 2) Scanning Electron Microscopy (SEM) (Fig. 4); 3) Atomic Force Microscopy (AFM) which involves rastering a cantilever with a very fine tip (tip radius ~ 20nm) across the sample and obtaining an image by measuring the cantilever deflection (see AFM image in Figure 6); 4) Transmission Electron Microscopy (TEM), in which electrons are accelerated to a high voltage and detected after they pass through the sample, (see TEM images in Fig. 5).

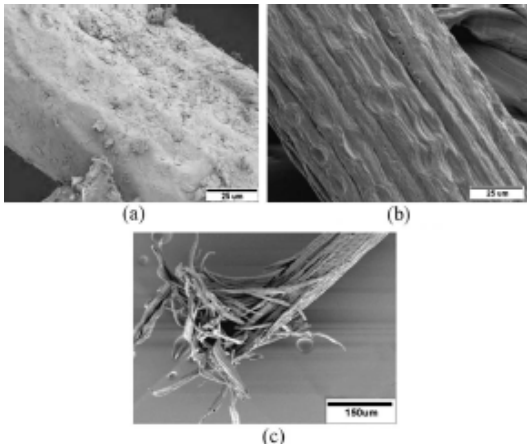

***Fig. 4.** SEM micrographs of (a) untreated coconut fiber; (b) coconut fiber subjected to pre-treatment and (c) coconut fiber subjected to bleaching [2]*

Both AFM and TEM can achieve nanometer resolution and are therefore effective for imaging

cellulose nanocrystals. Nuclear magnetic resonance and x-ray diffraction have also been used to further investigate crystal structure [15]. X-ray diffraction image can be seen in Figure 8. FTIR Spectra of NCC and of bamboo pulp following pretreatment with NaOH (Figure 7). As shown in this figure, the spectrum of NCC was similar to that of pretreated bamboo pulp with respect to the characteristic of cellulose peaks [15].

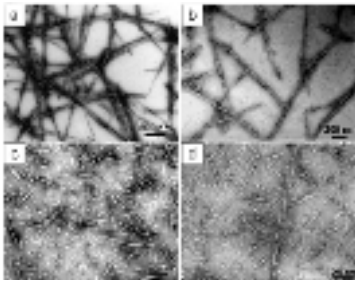

Fig. 5. *TEM images of dried dispersion of cellulose nanocrystals derived from (a) tunicate, (b) bacterial, (c) ramie, (d) sisal [17]*

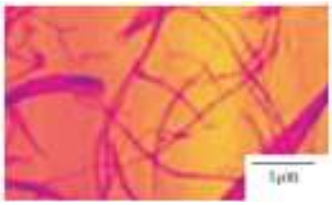

Fig. 6. *AFM image of wood cellulose nanofiber [7]*

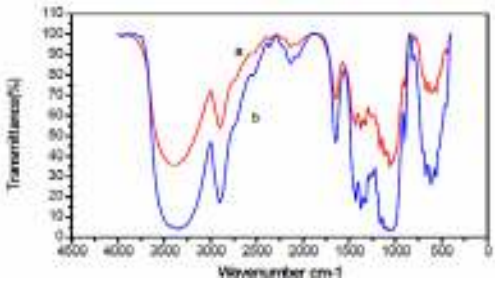

Fig. 7. *FTIR spectra of bamboo nanocristalline cellulose (a), and bamboo pulp with NaOH pretreatment (b) [15]*

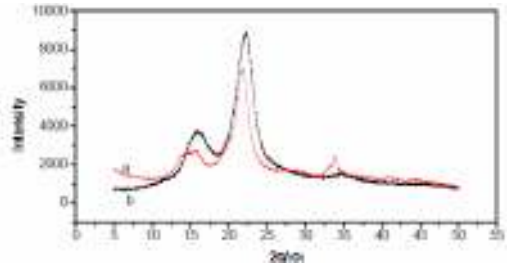

Fig. 8*. X-ray diffraction image of bamboo nanocrystalline cellulose (a) and cotton nanocrystaline cellulose (b) [15]*

4. Properties of nanocellulose

4.1. Mechanical properties

For wood nanocrystalline cellulose were determined different values of Young's modulus in the axial direction (EA = 50-100GPa) and transverse (ET = 18-50), tensile strenght σ_f = 0.3-1.4GPa, strain ε_f = 4-23% [4]. Other authors have determined that axial modulus values ranging between 110-220GPa, transverse modulus between 10-50 GPa and tensile strength between 7.5 -7.7GPa [5].

Tensile strength is greater than 200MPa, value similar to Kevlar fibers. Nanocellulose films have the same tensile strength value, strain 12% and the 20GP tensile stress [16].

4.2. Thermal properties

Thermal expansion coefficient in the axial direction was estimated at 0.1 ppm/K, value similar to quartz crystal [4].

The onset of thermal degradation occurs at 300^{0}C for freeze dried microcrystalline cellulose and 260^{0}C for nanocrystalline cellulose obtained by sulfuric acid hydrolysis of the same microcrystalline cellulose [4].

4.3. Electrical and magnetic properties

The cellulose is not electrically conductive, in native form. But it is influenced by the magnetic field when it is present, as loaded cellulose nanocrystals (CNC). CNC orientation using magnetic fields has been previously reported [16].

5. Applications

The cellulose nanofiber and composites reinforced with such fillers have found many potential applications in important areas such as electronics and electrical industry, construction, biomedicine, cosmetic, paper, packaging, building materials, textiles, solar cells, bioethanol, adsorption of heavy metal ions from aqueous solution, as filtration membranes and so on. Formulations with nanocellulose and silver nanoparticles can particularly be used as microbial medicaments, antibacterial agents in wound dressing, bandages, implants, skins replacements for burnings, face masks, artificial blood vessels, cuffs for nerve surgery, drug delivery, cell carriers and support matrices for enzyme immobilization, cosmetic tissues [4]. Surface modified cellulose nanofibers can be used for many applications such as coating, adhesives, sealings, filters, membranes, packing and cosmetics, aerospace industry, optically transparent flexible devices such as flat displays, digital cameras, cellular telephones and integrated circuits, paper or

board for printing and recording information liquid crystals for transparent windows, lamps or dials of clocks and watches [4, 6, 8]. For the bacterial cellulose important examples include supports for proteins, cell cultures and microorganisms, products for temporary skin and tissue replacement. NCC use of the fiber as reinforcement phase in the composite polymer matrix, have been incorporated into a wide range of polymer matrices, including polysiloxanes, polysulfonates, poly(caprolactone), styrene-butyl acrylate latex, poly(oxyethylene), poly(styrene*co*-butyl acrylate) (poly(S-*co*-BuA)), cellulose acetate butyrate, carboxymethyl cellulose, poly(vinyl alcohol), poly(vinyl acetate), poly(ethylene-vinyl acetate) (EVA), epoxides, polyethylene, polypropylene, poly-(vinyl chloride), poly-urethane, and water-borne polyurethane. Their incorporation into biopolymers, such as starch-based polymers, soy protein, chitosan, or regenerated cellulose, and biopolymer-like poly(lactic acid), poly(hydroxyoctanoate), and polyhydroxybutyrates have also been reported [10, 17].

6. Conclusions

This paper reviews the processes developed for the production of nanocellulose which include the methods for obtaining neat cellulose as well as the nanofibrillation procedure obtained by physical, chemical, enzymatic, mechanical or combined techniques. Aspects concerning physical description and material characterization were discussed. The paper underlines methods morphological investigation and structural characterization. Moreover, mechanical, thermal and electrical properties are reviewed.

References

[1]. Dufresne A. - *Natural Polymers*, Volume 2: Nanocomposites, chapter 1 Nanocellulose:Potential Feinforcement in Composites. Royal Society of Chemistry 1-32, (2012)

[2]. Rosa M.F. et al. - *Cellulose nanowhiskers from coconut husk fibers: Effect of preparation conditions on their thermal and morphological behavior*, Carbohydrate Polymers 81 (2010) 83–92

[3]. Frone A. et al. - *Some aspects concerning the isolation of cellulose micro- and nano-fibers***.** U.P.B. Sci. Bull., Series B, Vol. 73, Iss. 2, (2011)

[4]. Rebouillat S. et al. - *State of the Art Manufacturing and Engineering of Nanocellulose: A Review of Available Data and Industrial Applications*, Journal of Biomaterials and Nanobiotechnology, (2013), 4, 165-188

[5]. Moon R. et al. - *Cellulose nanomaterials review: structure, properties and nanocomposites,* Chem. Soc. Rev., (2011), **40**, 3941–3994

[6]. Liu H. et al. - *Understanding the Interactions of Cellulose with Ionic Liquids: A Molecular Dynamics Study,* The Journal of Phisical Chemistry B, (2010)

[7]. Kalia S. et al. - *Cellulose-Based Bio- and Nanocomposites: A Review***,** Hindawi Publishing Corporation International Journal of Polymer Science Volume 2011, Article ID 837875

[8]. Zhou C. et al. - *Recent Development in Applications of Cellulose Nanocrystals for Advanced Polymer-Based, Nanocrystals – Synthesis*, Characterization and Applications, (2012)

[9]. Chauhan V. et al. - *Use of nanotechnology for high performance cellulosic and papermaking products*, Cellulose chemistry and technology, (2011)

[10]. Masoodi R.et al., *Mechanical characterization of cellulose nanofiber and bio-based epoxy composite*, Materials and Design 36 (2012) 570–576

[11]. Kalia S. et al. - *Pretreatments of natural fibers and their application as reinforcing material in polymer composites-a review*, Polymer Engineering and Science, (2009), 49:1253–1272.

[12]. Rong M.Z et al. - *The effect of fiber treatment on the mechanical properties of unidirectional sisal-reinforced epoxy composite,* Composites Science and Technology, (2001), 61:1437–1447

[13]. Zhuo Li - *Bio-based Composites That Mimic the Plant Cell Wall*, Thesis Master of Science In Biological Systems Engineering, Virginia Polytechnic Institute and State University, (2009),

[14]. de Azeredo H. - *Nanocomposites for food packaging applications*, Food Research International 42 (2009) 1240–1253

[15]. Mengjiao Y. et al. - *Preparation and Characterisation of Bamboo nanocrystalline cellulos*, BioResources 7(2), 1802-1812, (2012)

[16]. Tummala G.K. - *A Brief Review on Electronic and Magnetic Applications of Nanocellulose.*

[17]. Habibi Y. et al. - *Cellulose Nanocrystals: Chemistry, Self-Assembly, and Applications*, American Chemical Society, (2009)

[18]. Filson P.B. et al. - *Sono-chemical preparation of cellulose nanocrystals from lignocellulose derived materials*, Bioresource Technology, vol 100, (2009), no.7, pp.2259-2264.

THE ANNALS OF "DUNAREA DE JOS" UNIVERSITY OF GALATI.
FASCICLE IX. METALLURGY AND MATERIALS SCIENCE
N^0. 2 – 2013, ISSN 1453 – 083X

PHOTOCATALYTIC PROPERTIES OF SEMICONDUCTIVE OXIDE NANOPARTICLES. FROM FUNDAMENTALS TO APPLICATIONS

Mariana (BUŞILĂ) IBĂNESCU[1], *Viorica MUŞAT[1], Torsten TEXTOR[2], Boris MAHLTIG[3]

[1]Centre of Nanostructures and Functional Materials-CNMF, "Dunărea de Jos" University of Galaţi, 111, Domnească Street, 800201, Galaţi, Romania
[2]DeutschesTextilforschungszentrum Nord-West GmbH, DTNW GmbH, Adlerstr. 1, 47798 Krefeld, Germany and CENIDE, Center for Nanointegration Duisburg-Essen
[3]University of Applied Sciences, Faculty of Textile and Clothing Technology, Webschulstr, 31, 41065 Mönchengladbach, Germany
*Corresponding author
email: viorica.musat@ugal.ro

ABSTRACT

Photocatalysis is a promising technology that demonstrated important applications in environmental systems such as air purification, pollution removal, self-cleaning and antimicrobial. Semiconductive oxides (e.g., ZnO, TiO_2, CuO) are important photocatalytic materials that can act as sensitizes for light based redox processes due to their electronic structure, which is characterized by the conduction-band with electrons (good reductants) and the valence band with holes (powerful oxidants). Excitation of electrons from the conduction-band and valence-band holes can react with electron donors and electron acceptors adsorbed on the semiconductor surface and electric double layer around the particles. The band gap value determines the semiconductive behavior of oxide nanoparticles. The absorption of UV-Vis radiation is an important tool for evaluating photocatalytic behavior of the obtained semiconductive nanoparticles. In this paper we present the correlation between the band gap value, particle size and the photocatalytic activity of ZnO nanoparticles prepared via an aqueous solution chemical method.

KEYWORDS: ZnO nanoparticles, band gap, photocatalysis, antimicrobial activities

1. Introduction

Semiconductor photocatalysts such as TiO_2 and ZnO nanoparticles have attracted much attention in recent years due to their various applications to the photocatalytic degradation of organic pollutants in water and air and dye sensitized photovoltaic solar cell [1-3].

Among these semiconductor photocatalysts, TiO_2 is the most commonly used owing to its stable, harmless and inexpensive properties. However, two typical defects including only exciting by high energy UV irradiation and a low quantum yield rate resulted from a low rate of electron transfer to oxygen and a high rate of recombination between excited electron/hole pairs, limit the photo-oxidation rate of TiO_2 nanoparticles. In order to improve the photocatalytic efficiency of TiO_2 nanoparticles, most studies have been focused on the modification of TiO_2 doped by metal ions, especially transition metal ions, which make it possible for TiO_2 to absorb visible light by increasing the charge separation [4, 5]. In addition, combination of different kinds of semiconductor also photocatalysts is a promising way to improve the photocatalytic efficiency [6]. The substitution of TiO_2 by ZnO used for photo-degradation is ascribed to the photo-degradation mechanism of ZnO being similar to that of TiO_2 [3, 13]. When photocatalyst e.g. semiconductor TiO2 or ZnO was irradiated with UV-light, electron (e-) from the valence band was excited to the conduction band resulting in the formation of holes (h+) in the valence band. Both excited state electrons (in conduction band-$_{CV}$) and holes (in valence band-$_{VB}$) can recombine, but if suitable scavenger for electrons or holes is available, recombination is prevented [14].

Example, in an air environment, the photogenerated holes and electrons can react with water molecule which are adsorbed on the surface or react with oxygen molecule to form hydroxyl and superoxide radicals.

ZnO nanoparticles can be synthesized by various approaches including sol–gel processing [15, 16], homogeneous precipitation [17], mechanical milling [18], organometallic synthesis [19], microwave method [20], spray pyrolysis [21, 22], thermal evaporation [23] and mechanochemical synthesis [24].

However, ZnO nanoparticles fabricated by the abovementioned methods are prone to aggregate due to the large surface area and high surface energy. In order to improve the dispersion, it is necessary to modify the surface of ZnO nanoparticles.

The present study focuses on the solvothermal synthesis of ZnO nanopowders and the effect of concentration of the precursors and the utilization of ZnO nanoparticles for photocatalytic process for textile treatment.

The solvothermal synthesis of ZnO powders has four advantages (1) powders with nanometer-size can be obtained by this method (2) the reaction is carried out under moderate conditions (3) powders with different morphologies by adjusting the reaction conditions and (4) the as-prepared powders have different properties from that of the bulk.

The influence of surface coating on the photocatalytic degradation of methylene blue was studied, since the photocatalytic activity of ZnO nanoparticles in form of both colloidal solution and textile coating material was evaluated in normal laboratory environment and after UV irradiation.

2. Experimental details

The preparation procedure was basically similar to that of Spanhel [25]. The procedure consists of two major steps. First the suspension of the precursor and second the hydrolysis of the precursor to form the zinc oxide nanoparticles. Zinc acetate dihydrate $(ZnAc)_2x2H_2O$ (Sigma Aldrich) and isopropanol (Sigma Aldrich), were used to prepare the precursor before lithium hydroxide (LiOH-Merk) was used to hydrolyze the precursor.

A two neck round bottom distillation flask was used to suspend 0.035M; 0.045M; 0.11M of $(ZnAc)_2x2H_2O$ in 500mL 2-propanol by reflux heating 82°C (boiling point) for three hours. 0.035M (1:2) lithium hydroxide was dissolved in 500 mL isopropanol at room temperature by vigorous magnetic stirring.

The $(ZnAc)_2x2H_2O$ suspension was cooled down to 0°C before the lithium hydroxide solution was added drop wise under vigorous stirring.

The ZnO sol was stored at ≤ 4ºC for 24 hours.

For separating ZnO nanoparticles and to remove the residual products, high-speed centrifugation 4000rpm/20min was used followed by several alcoholic washes. After which it is dried in an oven at 60°C to obtain powder can be weighed and finally resuspended in alcohol to be ready for application to the textile.

The finishing solutions were prepared: zinc oxide nanoparticle solution (100mL), 3-Glycidoxypropyl)methyldiethoxysilane (GPTMS) sol, Tetraethyl orthosilicate (TEOS) and 0.01N hydrochloric acid (HCl) were mixed together for 2h by magnetic stirring. The final formulation was applied to the fabrics (cotton 100%) by a pad-dry-cure method. After padding samples were dried in ventilated oven at 130°C for 30min. Finally the fabrics were washed with distilled water and dried at ambient temperature.

The size of the ZnO nanoparticles was measured by dynamic light scattering (DLS), using Zetasizer, Nano-S produced by Malvern. The crystal structures of the product were identified by X-ray diffraction patterns DRON -3 diffractometer system (Burevestnik, USSR) with CoKα radiation, λ=1.789 Å.

The crystallite size of the particles was calculated with Debye-Scherrer formula:

$$D = \frac{0.94 \cdot \lambda}{\beta \cos\theta} \quad (1)$$

The value of interplanar distance (d) was calculated with Bragg's equation:

$$2d \sin\theta = n \cdot \lambda \quad (2)$$

and lattice parameters:

$$\frac{1}{d^2} = \frac{4\left(h^2 + h \cdot k + k^2\right)}{3a^2} + \frac{l^2}{c^2} \quad (3)$$

The calculation is based on the measurement of full-width at half-maximum (FWHM) values in the corresponding XRD pattern.

Band gap energy value for ZnO nanoparticles was calculated with formula [26]:

$$E = h \cdot \frac{c}{\lambda} \quad (4)$$

UV/Vis Absorption measurements for that material are being carried out using a Cary 5E UV-VIS-NIR Spectrophotometer, Varian Deutschland GmbH with integrating sphere.

3. Results and discussions

Figure 1 shows DLS measurements of ZnO nanoparticle as prepared at different concentrations.

The results showed that the size of the nanoparticles increases (from 6nm to 322nm) with the increasing concentration of the solution (from

0.025M to 0.11 M). Crystal structure of the particles prepared was characterized by the XRD (Figure 2). The peaks at 2θ = 37.48°, 40.37°, 42.87° were assigned to (100), (002), (101), of ZnO planes, indicating the wurtzite structure. No characteristic peaks of any impurities were detected, suggesting that high-quality ZnO nanoparticles were synthesized.

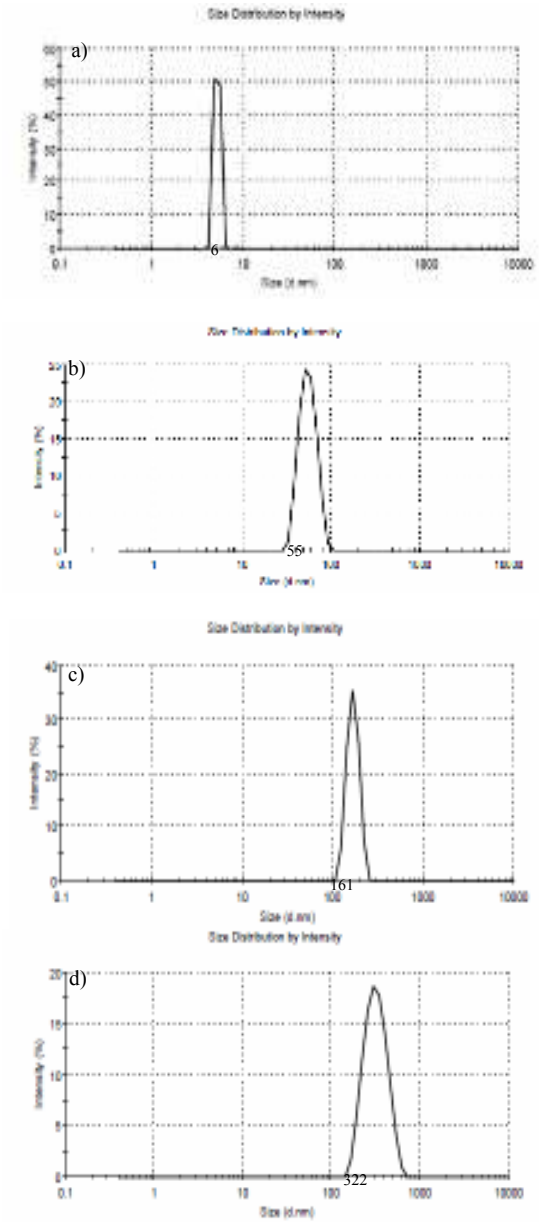

***Fig. 1**. Histograms of ZnO nanoparticles with different concentration by DLS: ZnO-1(0.025M) a), ZnO-2(0.035M) b), ZnO-3(0.045M) c) and ZnO-4(0.11M) d)*

Accordingly, the crystallite size calculated from XRD patterns using the Scherrer equation (Scherrer size) shows the same variation peak intensity.

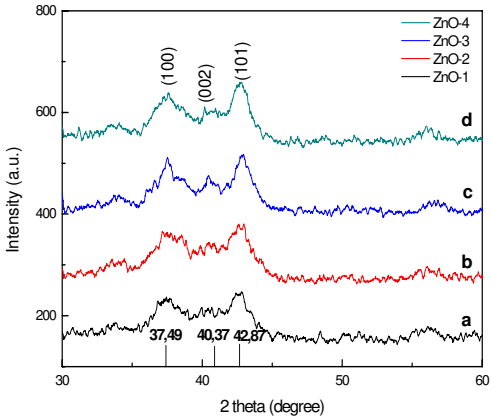

***Fig. 2.** XRD patterns for ZnO nanoparticles with different concentration: ZnO-1(0.024M) a), ZnO-2(0.035M) b), ZnO-3(0.045M) c) and ZnO-4(0.11M) d)*

***Table 1.** Crystallite size, interplanar spacing and lattice parameters for ZnO nanoparticles with different concentration*

Solution concentration	**Crystallite size**	**c**	**a**
[mol/L]	[nm]	[Å]	
0.025M	2.4	5.286	3.2823
0.035M	5.2		
0.045M	8.1		
0.11M	7.5		

For the study of the band gap was used optic absorption spectrum. When a semiconductor absorbs photons of energy larger than the gap of the semiconductor, an electron is transferred from the valence band to the conduction band, an abrupt increase in the absorbency of the material occurs to the wavelength corresponding to the band gap energy. The value of the band gap energy for the sample ZnO-0.035 M was 3.16eV, which resulted from absorption at 392nm. The photocatalytic properties of ZnO nanoparticles on degradation of methylen blue (MB) were studied using ZnO nanoparticles with different size. It can be seen that nanoparticles obtained from the solution with 0.035M concentrations are most effective (Figure 3).

From Figure 4, we can see the comparison with untreated fabrics and treated fabrics between ZnO nanoparticles. The extent of photocatalytic degradation was determined by the reduction in absorbance of the solution. As a result of the reaction between ZnO nanoparticles (through the reactive oxygen species on its surface) and MB dye, the rate

of decolourization was changed as the size of ZnO nanoparticles changed.

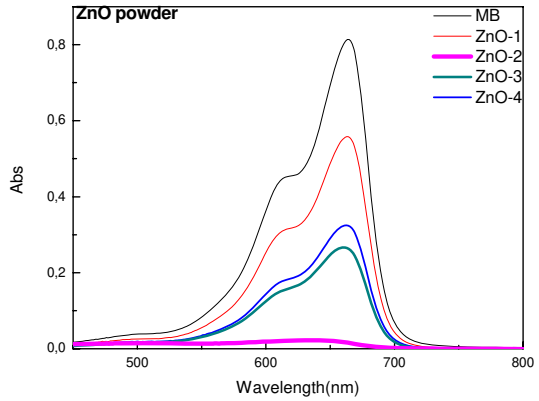

Fig. 3. *UV-Vis absorption spectra of methylen blue in presence by different size of ZnO nanoparticles (powder) after UV-irradiation, 1h in normal laboratory environment*

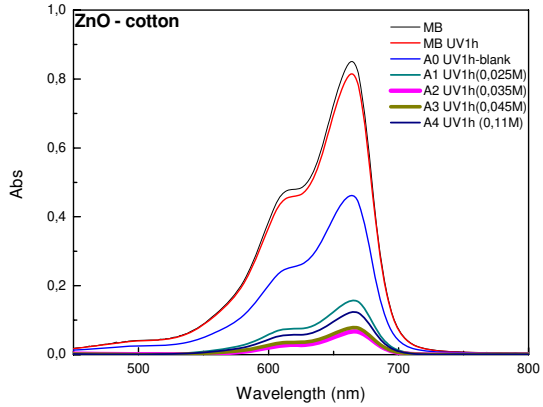

Fig. 4. *UV-Vis absorption spectra of methylen blue in presence by different size of ZnO nanoparticles (applied on cotton 100%) after UV-irradiation, 1h in normal laboratory environment*

As indicated in figure 3 and figure 4 the rate of decolourization increased as the size of ZnO nanoparticles decreased. The rate of decolorization was recorded with respect to the change in the intensity of absorption peak in visible region. The major peak was observed at λmax, i.e., 663nm.

The photocatalytic processes involve several numbers of possible reactions [27]:

- *photoexcitation of a semiconductor* surfaces induces the creation of an electron-hole pair:

$$ZnO + hv \rightarrow ZnO\left(e_{CB}^{-} + h_{VB}^{+}\right); \quad (5)$$

- *separation of electrons and holes*
- *surface reactions*

The remaining holes contribute to the oxidation reactions by generating $\bullet OH$ radicals, either to the decomposition of water

$$H_2O + h_{VB}^{+} \rightarrow H^{+} + \bullet OH\ ; \quad (6)$$

or by the reaction with adsorbed OH^{-}

$$OH^{-} + h_{VB}^{+} \rightarrow \bullet OH\ ; \quad (7)$$

The hydroxyl radical species alone is a strong oxidant for the partial or complete degradation of the dye:

$$dye + \bullet OH \rightarrow oxydation\ products \quad (8)$$

While, on the surface of the catalyst, oxygen is reduced as an electron acceptor to superoxide and this leads to production of $HOO\bullet$ radical which finally plays a strong oxidant role

$$e_{CB}^{-} + O_2 \rightarrow O_2^{-} + H^{+} \rightarrow HO_2^{\bullet} \quad (9)$$

$$HO_2^{\bullet} + O_2^{-} + H^{+} \rightarrow H_2O_2 + O_2 \quad (10)$$

$$H_2O_2 + e_{CB}^{-} \rightarrow OH^{-} + \bullet OH \quad (11)$$

- *degradation of dyes*

So, all these possible reactions contribute to increase the degradation of MB dye by decreasing the size of ZnO nanoparticles.

4. Conclusions

ZnO nanoparticles are prepared using a solvothermal process at temperature of 82°C. The XRD measurement confirms that ZnO consists of würtzite-type nanocrystallites with different crystalline orientation, and (101) the dominating peak. The photocatalytic activity of different ZnO nanoparticles (powder) and with ZnO nanoparticles treated fabric has been demonstrated by the decoloration of MB dye, after irradiating for 60min with ultraviolet light. As a result of the reaction between ZnO nanoparticles and MB dye, the rate of decolorization changed when the size of ZnO nanoparticles changed.

Acknowledgements

The work of Mariana (Busila) Ibanescu was supported by Project SOP HRD – TOP ACADEMIC 78622 and Deutsches Textilforschungszentrum Nord-West GmbH, Krefeld, Hochschule Niederrhein - University of Applied Sciences, Faculty of Textile and Clothing Technology, Mönchengladbach.

References

[1]. H. Tian, J. F. Ma, K. Li and J. J. Li - Vol. 112, (2008), pp. 47-51.

[2]. N. Daneshvar, D. Salari and A. R. Khataee - Journal of Photochemistry and Photobiology A: Chemistry, Vol. 162, (2004), pp. 317-322.

[3]. L. Andronic and A. Duta - Materials Chemistry and Physics, Vol. 112, (2008), pp. 1078-1082.

[4]. Y. Sakata, T. Yamamoto, T. Okazaki, H. Imamura and S. Tsuchiya - Chemistry Letters, Vol. 27, (1998), pp. 1253-1257.

[5]. M. Iwasaki, M. Hara, H. Kawada, H. Tada and S. Ito - Journal of Colloid and Interface Science, Vol. 224, (2000), pp. 202-207.

[6]. H. Tian, J. F. Ma, X. Huang, L. J. Xie, Z. Q. Zhao, J. Zhou, P. W. Wu, J. H. Dai, Y. M. Hu, Z. B. Zhu, H. F. Wang and H. Y. Chen - Materials Letters, Vol. 59, (2005), pp. 3059-3061.

[7]. I. Poulios, M. Kositzi and A. Kouras - Journal of Photochemistry and Photobiology A: Chemistry, Vol. 115, (1998), pp. 175-179.

[8]. J. P. Percherancier, R. Chapelion and B. Pouyet - Journal of Photochemistry and Photobiology A: Chemistry, Vol. 87, (1995), pp. 261-265.

[9]. M. C. Yeber, J. Rodriguez, J. Freer, J. Baeza, N. Duran and H. D. Mansilla - Chemosphere, Vol. 39, (1999), pp. 1679-1683.

[10]. A. A. Khodja, T. Sehili, J. F. Pilichowski and P. Boule - Journal of Photochemistry and Photobiology A: Chemistry, Vol. 141, (2001), pp. 231-236

[11]. C. Marci, V. Augugliaro, M. J. L. Munoz, C. Martin, L. Palmisano, V. Rives, M. Sehhiavello, R. J. D. Tilley and A. M. Venezia - The Journal of Physical Chemistry B, Vol. 105, No. 5, (2001), pp. 1026- 1032.

[12]. C. Lizama, J. Freer, J. Baeza and H. D. Mansilla - Catalysis Today, Vol. 76, (2002), pp. 235-239.

[13]. N. Daneshvar, D. Salari and A. R. Khataee - Journal of Photochemistry and Photobiology A: Chemistry, Vol. 162, (2004), pp. 317-322

[14]. Kathirvelu, S.; Louis, S., Bhaarathi D. - Indian Journal of Science and Technology (2008), 1, 5.

[15]. S.Y. Chu, T.M. Yan, S.L. Chen - J. Mater. Sci. Lett. 19 (2000) 349–352.

[16]. M.S. Tokumoto, V. Briois, C.V. Santilli - J. Sol–Gel Sci. Technol. 26 (2003) 547–551.

[17]. J.H. Kim, W.C. Choi, H.Y. Kim, Y. Kang, Y.- K. Park - Powder Technol. 153 (2005) 166–175.

[18]. L.C. Damonte, L.A. Mendoza Zélis, B. Marí Soucase, M.A. Hernández Fenollosa - Powder Technol. 148 (2004), 15–19.

[19]. M.L. Kahn, M. Monge - Adv. Funct. Mater. 3 (2005) 458–468.

[20]. S. Komarneni, M. Bruno, E. Mariani - Mater. Res. Bull. 35 (2000) 1843–1847.

[21]. X.Y. Zhao, B.C. Zheng, C.Z. Li, H.C. Gu - Powder Technol. 100 (1998) 20–23.

[22]. T. Tani, L. Mädler, S.E. Pratsinis - J. Nanopart. Res. 4 (2002) 337–343.

[23]. Z.R. Dai, Z.W. Pan, Z.L. Wang - Adv. Funct. Mater. 13 (2003) 9–24.

[24]. W.Q. Ao, J.Q. Li, H.M. Yang, X.R. Zeng, X.C. Ma - Powder Technol. 168 (2006) 148–151.

[25]. Spanhel, L., Anderson, M. A. - J. Am. Chem. Soc. (1991), 113, 2826

[26]. Jayant Dharma - *Simple Method of Measuring the Band Gap Energy Value of TiO2 in the Powder Form using a UV/Vis/NIR Spectrometer*, PerkinElmer Technical Center; Aniruddha Pisa-Global Application Laboratory PerkinElmer, Inc. Shelton, CT USA,

[27]. Kensal, S. K.; Kaur, N.; Singh, S. - Nanoscale Res. Lett. (2009), 4, 709–716.

THE ANNALS OF "DUNAREA DE JOS" UNIVERSITY OF GALATI.
FASCICLE IX. METALLURGY AND MATERIALS SCIENCE
N^0. 2 – 2013, ISSN 1453 – 083X

EMPHASIZING PHYSICAL ASPECTS AND APPLICATIONS OF GRAPHENES

Marian BASTIUREA, Magdalena Silvia RODEANU, Dumitru DIMA, Gabriel ANDREI
"Dunărea de Jos" University of Galati, 47, Domneasca Street, RO-800008, Galati, Romania,
email: marian.bastiurea@ugal.ro

ABSTRACT

Graphenes have attracted much attention due to their properties and possible applications. This approach is dedicated to shortly describe the problems related to this promising element. Some aspects concerning physical description and material characteristics are discussed. The paper presents methods for graphenes obtaining and major means of morphological investigation and structural characterization. Also, mechanical, thermal and tribological properties are reviewed. Finally, concluding remarks are drown.

KEYWORDS: graphene, synthesis methods, structure, properties

1. Introduction

Carbon has four allotropic forms: diamond, graphite, fullerene and graphene. Graphenes are formed by one-layer of carbon atoms placed in a honeycomb structure. It is the main material for all allotropic carbon forms: fullerene (0D), nanotubes (1D), or graphite (3D) as it can be seen in Figure 1. They are very light, 1 m^2 weighting only 0.77mg [1]. In their natural state, graphenes are arranged as bulks with maximum 10 layers with monoatomic thickness, through π-π interactions. In order to mix them with other materials these interactions must be weakened.
The major difficulty in synthesis and processing of graphenes is their tendency of aggregation. As the value of graphene characteristics is given by its structure in separate layers, it is essential to avoid their aggregation caused by Van der Vaals forces.

2. Methods of obtaining graphemes

In practice, there are used various methods of obtaining graphenes.

2.1. Mechanical exfoliation

An empirical method is mechanical exfoliation in solution. The method was used by 2010 Nobel laureats for physics, Geim and Novoselov [1].

The strength energy of Van der Vaals interaction is of approximately 2eV/nm^2, and the necessary force for breaking this interaction is of approximately 300nN. This small force can be easily obtained by means of a scotch tape [1]. Another method is the intercalation of small molecules by mechanical exfoliation. Graphite stocking can be substantially reduced by molecule insertion between graphene layers or by non-covalently attaching of polymer molecules between graphene layers, generating graphite intercalation compounds. The graphite layers remain unaltered with guest molecules located in the interlayer galleries [6].

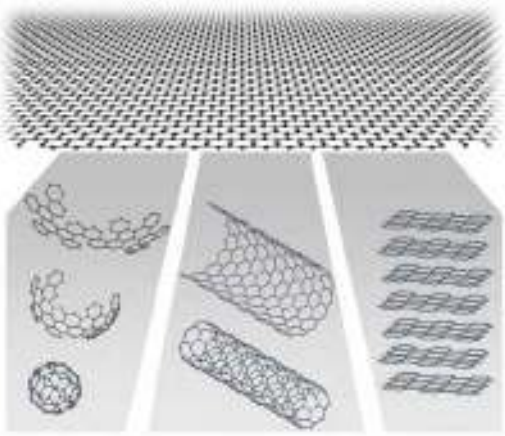

Fig. 1. *Graphene is a building material for carbon materials. It can be wrapped up into 0D buckyballs, rolled into 1D nanotubes or stacked into 3D graphite [1]*

Another method is the intercalation of small molecules by mechanical exfoliation. Graphite stocking can be substantially reduced by molecule

insertion between graphene layers or by non-covalently attaching of polymer molecules between graphene layers, generating graphite intercalation compounds. The graphite layers remain unaltered with guest molecules located in the interlayer galleries [6].

2.2. Chemical vapor deposition (CVD)

Thermal CVD is recommended for obtaining graphene layers on a wide scale at a temperature of approximately 1000^{0}C [20]. A foil of Ni is placed in CVD chamber at a temperature of approximately 1,000^0 C with a diluted hydrocarbon gas. The process starts by inserting carbon atoms into the superficial layer of the Ni substrate, similar to the carburization process. Oversaturation of carbon atoms of the superficial layer is followed by out-diffusing carbon atoms on the surface which forms graphene structures [2, 19]. Plasma enhanced CVD has an advantage compared to the previous method given by the temperature (650^{0}C) and smaller deposition time. It is used a gas mixture of 5-1000% CH_4 in H_2 at a pressure of 12Pa [22].

Another method is thermal decomposition on SiC, where SiC is introduced into a UHV chamber which is heated at 1200^{0}C for a few minutes, sublimation of Si into gas atoms from the superficial layer, allowing carbon atoms to form graphenes [27, 28].

2.3. Chemical reaction

In order to obtain oxidated graphenes, graphite is oxidated with: sulfuric acid, nitric acid and potassium permanganate, potassium dichromate, hydrogen peroxide, using *Hummers* method [2, 4, 3, 10, 12, 24]. Schema of this method can be seen in Figure 2.

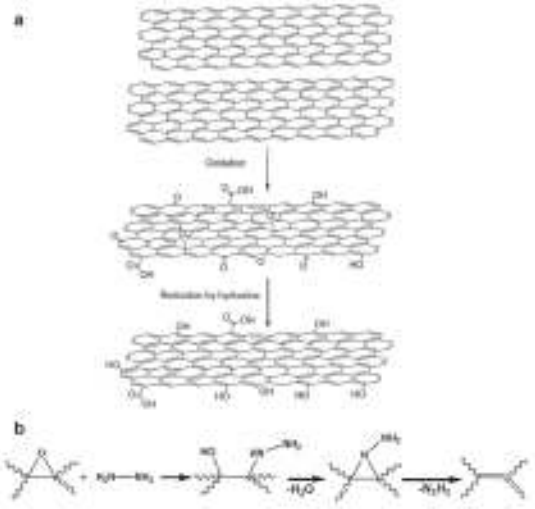

***Fig. 2**. General scheme for a) oxidation of graphite and obtaining graphenes oxide; b) epoxy reduction by hydrazine [3].*

Another method used is *Staudenmaier*, and consists of an oxidation reaction followed by pyrolysis in an oven heated at 1000 ^{0}C [29].

3. Structure characterization

Study of graphene may be done by using optical microscope, SEM, TEM and AFM. Using optical microscope, graphenes could be studied on substrate of SiO and SiN. It was used a silicon layer with an overlayer of 300nm of SiO. The number of layers was identified according to contrast colour as it can be seen in Figure 3 [13].

Using AFM it can be revealed a topographic contrast where no distinction can be made between graphene oxide (GO) and graphene reduce (GR). It was observed a thickness of 1nm for GO and of 0.6nm for GR. The difference in thickness is given by functional oxigen groups which are removed during chemical reductions (Figure 4) [14]. TEM gives the best results when studying the materials at atomic layer.

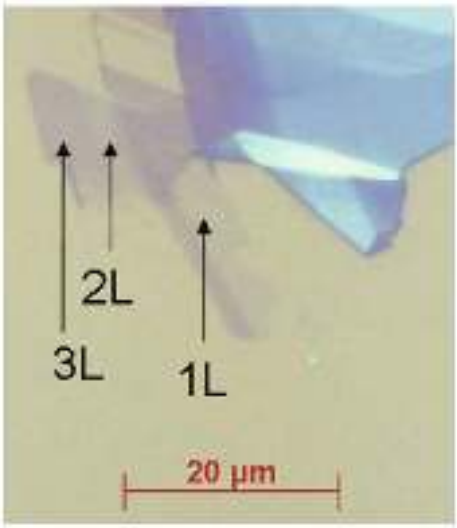

***Fig 3**. Image obtained by means of optical microspy of graphene layers. (1L, 2L, 3L are the number of graphene layers) [13]*

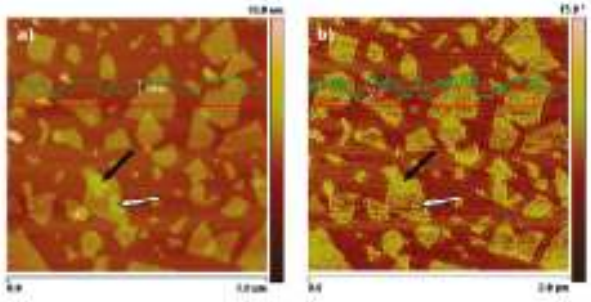

***Fig. 4**. AFM images of graphenes. In a) and b) are GO. a) surface image and; b) cross section image [14]*

The results in studying graphene layers is limited by their resolution at a lower voltage, as a higher voltage may destroy graphene layers. The latest TEM allows for a resolution of 1Å at a 80kV voltage. The images are seen in Figure 5[15]. STEM show us both structure defects and contamination with other atoms. The images are seen in Figure 6 [16].

4. Graphene characteristics

4.1 Mechanical characteristics of graphenes

Besides CNT, graphenes are considered to have the highest Young's modulus, E=1TPa, several times bigger than that of steel (E=0.21 TPa). Taking into consideration the fact that this material has only two dimensions, the value of the modulus was calculated as follows: E^{2D} = 3.41TPa(E^{2D} – Young's modulus in two dimensions). The tensile strength is σ =130GPa and strain is ε = 0.25 measured by AFM [17]. For shear modulus it was measured the value of G= 0.408 TPa [5].

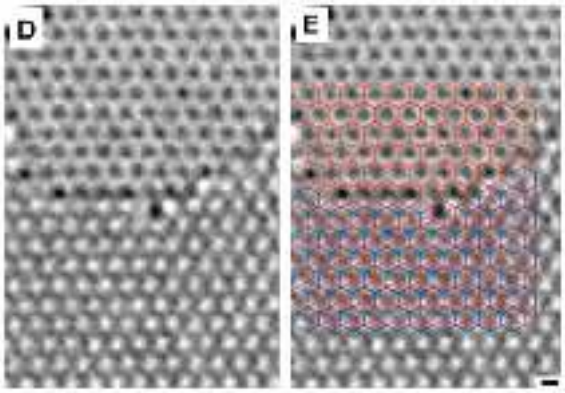

Fig. 5. *D-the upper part represents a single graphene layer and the bottom part represents two- layer graphene. In E, we have two layers of graphene [15]*

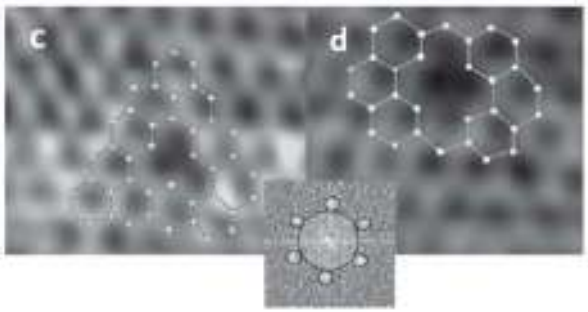

Fig. 6. *Graphene layer with structure defects which can be c) one atom or d) two atoms. The raw image is in the middle [16]*

Young's modulus of graphenes obtained by chemical reduction was 0.25TPa, close to the pristine graphene. The difference in value is due to structure defects, because of the lack of carbon atoms from graphene structure [26]. Other scientists found out that the value of Young's modulus varies according to the thickness of graphenes and Poisson's coefficient remains constant, no matter the variation in graphene thickness. These curves are shown in Figure 7 [8].

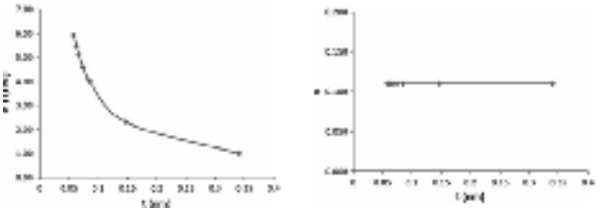

Fig. 7*. a) Young's modulus of graphene sheet (L = 7.137 nm,W = 6.252nm) with various thicknesses; b) Poisson's ratio of graphene sheet (L = 7.137 nm, W = 6.252nm) with various thicknesses [8].*

Starting from the hypothesis that graphenes are ortotropic materials there were established different values of "zigzag" or "armchair" Young's modulus as well as different values of tensile strength and stress for longitudinal and transversal loads [9]. Compressive and tensile behaviour of graphenes have been studied at both longitudinal and transversal loads, bigger differences being noticed during compressive loads between the two methods of applying load, Figure 8 [23].

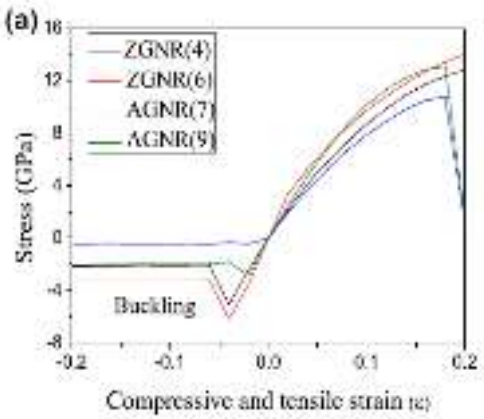

Fig. 8*. Compressive and tensile behaviour of graphenes at both longitudinal (ZGNR4 si ZGNR6) and transversal loads (AGNR7si AGNR9) [23]*

After measurements it has been noticed that the variation of elastic properties of graphenes is non-linear, and can be expressed under a uniaxial load as folows:

$$\sigma = E\varepsilon + D\varepsilon^2 \quad (1)$$

where σ represents the strength, E – Young's modulus, σ is the symmetric second Piola-Kirchhoff stress, ε – uniaxial Lagrangian strain, D – third-order elastic constant [21].

***Tab. 1**. Properties of graphenes [7]*

Measured values	*Armchair*	*Zigzag*
Young's modulus	710GPa	737GPa
Tensile failure strain	0.269	0.198
Tensile failure stress	120GPa	95GPa
Failure rigidity	241GPa/nm	250GPa/nm

Graphene adhesion to other materials is described as (2):

$$\eta = Et^3h^2 / \Gamma\lambda^4 \quad (2)$$

where E –Young's modulus, Γ – adhesion energy between graphene and substrate, h- asperities height, λ – spacing between asperities, t – asperities thickness, η – the competition between Γ and the elastic energy of the deforming to conform a rough surface.

For h<<1nm the graphene conform to the rough surface while for h>1 it can only partially conform [25].

4.2. Thermal properties

In order to determine the value of thermal conductivity of graphenes, it has been suspended a layer of graphene in a substrate of silicon oxide/silicon and a focused laser light was pointed towards this. Thermal conductivity of graphenes, measured with micro-Raman spectroscopy is very high, reaching 5000W/mK compared to copper (400W/mK), carbon steel (43W/mK) or diamond (0.2W/mK) and it is higher than CNT (single wall CNT ≈3500W/mK and multi wall CNT≈3000W/mK) [18]. Graphene can be used in electronic devices where an important problem is dissipation of thermal energy accumulated during functioning, these properties thus giving the possibility of replacing silicon as material for electronic microdevices.

4.3. Tribological properties of graphenes

For studying the wear behaviour of graphene there have been used values of loads smaller than 250nN, without causing graphenes breakage. Wear behavior of graphene can be affected by the number of graphene layers, thus a small number of layers (1-4) have a different friction behavior than a bigger number (13-16). Thus graphenes with more than 5 layers have a similar friction behaviour as graphite. Graphenes used for determining wear behaviour have been deposited on a silicon substrate by mechanical exfoliation. Using AFM it has been studied the graphene friction behaviour using loads with values between 30 and 5nN [11]. Initially AFM height of the tip came in contact with the cantilever and friction force has been measured on a 20μm distance for 2 cycles. The cantilever was retracted slightly to lower the applied load and the friction force was measured again. This process was repeated until the tip got detached from the specimen surface due to excessive negative load (Figure 9) [11].

***Fig. 9**. Schematic of AFM tip/specimen contact under negative and positive applied loads [11]*

Graphenes used were 6nm thick. Figures 10 and 11 show the image obtained by AFM of graphenes used in the experiment [11].

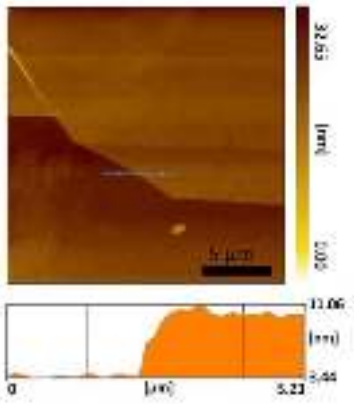

***Fig. 10.** AFM image of the graphene specimen, 2D profiles [11]*

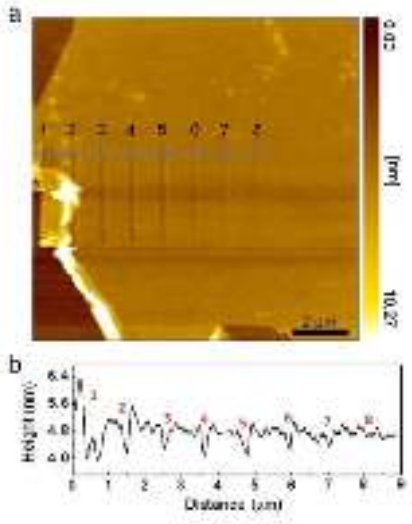

***Fig. 11.** (a) AFM image of wear tracks and (b) the cross-sections of wear tracks [11]*

5. Conclusions

Due to its unique properties (mechanical, electrical, thermal, optical) graphenes applications are diverse:

- electronic devices with integrated circuits, touchscreens, LCDs, LEDs, organic photovoltaic cells, transistors, frequency multipliers;

- water desalination, ethanol distillation, thermal management materials, optical modulators, additives in coolants, ultracapacitors, engineered piezoelectricity, biodevices, single-molecule gas detection.

Meanwhile, the main problem remains graphenes mass production and a price as small as possible. Preparation methods must solve the transfer, the number of layers or graphenes folding from the substrate they have been chemically deposited.

References

[1]. Geim, A.K., Novoselov K.S. - *The Rise of graphene.* Nature materials 6:183-191, (2007).
[2]. Singh, V., Joung D. - *Graphene based materials: Past, present and future.* Progress in Materials Science 56:1178-1271, (2011).
[3]. Stankovich, S., et al. - *Synthesis of graphene based nanosheets via chemical reduction of exfoliated graphite oxide.* Carbon 12:1558-2003, (2007).
[4]. **Schniepp H.C**., et al. - *Functionalized single graphene sheets derived from splitting graphite oxide.* The Journal of Physical Chemistry B 110:8535-8539, (2006).
[5]. Faccio R., et al. - *Mechanical properties of graphene nanoribbons.* Journal of Physics: Condensed Matters 21:1 -29. (2009).
[6]. Li X., et al.2008. *Highly conducting sheets and Langmuir-Blodgett films.* Nano Letters 538-541.
[7]. Georgantzinos S.K., et al. - *Graphene characterization: a fully non-linear spring-based finite element prediction.* Physica E 43:1833-1839, (2011).
[8]. Alzebdeh K. - *Evaluation of the in-plane effective elastic moduli of single-layered graphene sheet*. Journal of Mechanics and Materials in Design. 8:269-278, (2012).
[9]. Tkachev S.V., et al. - *Reduced graphene oxide.* Inorganic Materials 48:796-802, (2012).
[10]. Xianoqing S., et al. - *A simple method for preparing graphene nano-sheets at low temperature.* Advanced Powder Technology 24:317-323, (2013).
[11]. Li-Yu et al. - *Friction and wear characteristics of multi-layer graphene films investigated by atomic force microscopy.* Surface&Coating Technology 205:4864-4869, (2011).
[12]. Yi - Tao. - *High-concentration organic solutions of poly(styrene-cobutadiene-co-styrene)-modified graphene sheets exfoliated from graphite.* Carbon 49:3259-3537, (2011).
[13]. Park, G.S. et al. - *G'band Raman spectra of single, double and triple layer graphene.* Carbon 47:1303-1321, (2009).
[14]. Paredes J.L.,et al. - *Atomic force and scanning tunneling microscopy imaging of graphene nanosheets derived from graphite oxide*. Langmuir 17:5957-5982, (2009).
[15]. Myer J.C., et al. - *Direct imaging of lattice atoms and topological defects in grapheme membranes*. Nano Letters 4:3582-3590, (2008).
[16]. Gas M.H., et al. 2008. *Free-standing graphene at atomic resolution.* Nature Nanotechnology5: 676- 681.
[17]. Lee, C.,et al. - *Measurement of the elastic properties and intrinsic strength of monolayer graphene.* Science 385-388, (2008).
[18]. Balandin A., et al. - *Superior thermal conductivity of single layer graphene.* Nano Letters 8:902 -907, (2008).
[19]. Yanwu Z., et al. - *Graphene and Graphene Oxide: Synthesis, Properties, and Applications.* Advanced Materials 22:3906-3924, (2010).
[20]. Reina A., et al. - *Large Area, Few-Layer Graphene Films on Arbitrary Substrates by Chemical Vapor Deposition.* Nano Letters 9:30-35, (2008).
[21]. Changgu, L.,et al. - *Measurement of the elastic properties and intrinsic strength of monolayer graphene.* Science 321:385-397, (2008).
[22]. Drayer D.,et al. - *The chemistry of graphene oxide.* Chemical Society Rewiews 39:228-240, (2009).
[23]. Wu G., et al. - *I–V Curves of graphene nanoribbons under uniaxial compressive and tensile strain.* Chemical Physics Letters 559:82-97, (2013).
[24]. **Park S**. et al. - *Aqueos suspension and characterization of chemically modified graphene sheets.* Chemistry of Materials 20:6592-6596, (2008).
[25]. Bunch, J.S., - *Adhesion mechanics of graphene membranes.* Solid State Communications 152:1359-1364, (2012).
[26]. Gomez N.C., et al. - *Elastic properties of chemically derived single graphene sheets.* Nano Letters 8:2045-2049, (2008).
[27]. Penuelas J., et al. - *Surface morphology and characterization of thin grapheme films on SiC: effect of substrate.* Physical Revue B 79:876-890, (2009).
[28]. Marchetto D., et al. - *Friction and wear on single-layer epitaxial graphene in multi-asperity contacts.* Triblogy Letters 48:77-82, (2012).
[29]. Kim H., et al. - *Graphene/polyetylene nanocomposites: Effect of polyetylene functionalization and blending methods.* Polymer 52:1837-1846, (2011).

THE ANNALS OF "DUNAREA DE JOS" UNIVERSITY OF GALATI.
FASCICLE IX. METALLURGY AND MATERIALS SCIENCE
N^0. 2 – 2013, ISSN 1453 – 083X

HIGH-K DIELECTRIC INORGANIC-ORGANIC HYBRID THIN FILMS FOR FIELD EFFECT TRANSISTORS (FETFT)

Elena Emanuela VALCU (HERBEI)[1], Viorica MUSAT[1], Susanne OERTEL[2] and Michael JANK[2]

[1]Centre of Nanostructures and Functional Materials, Faculty of Materials and Enviromental Engineering, "Dunărea de Jos" University of Galati, 47, Domneasca Street, RO-800008, Galati, Romania,
[2]Fraunhofer Institute for Integrated Systems and Device Technology IISB, Erlangen, Germany
emails: viorica.musat@ugal.ro.; Michael.Jank@iisb.fraunhofer.de

ABSTRACT

The paper discusses the challenges to develop thin films transistors for flexible transparent electronics, displays etc. The sol-gel preparation of hybrid thin films based on dielectric oxides nanoparticles (SiO_2 NPs, ZrO_2 NPs) and polymethy methacrylate (PMMA) is presented. The high-k hybrid thin films, evaluated as gate dielectric in a MIM structures, were deposed by spin-coating teqhnique. The multi-layers (thin films) configuration of MIM structures were investigated by scanning electron microscopy (SEM) and electrical properties. The I-V and C-V curves showed a better dielectric behavior of hybrid films with respect to the simple PMMA films. Dielectric constant values of 2.1, 3.4 and 5.4 have been obtained for PMMA, ZrO_2-PMMA and SiO_2-PMMA films, respectively.

KEYWORDS: hybrid dielectric materials, thin film transistors, morphology, I-V and C-V measurements

1. Introduction

Hybrid materials are a very interesting class of materials that combines the benefits of both inorganic and organic components. [1]. The sol-gel method is the most convenient and suitable method to get the coupling between organic and inorganic phases at the interface level [2-3]. Some of the advantages of this method include low temperature processing as well as high control in the final organic to inorganic phase composition. These advantages are of special interest in the fabrication of flexible electronic devices where the processing temperature is limited by the low processing temperature tolerated by the substrate. In hybrid systems, the poly(methyl methacrylate) (PMMA) organic component provides large area substrate compatibility and flexibility at low processing temperature, while oxide nanoparticles as SiO_2 and ZrO_2 increase the dielectric characteristics of resulting hybrids.

SiO_2-PMMA is one of the most intensively studied hybrid systems in the recent years. Highly transparent SiO_2- PMMA films with different organic - inorganic molar ratios obtained by sol-gel process were reported [4-5]. The properties of the SiO_2-PMMA films such as hardness, refraction index, etc. can be tuned by choosing the appropriated initial compositions of the precursors. There are two principal different routes to introduce inorganic particles into organics. One method is to incorporate inorganic domains into polymer matrices using the sol-gel method. In addition, the polymer may stay contaminated by unreacted educts or byproducts of the precipitation reaction. Another method was blending of preformed inorganic particles into the organic medium. In contrast to the former route, this method is more compatible with the needs of an industrial production [6, 7].

The replacement of rigid substrates with flexible polymeric ones requires novel dielectrics, semiconductors and contacts materials with good mechanical flexibility, low processing temperatures and acceptable performance. As mentioned before, for flexible electronics, PMMA has been assessed as an option for the gate dielectric due to its high resistivity, chemical resistance, thermal stability, mechanical flexibility, low cost and high dielectric constant similar to SiO_2 [8].

One of the most promising high-k dielectric for widespread application is zirconium oxide (ZrO_2), used as gate dielectric. Zirconia is a stable metal oxide with a high dielectric constant (15–25) [9] and a large band gap (5.8eV). It has been reported that ZrO_2 has the lowest leakage current [10]. Moreover, it

is a promising material for the fabrication of large-area flexible displays because ZrO_2 films can be transparent and have good adhesion with plastic substrates [11, 13]. These properties have prompted further studies of ZrO_2-PMMA as an alternate gate dielectric material. The understanding of the electrical behavior presents a challenge for any alternative gate dielectric candidate.

The paper presents a study on the electrical properties of SiO_2-PMMA and ZrO_2-PMMA dielectric thin films deposited using a modified sol–gel route. The resulting hybrid thin films were evaluated as gate dielectric using MIM structures. Electrical properties of the hybrid system were studied using current–voltage (I–V) and capacitance–voltage (C–V) data, at 1 MHz frequency.

2. Experimental details

2.1. Film preparation

ZrO_2 (<50nm) and SiO_2 (5nm) nanoparticles used for the preparation of hybrid films were purchased from Sigma Aldrich and PMMA (495kw) from MICRO CHEM. SiO_2-PMMA and ZrO_2-PMMA films were prepared from solutions of 1:1 and 4:1 molar ratios, for both systems. The solution was spin coated for 20 seconds in air, onto the n-doped Si substrates covered with a layer of 100 nm tantalum. The as-deposed films were thermally treated on hot plate at 120^{o}C for 30 minutes.

Before film deposition, the substrates were cleaned using the following procedure: washed in water for three times, dipped in isopropanol for 1 minute and cleaned with water, dried with nitrogen stream and hotplate for 5 minutes at 120^{o}C. Finally, metallic aluminum contacts for the capacitor were thermally evaporated through a shadow mask with different areas (180, 320 and 680μm diameters) resulting a multi-layer structure (Figure 1a).

2.2. Film characterization

The thickness of the films was measured from SEM cross-section images obtained with a Zeiss SEM-Raith 150 equipment operated at 10 kV. Aluminum contacts (300nm) were thermally evaporated through a shadow mask on spin-coated hybrid dielectric film.

The I-V and C-V curves were measured in a Metal-Insulator-Metal (MIM) structure (Fig. 1a), using an Agilent 4156 Precision Semiconductor Parameter Analyzer and an HP 4277A Parameter Analyzer, respectively, at 1MHz. Figure 1a depicts a schematic representation of the MIM gate structure used for I-V and C-V measurements, and figure 1b shows a top view optical image of the investigated structure.

The dielectric constant (k) value was calculated from the measured capacitance (C), based on the equation (1):

$$C = \frac{k \cdot \varepsilon_0 \cdot A}{d} \quad (1)$$

where ε_0 is the permittivity of free spaces, d is the dielectric thickness, C ***is the*** capacitance (F), k is the dielectric constant and A is the capacitor area [12].

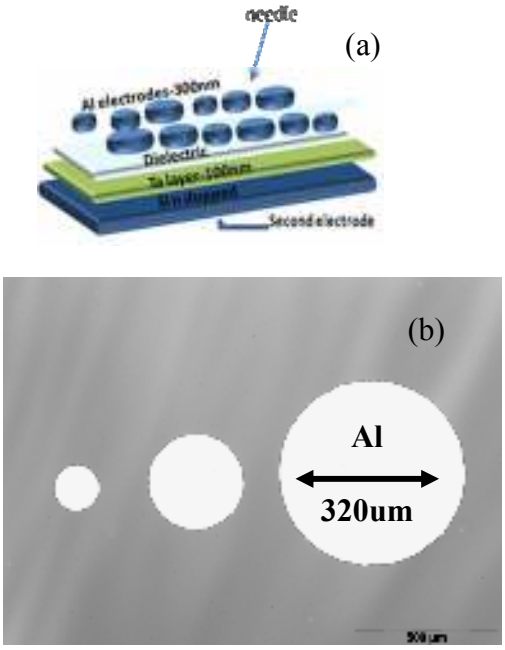

Fig. 1. *Schematic representation of MIM structures (a) and top-view image of the obtained MIM devices (b)*

3. Results and discussion

Fig. 2 show the SEM images of obtained hybrid films with 1:1 and 4:1 molar ratio between oxide nanoparticles and PMMA. For ZrO_2-PMMA, SEM images shows a relatively homogeneous dispersion of nano particle aggregates, the spaces between them being filled by polymer matrix (Fig. 2d-e), resulting in the formation of cross-linked organic - inorganic phases of hybrid films. The thickness of the dielectric layer, is about 150 nm (Fig. 2b). The hybrid films containing silica nanoparticles have a much higher roughness than zirconia films, their thickness varying between 200-600 nm (Fig. 2a). The thickness of the layer of hybrids is increasing by adding nanoparticles, as we saw from the top view of film with PMMA, whose thickness is 70nm (Fig. 2c). For silica films the spaces between agglomerates are bigger than hybrids containing zirconia (Fig. 2f-g). We believe this is due to particle agglomeration because of a weak dispersion in the reaction medium.

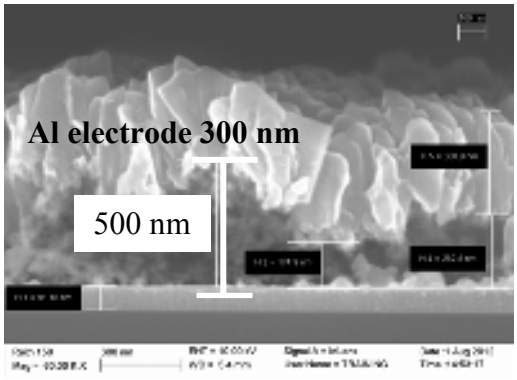

a.

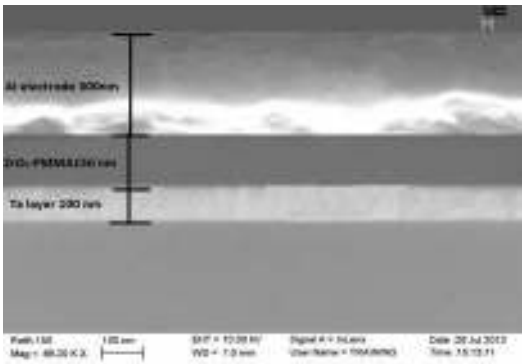

b.

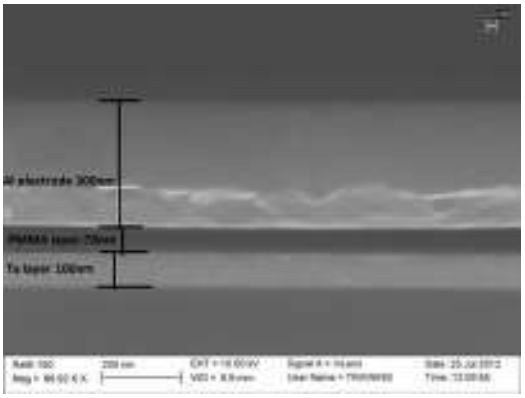

c.

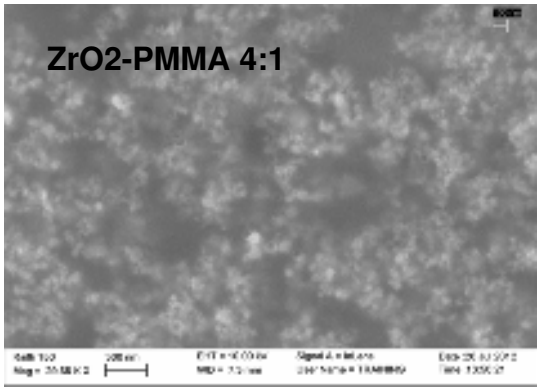

d.

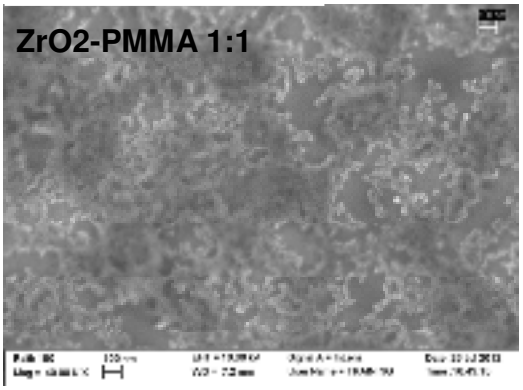

e.

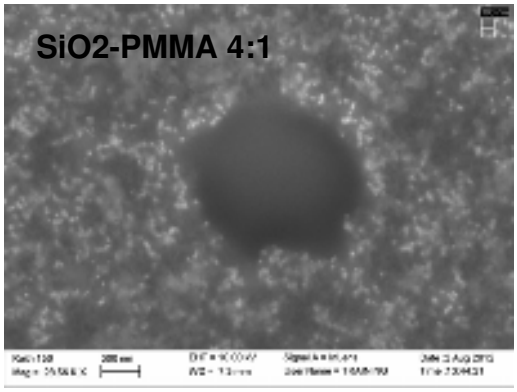

f.

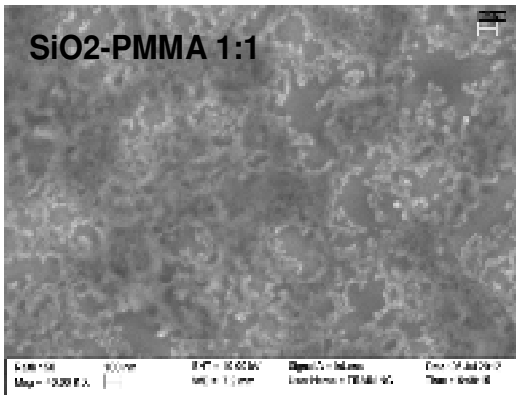

g.

Fig.2. *Cross section SiO_2-PMMA (a), ZrO_2-PMMA (b), PMMA (c) and top views SEM micrographs of hybrid thin films ZrO_2-PMMA 4:1 (d), ZrO_2-PMMA 1:1 (e), SiO_2-PMMA 4:1 (f), SiO_2-PMMA 1:1 (g)*

From the C–V curves (Figs. 3 and 4), were calculated the values of dielectric constant measured at 1MHz frequency in the voltage range ±1 volts for silica hybrid and ± 4 volts for zirconia hybrid. The dielectric constant of devices is summarized in *Table 1*.

Table 1. *Electric parameters of films*

Sample	Capacitance	Thickness, d	Dielectric constant
	[F]	[nm]	[k]
PMMA	$5.39*10^{-11}$	70	2.1
SiO_2-PMMA	$3.5*10^{-10}$	300	3.4
ZrO_2-PMMA	$4.7*10^{-10}$	200	5.4

From *Table 1*, one can observe that the addition of oxide nanoparticles increases the dielectric constant of PMMA. Relevant growth of dielectric constant values is observed in films containing zirconia nanoparticles.

The increment of the capacitance values depends on the ability of existing carriers (holes in this case for n-type substrate) to follow the variation of the applied signal. It is well known that the dielectric permittivity of a material is proportional to its electronic polarization.

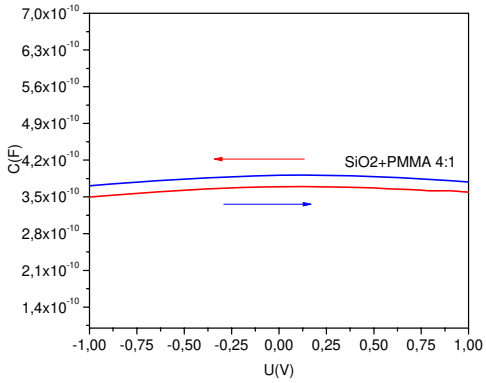

Fig.3. *C-V curve for SiO_2-PMMA thin film*

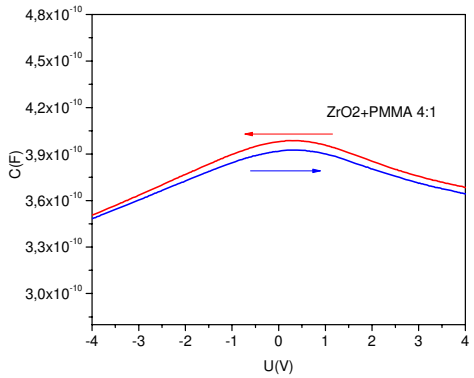

Fig.4. *C-V curve for ZrO_2-PMMA thin film*

Materials with polar groups (i.e. C=O) have large dielectric constants due to the orientation of their electrical dipoles in an applied electric field. Among the organic functional groups, –OH has the highest molar polarization [14].

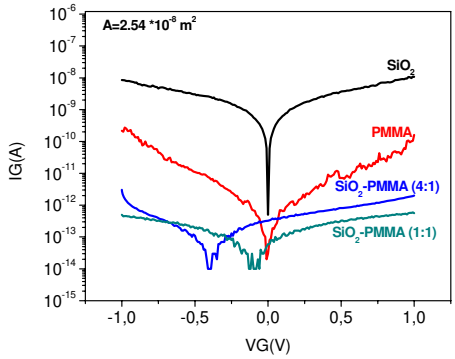

Fig. 5. *I-V curves for SiO_2, PMMA and SiO_2-PMMA thin film different molar ratio*

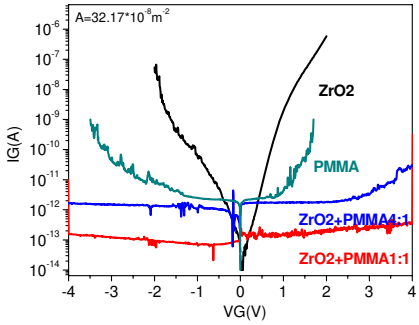

Fig. 6. *I-V curves for ZrO_2, PMMA and ZrO_2-PMMA thin film at different molar ratio*

Polar polymers have a tendency to retain moisture, which further increases their dielectric constants. Also, it is known that for materials with a large number of carbon atoms the polarity increases in the order of single, double and triple chemical bonds, due to enlarged mobility of the *p*-type electrons [15]. The total polarization is the result of the contribution of different factors: type of chemical bond (electronic, atomic or ionic) and polarization responses, at least one of these polarization modes exhibited in dielectric materials. At high frequencies the electronic responses dominate, while ionic contribution is important at low frequencies.

The I-V curves of silica films (Fig. 5) show a dielectric behavior with low leakage current values: 10^{-12} to 10^{-6} A at ±1 volts. By mixing the PMMA with the inorganic SiO_2, the values of the current decreases, being the lowest for the sample with higher inorganic content. The sample with 4:1 molar ratios has a lower leakage current than the sample with 1:1 molar ratio. For zirconia hybrid films, the voltage breakdown increases up to ±15 V (not presented here) with the increase of molar ratio of inorganic/organic content at 4:1 compound. In the same time, the leakage current (Fig. 6) decreases from 10^{-12} A to 10^{-13} when the molar ratio increases at 4:1.

Conclusions

Hybrid SiO_2-PMMA and ZrO_2-PMMA films used as dielectrics in MIM stacks were prepared.

From Capacitance-Voltage electrical data, an increase of dielectric constant of the PMMA films was observed by dopping with silica and zirconia nanoparticles; 3.4 for SiO_2-PMMA and 5.4 for ZrO_2-PMMA hybrid films, respectively.

The I-V curves show a dielectric behavior with values for the leakage current between 10^{-14} and to 10^{-11} A for silica-based hybrid films and 10^{-14}-10^{-12} A for zirconia-based hybrid films. SiO_2-PMMA and ZrO_2-PMMA inorganic-organic films offer attractive opportunities for flexible electronic applications, due to the combined functional features of both organic and inorganic components in a single material.

Acknowledgements

This work was supported by the projects FP7-POINTS (Printable Organic Inorganic Transparent Semiconductor Devices) No. 263042/2011 and CAPACITATI M-III EU 156/2011-POINTS.

The work of Elena-Emanuela Valcu was supported by Project SOP HRD – TOP ACADEMIC 78622.

References

[1]. C. Sanchez: J. - Mater. Chem. Vol. 15 (2005) p. 3557.
[2]. C. Sanchez, B. Julian, P. Belleville, M. Popall: J. Mater. Chem. Vol. 15 (2005) p. 3559.
[3]. Sh. Al-Kandary, A.A.M. Ali, Z. Ahmad - J. Mat. Sci. Vol. 41 (2006) p. 2907.
[4]. J.L. Almaral-Sanchez, E. Rubio E, A. Mendoza-Galvan and R. Ramirez-Bon - J Phys. Chem. Solids Vol. 600 (2005) p. 1660.
[5]. E. Rubio, J. Almaral, R. Ramirez-Bon, V. Castano, V. Rodriguez - Opt. Mat. 27 (2005) p. 1266.
[6]. Lee, L.H. and Chen, W.C. - Chem. Mater., (2001), 13: 1137
[7]. Xiong, M.N., Zhou, S.X., Wu, L.M., Wang, B. and Yang, L. - Polymer, (2004), 45: 8127
[8]. Puigdollers J, Voz C, Orpella A, Quidant R, Martın I, Vetter M, Alcubilla R - Pentacene thin-film transistors with polymeric gate dielectric. Org Electron (2004)5:67–71.
[9]. C. C. Fulton, T. E. Cook, G. Lucovsky, and R. J. Nemanich, - *Interface instabilities and electronic properties of ZrO2 on silicon (100)*, *Journal of Applied Physics,* vol. 96, no. 5, (2004), pp. 2665–2673.
[10]. W. J. Qi, R. Nieh, B. H. Lee et al. - *MOSCAP and MOSFET characteristics using ZrO2 gate dielectric deposited directly on Si,* in Proceedings of the 1999 IEEE International Devices Meeting (IEDM), (1999), pp. 145–148, December.
[11]. W. J. Qi, R. Nieh, B. H. Lee et al. - *Performance of MOSFETs with ultra thin ZrO2 and Zr silicate gate dielectrics*, in Proceedings of the 2000 Symposium on VLSI Technology, (2000), pp. 40– 41, June.
[12]. M. D. Morales-Acosta, M. A. Quevedo-Lopez, Bruce E, Gnade, R. Ramirez-Bon - J Sol-Gel Sci Technol (2011) 58:218–224 DOI 10.1007/s10971-010-2380.
[13]. C. Sanchez - J. Mater. Chem. Vol. 15 (2005) p. 3557.
[14]. Ogura I In Nalwa HS (ed) - *Handbook of low and high dielectric constant materials and their applications*, vol I—materials and processing. Academic Press, Boston, (1999).
[15]. Ho PS, Liu J, Morgen M, Kiene M, Zhao JH In: Murarka SP, Eizenberg M, Sinha AK(eds) - *Inter layer dielectrics for semiconductor technologies.* Elsevier Inc, London, (2003).

THE ANNALS OF "DUNAREA DE JOS" UNIVERSITY OF GALATI.
FASCICLE IX. METALLURGY AND MATERIALS SCIENCE
N^0. 2 – 2013, ISSN 1453 – 083X

FABRICATION AND CHARACTERIZATION OF COBALT/IRON COMPOSITE COATINGS

Livia GHEORGHIES
"Dunărea de Jos" University of Galati, Faculty of Materials Engineering and Environment,
111, Domnească Street, RO-800201, Galati, Romania
email: cgheorgh@ugal.ro

ABSTRACT

Cobalt/iron composite coatings are used in micro-equipments due to their high magnetic saturation values and Curie temperatures, as magnetic nanoparticles capable of killing cancer cells, for magnetic data storage and magnetic resonance imaging (MRI) and in coatings, plastics, nanowire, nanofiber and textiles as well as in certain alloys and in catalyst applications. Cobalt/iron composite coatings were prepared by using two types of solution consisting of oleic acid in diphenyl ether and cobalt formate strongly stirred then centrifuged and drayed. Obtained coatings were subjected to chemical and structural analysis by using EDAX and XRD techniques. Some magnetic characteristics have been estimated by drawing the hysteresis loop for various thicknesses of coatings.

KEYWORDS: cobalt/iron, coating, structure, magnetic properties

1. Introduction

For the last ten years, research in nanofield has been focused on preparing and studying the influence of dimension and shape of nanomaterials or nanostructures obtained by different techniques or methods on some magnetic, mechanic, electric or optic properties [1-3]. Applications of cobalt/iron nanocrystals include ones in electromagnetic machines and micro-equipments due to their high magnetic saturation values and high Curie temperatures, as magnetic nanoparticles capable of killing cancer cells, for magnetic data storage and magnetic resonance imaging (MRI) and in coatings, plastics, nanowire, nanofiber and textiles as well as in certain alloys and catalyst applications. For example, the papers of J. Park, T. Hyeon or S. Sun and their collaborators showed that certain magnetic properties are greatly reduced with decreasing size of spherical nanoparticles [4-6]. Other scientists such as N. Cordente or M. Aslam have been made attempts in order to improve the magnetic properties of nanocrystals by preparing anisotropic 1D nanostructured materials [7, 8] having the shape of rods or wires. In 2D nanostructures superior magnetic properties are expected, such as made by Y. Leng and co-workers who prepared nickel nanosheets having enhanced magnetic properties [9] or by V. F. Puntes together his collaborators who synthesized 2D disk-shaped cobalt packed crystal structure [9, 10].

In this paper it is reported the possibility to prepare 2D structure, namely cobalt/iron coatings, having interesting magnetic properties. The presence of iron in structure leads to increasing of coercive force of prepared 2D structures and it can be explained taking into account the enhanced anisotropic energy of cobalt in the presence of iron atoms, when thermodynamically unfavourable shapes appear. The anisotropic growth is induced by twin planes and is proposed to explain the formation of cobalt/iron coatings [11].

2. Experimental research

In order to prepare cobalt/iron coatings, two types of solution were initially introduced into separate flasks. The first flask contains 20ml diphenyl ether [$C_{12}H_6Br_4O_2$] solution of oleic acid [$C_{18}H_{34}O_2$] (6.0mmol) and cobalt formate [$Co(CHO_2)_2$] (3.0mmol). The mixture was strongly stirred and maintained at a constant temperature of 200^{o}C and in a nitrogen atmosphere.

The second flask contains a solution of iron pentacarbonyl [Fe $(CO)_5$] (2.0 mmol) and oleyl amine [$CH_3(CH_2)_7CH{=}CH(CH_2)_8NH_2$] (16 mmol). This solution was taken and quickly introduced in the first flask. The resulted mixture was maintained for half an hour at the same temperature of 200^{o}C, then it was cooled to room temperature, precipitated with ethanol and, finally, it was separated by centrifugation. Then,

the precipitate was dried and subjected to structural characterization.

In figure 1 the technological schema of cobalt/iron coatings preparation process is presented. The composition of sample was estimated by EDAX technique (Quanta 200 EM); the structural analysis was made by XRD method using monochromatic Cu Kα radiation (DRON-3), and the morphology and size distribution were examined by SEM (Quanta 200 EM) and TEM (Phillips CM200) techniques. Relating to magnetic properties, they were investigated with an original device that allows carrying out the hysteresis loops by applying a magnetic field up to 12.10^4 A/m.

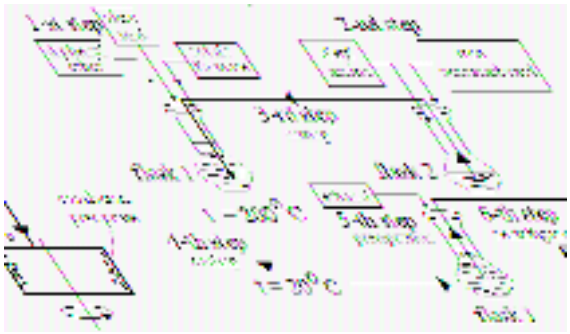

***Fig. 1**. Technological scheme of cobalt/iron composite coatings preparation*

3. Results

The chemical composition of the cobalt/iron coating was determined by EDAX and consists of two or three percent iron that probably has diffused into the crystalline lattice of cobalt. The XRD pattern presented in Figure 2 reveals that the prepared coatings are represented only of cobalt which has a hexagonal close-packed structure with lattice constants of a = b= 2.508 Å and c = 4.069 Å. These results show that indeed it is obtained pure cobalt. No signals from cobalt format are observed and there are not present iron oxides or the formation of amorphous iron in the sample even if the initial molar ratio of components is 1:2. It is important to control the mixture temperature and the ratio of iron pentacarbonyl to oleic acid. If the temperature is lower than 200^{o}C cobalt formate is difficult to decompose.

The SEM and TEM study shows that the cobalt/iron coatings present structural units having a hexagonal shape, with edge lengths varying from several tens to several hundreds of nanometers. The maximum thickness of prepared coatings was estimated to be about 120 nm. The thickness can be controlled by the quantity of iron pentacarbonyl introduced into the first solution that contains cobalt format and oleic acid. Due to the strong magnetic interaction between different structural units, these tend to overlap resulting in an anisotropic growth of coatings [15].

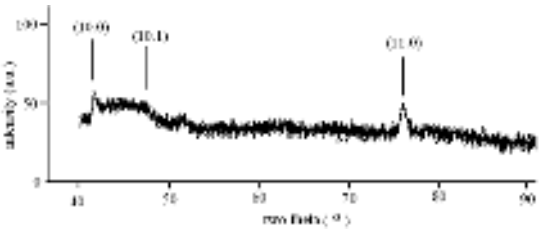

***Fig. 2**. XRD pattern of cobalt/iron composite coatings*

There are several mechanisms trying to explain this behaviour. The most representative one considers that the organic molecules influence the growing process or promote the addition of adsorptive atoms to the specific crystal faces. In figure 3, typical SEM (a) and HRTEM (b) images are presented when the edges of the different coatings are clearly distinguished although there is an overlap.

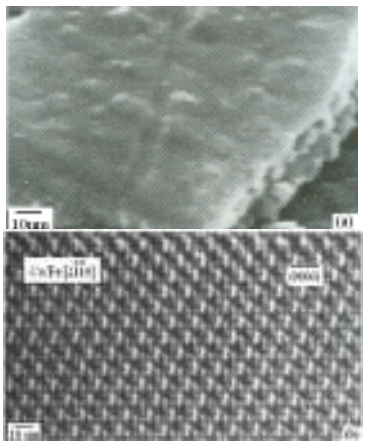

***Fig. 3**. SEM (a) and HRTEM (b) images of cobalt/iron composite coatings*

This provides good evidence that the coatings appear to be transparent under the electron beam. The transparent nature under the electron beam implies the ultra-thin cobalt/iron coatings. Comparable results were observed for other metals. For example, Y. Leng, N. Malikova, R. J. Cao and C. Salzemann obtained similar morphologies in case of nickel [9], gold [12], silver [13], and copper [14], respectively. The organic molecules, such as oleic acid and oleyl amine, have no special effect on cobalt anisotropic growth in our process. In complete contrast, by using iron pentacarbonyl to the reaction system, a large quantity of cobalt/iron coatings is produced after 15-20min. This implies that the iron species play an

important role in the formation of cobalt/iron coatings. Iron atoms are produced immediately after using iron pentacarbonyl into the diphenyl solution, and then they are etched by oleic acid in the diphenyl ether during their growth. Iron atoms will be locked into twinned morphology because the twinned nanoparticles have a lower overall surface energy [16]. Finally, the adsorption of cobalt atoms along the plane having smaller atom density leads to the formation of coatings.

The magnetic properties the prepared cobalt/iron coatings were performed by recording at the room temperature of the normalized hysteresis loop. Figure 4 shows the normalized hysteresis loops for different thicknesses that range from 20 to 120 nm. It can see that the squareness and coercivity decreasing with increasing thickness and this behaviour can be connected to the grain size. Supposing a rotational magnetization process of slightly interacting fine particles, in fact, film coercivity is inversely proportional to particle size [17].

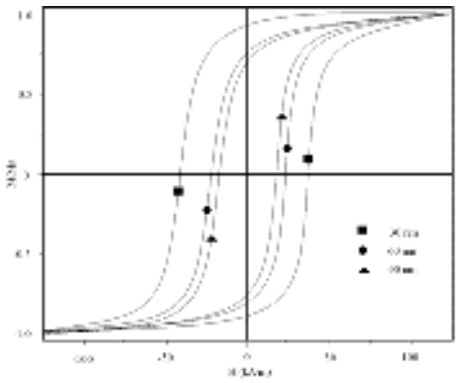

***Fig. 4**. Hysteresis loops of cobalt/iron composite coatings having various thicknesses*

The hysteresis loops of cobalt/iron coatings show that they have a typical ferromagnetic behaviour. The values of the coercitive force of obtained coatings depend on their thickness and it is superior both to the cobalt bulk and cobalt nanospheres ones. This aspect is probably due to their 2D structure.

4. Conclusions

The present paper shows the possibility to prepare by a synthesis process cobalt/iron coatings having a crystalline structure. Iron atoms and oleic acid have a determinant role in the synthesis process, they lead to the growth of a special structure having interesting magnetic properties. The magnetic properties of cobalt/iron coatings were studied taking into account hysteresis loops that are strongly influenced by the thickness of coatings. The coercitive force of cobalt/iron composite coatings is superior to the growth of a bulk or cobalt nanospheres.

References

[1]. F. Dumestre, B. Chaudret, C. Amiens, P. Renaud, and **P. Fejes** - Science **303**, 821, (2004)
[2]. S. H. Sun, and **H. Zeng** - J. Am. Chem. Soc. **124,** 8204, (2002)
[3]. E. V. Shevchenko, D. V. Talapin, H. Schnablegger, A. Komowski, O. Festin, P. Svedlindh, M. Haase, and H. Weller - Am. Chem. Soc. **125,** 9090 (2003)
[4]. J. Park, E. Lee, N. M. Hwang, M. Kang, S. Kim C., Y. Hwang, J.G. Park, H. Noh, J. Kim, J.H. Park, and **T. Hyeon** - Angew. Chem. Int. Edn., **44,** 2872 (2005)
[5]. T. Hyeon, S. S. Lee, J. Park, Y. Chung, and **H. B. Na** - J. Am.Chem. Soc. **123**, 12798, (2001)
[6]. S. Sun, and **C. B. Murray** - J. AppL Phys. **85**, 4325(1999)
[7]. N. Cordente, M. Respaud, F. Senocq, M. J. Casanove, C. Amiens, and **B. Chaudret -** Nano Lett. **1**, 565 (2001)
[8]. M. Aslam, R. Bhobe, N. Alem, S. Donthu, and **V. P. Dravid** - J. Appl. Phys., **98** 074311, (2005)
[9]. Y. Leng, Y. Zhang, T. Liu, M. Suzuki, and **X. Li** - Nanotech., 17, 1797-1800, (2006)
[10]. V. F. Puntes, K. M. Krishnan, and **A. P Alivisatos**.- Science **291**, 2115, (2001)
[11]. V. F Puntes., D. Zanchet, C. K. Erdonmez, and **A. P. Alivisatos** - J. Am. Chem. Soc., **124,** 12874, (2002)
[12]. N. Malikova, I. Pasioriza-Santos, M. Schierhom, N. A. Kotov, and **L. M. Liz-Maraan** - Langmuir, **18**, 3694, (2002)
[13]. R. Jin, Y. Cao, G. Mirkin, K. Kelly, G. Schatz, and **J. Zheng** - Science, **294**, 1901, (2001)
[14]. C. Salzemann, I. Lisiecki, J. Urban, and **M. P. Pileni -** Langmuir, **20**, 11772, (2004)
[15]. M. B. Sigman, A. Ghezelbash, T Hanrath., A. E. Saunders, F. Lee, and **B. A Korgel** - J. Am. Chem. Soc., **125**, 16050, (2003)
[16]. **S. Im, Y. Lee, B. Wiley**, and **Y.N. Xia -** Angew. Chem. Int. Edn.,**44**, 2154, (2005)
[17]. X. Xu and **G. Zangari -** J. Appl. Phys., **99**, 08M304, (2006).

MANUSCRISELE, CĂRŢILE ŞI REVISTELE PENTRU SCHIMB, PRECUM ŞI ORICE CORESPONDENŢE SE VOR TRIMITE PE ADRESA:

MANUSCRIPTS, REVIEWS AND BOOKS FOR EXCHANGE COOPERATION, AS WELL AS ANY CORRESPONDANCE WILL BE MAILED TO:

LES MANUSCRIPTS, LES REVUES ET LES LIVRES POUR L'ECHANGE, TOUT AUSSI QUE LA CORRESPONDANCE SERONT ENVOYES A L'ADRESSE:

MANUSCKRIPTEN, ZIETSCHRITFTEN UND BUCHER FUR AUSTAUCH SOWIE DIE KORRESPONDENZ SID AN FOLGENDE ANSCHRIFT ZU SEDEN:

After the latest evaluation of the journals achieved by National Center for the Science and Scientometry Politics (**CENAPOSS**), as recognition of its quality and impact at national level, the journal is included in B^+ category, 215 code (http://www.cncsis.ro/2006_evaluare_rev.php).

The journal is indexed in:
CSA: http://www.csa.com/ids70/serials_source_list.php?db=mechtrans-set-c
EBSCO: http://www.ebscohost.com/titleLists/a9h-journals.pdf
Copernicus: http://journals.indexcopernicus.com/karta.php

The papers published in this journal can be visualized on the "Dunarea de Jos" University of Galati site, the Faculty of Materials and Environmental Engineering, page: www.fimm.ugal.ro.

Publisher's Name and Address:
Contact person: Antoaneta CĂPRARU
Galati University Press - GUP
47 Domneasca St., 800008 - Galati, Romania
Phone:+40 336 130139, Fax: +40 236 461353
Email: gup@ugal.ro

Editor's Name and Address:
Prof. Dr. Eng. Marian BORDEI
Dunarea de Jos University of Galati, Faculty of Materials and Environmental Engineering
111 Domneasca St., 800201 - Galati, Romania
Phone: +40 336 130223, Phone/Fax: +40 236 460750
Email: mbordei@ugal.ro

AFFILIATED WITH:

- *ROMANIAN SOCIETY FOR METALLURGY*
- *ROMANIAN SOCIETY FOR CHEMISTRY*
- *ROMANIAN SOCIETY FOR BIOMATERIALS*
- *ROMANIAN TECHNICAL FOUNDRY SOCIETY*
- *THE MATERIALS INFORMATION SOCIETY (ASM INTERNATIONAL)*

Annual subscription (4 issues per year)

Edited under the care of
Faculty of
MATERIALS AND ENVIRONMENTAL ENGINEERING

Edited date: 30.06.2013
Issues number: 200
Printed by
Galati University Press
accredited CNCSIS
47, Domnească Street, 800036
Galati, Romania